

# **Modeling the Inelastic Behavior of High-Temperature Steels Exerted to Variable Loading Conditions**

DISSERTATION

zur Erlangung des akademischen Grades

Doktoringenieur  
(Dr.-Ing.)

von M.Sc. Katharina Knappe

geboren am 25.06.1995 in Brandenburg an der Havel

genehmigt durch die Fakultät für Maschinenbau  
der Otto-von-Guericke-Universität Magdeburg

Gutachter:

1. Prof. Dr.-Ing. habil. Dr. h.c. Holm Altenbach
2. Prof. Dr.-Ing. habil. Michael Johlitz

Promotionskolloquium am 22.10.2025

## Zusammenfassung

Martensitische Stähle werden häufig in Kraftwerkskomponenten eingesetzt, die bei hohen Temperaturen bis zu  $650^{\circ}\text{C}$  betrieben werden. Diese Komponenten erfahren nicht nur Kriechverformungen aufgrund mechanischer Lasten bei erhöhten Temperaturen, sondern sind auch zyklischen Belastungen ausgesetzt, die durch häufige Hoch- und Herunterfahrvorgänge entstehen. Dank ihrer robusten mechanischen und thermischen Eigenschaften sind wärmebehandelte martensitische Stähle in der Lage, solchen anspruchsvollen Betriebsbedingungen standzuhalten. Allerdings neigen diese Stähle unter Kriechbeanspruchung und zyklischen Lasten zur Entfestigung. In den letzten Jahren konzentrierte sich die Forschung auf die Modellierung des inelastischen Materialverhaltens dieser Stähle bei erhöhten Temperaturen. Für die Legierungen X20CrMoV12-1 und X12CrMoWVNbN10-1-1 wurde die Phasenmischungsregel verwendet, um die konstitutiven Gleichungen einschließlich einer Evolutionsgleichung für die inelastische Verformung, die Rückspannung und die Entfestigungsvariable abzuleiten. Die Materialmodelle wurden durch zahlreiche Experimente kalibriert, um das Materialverhalten realitätsnah abbilden zu können.

Konventionelle Implementierungen leiden jedoch unter hohen Rechenkosten, da für die Zyklus-für-Zyklus-Simulationen extrem kleine Zeitschritte erforderlich sind. Zur Lösung dieses Problems wird in der vorliegenden Arbeit ein Zwei-Zeitskalen-Ansatz vorgestellt, der die Rechenzeit um etwa 80% reduziert und gleichzeitig eine hohe Genauigkeit bewahrt, wie durch experimentelle Daten und Finite-Elemente-Simulationen validiert wurde. Hierfür werden eine schnelle oder Mikrozeitskala sowie eine langsame, sogenannte Makrozeitskala definiert, die eine Zerlegung und Entkopplung des Problems ermöglichen. Der Ansatz basiert auf der asymptotischen Reihenentwicklung der konstitutiven Gleichungen in Bezug auf einen Skalierungsparameter, der das Verhältnis der beiden Skalen darstellt. Die Implementierung des Ansatzes beruht auf der Periodizitätsbedingung des Lastprofils, die durch das Langzeitdehnverhalten und das thermomechanische Belastungskollektiv von Kraftwerkskomponenten erfüllt wird.

Im Rahmen dieser Arbeit dient das explizite ADAMS-BASHFORTH- sowie das explizite EULER-Verfahren zur Implementierung der grundlegenden Gleichungen in einem Python-Code, auf den dann der Zwei-Zeitskalen-Ansatz angewendet wird. Die Homogenisierung erfolgt nach der Trapezregel, um die Funktionen für ein definiertes Integral auswerten zu können. Die Ergebnisse des Multiskalierungsverfahrens werden mit Ergebnissen aus der Finite-Elemente-Software ABAQUS sowie mit experimentellen Daten verglichen und validiert. Zudem wird der Einfluss verschiedener Skalierungsparameter sowie Zeitschrittgrößen für die Makroskala untersucht.

Im letzten Teil wird die gleiche numerische Technik verwendet, um einen Materialparameter aus dem Langzeitverhalten zu berechnen. Hierfür wird die Evolutionsgleichung für das Entfestigungsverhalten angepasst, um die Simulationsergebnisse insbesondere im Bereich von  $N = 10^2 - 10^6$  Zyklen zu verbessern, da die Abnahme des Maximal- und Minimalwerts pro Zyklus im bestehenden Modell nicht ausreichend erfasst bzw. abgebildet wird. Die experimentellen Daten bezüglich einer großen Anzahl von Zyklen werden in den Python-Code eingefügt, um die Simulation mit einem unbekannten Exponenten durchzuführen, sodass dessen Wert bestimmt werden kann, um die Materialantwort realistischer vorherzusagen.

Die Arbeit stellt die validierte Anwendung eines Zwei-Zeitskalen-Ansatzes für hochtemperaturbeständige martensitische Stähle dar und hebt sich damit vor allem in Hinblick auf die Rechenzeiten von bisherigen Simulationsmethoden ab. In zukünftigen Anwendungen könnten diese Ergebnisse als Grundlage zur Abschätzung von zyklischen Ermüdungsschäden dienen und damit eine präzisere Vorhersage der Lebensdauer von Kraftwerkskomponenten ermöglichen.



## Abstract

Tempered martensitic steels are widely applied in power plant components operating at high temperatures, reaching up to 650°C. These components experience not only creep deformation due to mechanical loads at elevated temperatures but also endure cyclic loading as a result of highly frequent start-up and shut-down operations. Because of their robust mechanical and thermal properties, tempered martensitic steels are able to withstand such demanding service conditions. However, these steels are prone to softening under both constant creep and cyclic loads. During the past years, a main focus of this research field was to model the inelastic material behavior of these steels at elevated temperatures. For the alloys X20CrMoV12-1 and X12CrMoWVNbN10-1-1, the phase mixture rule was employed to derive the constitutive equations including an evolution equation for the inelastic strain, the backstress and the softening variable. The material models were calibrated through numerous experiments in order to be able to depict the material's response realistically.

However, conventional implementations suffer from high computational costs due to the extremely small time steps required for cycle-by-cycle simulations. To overcome this, the present work introduces a two-time-scale multiscaling approach, which reduces computation time by approximately 80% while preserving accuracy, as validated against experimental data and finite element simulations. Therefore, a fast or micro time scale as well as a slow, so-called macro time scale are defined allowing for a decomposition and decoupling of the problem. The approach is based on the asymptotic series expansion of the constitutive equations with respect to a scaling parameter representing the ratio of the two scales. The implementation of the approach requires the periodicity of the loading condition which is met by the low cycle and real-life thermo-mechanical fatigue profiles power plant components are subjected to.

Within this work, the explicit ADAMS-BASHFORTH as well as the EULER FORWARD method serves for the implementation of the governing equations in a python code where the two-time-scale approach is then applied. The time averaging is done by the trapezoidal rule in order to be able to evaluate the functions for a defined finite integral. The results of the multiscaling procedure are compared to and validated with results from the finite element software ABAQUS together with experimental data. Furthermore, the influence of different scaling parameters as well as time step sizes for the macro scale are examined.

In the final part, the same numerical technique is applied to calculate a material parameter from the long time response. Therefore, the evolution equation for the softening behavior is adapted in order to improve the simulation results especially in the range of  $N = 10^2 - 10^6$  cycles since the decrease of the maximum and minimum values is not well captured by the existing model. The experimental data with respect to a large number of cycles is fitted and inserted into the python code. The simulation is carried out with one unknown exponent so that the optimal value can be found to predict the material's response more realistically.

This work represents a validated implementation of a two-time-scale multiscaling strategy for high-temperature martensitic steels, setting it apart from conventional simulation approaches especially with respect to the calculation times. In future applications, these results could serve as a foundation for estimating cyclic fatigue damage, enabling accurate predictions of the operational lifetime of power plant components.

# Contents

<b>Figures</b>	<b>vi</b>
<b>Tables</b>	<b>ix</b>
<b>Nomenclature</b>	<b>x</b>
<b>1 Introduction</b>	<b>1</b>
1.1 High-Temperature Materials . . . . .	2
1.1.1 Mechanical Behavior . . . . .	4
1.1.2 Modeling Approaches . . . . .	6
1.1.3 Simulation Approaches . . . . .	8
1.2 Outline . . . . .	11
<b>2 Theoretical Background</b>	<b>12</b>
2.1 Cyclic Material Behavior . . . . .	12
2.2 Continuum Mechanics . . . . .	15
2.3 Constitutive Equations of the Phase Mixture Model . . . . .	19
2.3.1 Elasticity . . . . .	20
2.3.2 Inelasticity . . . . .	22
2.3.3 Initial Boundary Value Problem . . . . .	25
2.4 Methods of Time Integration . . . . .	25
2.4.1 Explicit Time Integration Methods . . . . .	27
2.4.2 Implicit Time Integration Methods . . . . .	28
2.5 Two-Time-Scale Approach . . . . .	30
<b>3 Numerical Implementation for X20CrMoV12-1</b>	<b>35</b>
3.1 Cycle-by-cycle Simulations . . . . .	35
3.1.1 Constitutive Equations . . . . .	35
3.1.2 Implementation . . . . .	40
3.1.3 Validation . . . . .	42
3.2 Application of the Two-Time-Scale Approach . . . . .	48
3.2.1 Constitutive Equations . . . . .	49
3.2.2 Implementation . . . . .	53
3.2.3 Validation . . . . .	56
3.3 Simulation of a Large Number of Cycles . . . . .	64
<b>4 Application to X12CrMoWVNbN10-1-1</b>	<b>67</b>
4.1 Cycle-by-cycle Simulations . . . . .	67
4.1.1 Constitutive Equations . . . . .	67
4.1.2 Implementation . . . . .	70

## Contents

4.1.3	Validation . . . . .	71
4.2	Application of the Two-Time-Scale Approach . . . . .	75
4.2.1	Macrochronological Problem . . . . .	76
4.2.2	Microchronological Problem . . . . .	76
4.3	Validation . . . . .	77
<b>5</b>	<b>Formulation and Identification of a New Softening Model</b>	<b>84</b>
5.1	Adaption of the Material Model . . . . .	84
5.2	Calculation of Adapted Softening Evolution . . . . .	86
5.3	Validation of the New Parameter . . . . .	91
<b>6</b>	<b>Summary and Outlook</b>	<b>93</b>
6.1	Conclusions . . . . .	94
6.2	Further Research . . . . .	95
	<b>Bibliography</b>	<b>97</b>

# Figures

1.1	Heavy duty gas turbine SGT6-9000HL [144] . . . . .	2
1.2	Real-life cyclic loading condition of power plant components due to start-ups and shut-downs according to [87, 113] . . . . .	4
1.3	Iron-carbon phase diagram [103] (top) and schematic sketches of a body-centered cubic (a) and body-centered tetragonal (b) unit cell after [41] . . . . .	5
1.4	Overview of multi-scale computational strategies in time . . . . .	9
1.5	Principle of the LATIN algorithm after [92] . . . . .	9
1.6	Schematic description of the cycle jump method after [70, 101] . . . . .	10
2.1	Evolution of the yield surface under isotropic expansion (a) and under kinematic translation (b) . . . . .	13
2.2	Qualitative evolution of the stress amplitude with respect to the number of LCF cycles, after [121] . . . . .	13
2.3	Strain-controlled loading path . . . . .	14
2.4	Change of line segment $d\mathbf{a}$ in the reference configuration at time $t_0$ (red arrow) in comparison to $d\mathbf{x}$ in the actual configuration (blue arrow) after deformation $\mathbf{u}$ . . . . .	16
2.5	Schematic diagram for an explicit time integration procedure . . . . .	27
2.6	Comparison between the general program flowcharts of explicit and implicit time integration methods . . . . .	29
2.7	Basic principle of the two-time-scale approach by dividing the physical time $t$ shown in (a) into the two time scales: the macro scale $t_M$ illustrated in part (b) and the micro time $\tau$ depicted in (c) after [69] . . . . .	30
2.8	Schematic decomposition of the physical time $t$ after [69] . . . . .	31
2.9	Sketch of an approximation to the arbitrary function $f(x)$ in the interval from $a$ to $b$ depicted in blue using the trapezoidal rule with five segments after [33] . . . . .	34
3.1	Rheological model of the iso-strain concept after [48] . . . . .	37
3.2	Results of the HT tensile tests with a the constant strain rates $\dot{\epsilon}_{22} = 1.0 \cdot 10^{-4} \text{ s}^{-1}$ and $\dot{\epsilon}_{22} = 5.0 \cdot 10^{-5} \text{ s}^{-1}$ at different temperatures . . . . .	43
3.3	FEM model of the pipe including the loading direction as well as the point to extract the results from (left) and a schematic representation of the elements used (right) . . . . .	44
3.4	Simulation results of three cycles of the LCF test at elevated temperature and the comparison of them to the ABAQUS result . . . . .	45
3.5	Simulation of the uniaxial low cycle fatigue test with respect to the different temperature levels compared to the corresponding ABAQUS simulation (dashed line) . . . . .	45
3.6	Convergence of the explicit time integration; logarithmic error vs. time step size . . . . .	46
3.7	TMF test loading: strain and temperature profile after [87] . . . . .	46

3.8	Comparison of the resulting material response between ABAQUS and Python simulations . . . . .	47
3.9	Service-type loading profile of a power plant component, including cold, warm as well as hot starts [87] . . . . .	47
3.10	Results of the TMF profile: the stress (a) and the internal variables namely the inelastic strain $\varepsilon_{22}^{\text{in}}$ (b), the backstress $\beta_{22}$ (c) and the softening variable $\Gamma$ (d) . .	48
3.11	Scheme of the steps taken to solve the multiscale problem with respect to the fast and slow time scales $\tau$ and $t_M$ after [85] . . . . .	55
3.12	Program flowchart for the implementation of the two-time-scale approach for solving the constitutive equations for high temperature steel . . . . .	57
3.13	Comparison of the experimental input and the fitted sine function . . . . .	58
3.14	Comparison of the elastic cycle-by-cycle simulation with the elastic temporal multiscale algorithm for $N = 100$ cycles . . . . .	59
3.15	Comparison of the fully resolved internal variables and the averaged value of the elastic solution: for the inelastic strain $\varepsilon^{\text{in}}$ (a), the backstress $\beta$ (b) and the softening variable $\Gamma$ (c) . . . . .	60
3.16	Comparison of the cycle-by-cycle simulation with the temporal multiscale algorithm for $N = 100$ cycles . . . . .	61
3.17	Relative error of the maximum stress values for $N = 100$ cycles . . . . .	61
3.18	Comparison of the fully resolved internal variables and the averaged value: for the inelastic strain $\varepsilon^{\text{in}}$ (a), the backstress $\beta$ (b) and the softening variable $\Gamma$ (c) .	62
3.19	Result of the maximum stress calculated by the multiscale algorithm depending on the macro time step $\Delta t_M$ . . . . .	63
3.20	Comparison of the averaged internal variables for different $\Delta t_M$ : the inelastic strain $\varepsilon^{\text{in}}$ (a), the backstress $\beta$ (b) and the softening variable $\Gamma$ (c) . . . . .	63
3.21	Comparison of the stress as well as the averaged internal variables for $10^3$ cycles: the maximum stress per cycle (a), the inelastic strain $\varepsilon_{22}^{\text{in}}$ (b), the backstress $\beta_{22}$ (c) and the softening variable $\Gamma$ (d) . . . . .	65
4.1	Simulation results of three cycles in the LCF test: in comparison with the ABAQUS result (a) and to the experimental results (b) . . . . .	71
4.2	Comparison of the simulation results regarding one LCF cycle with a constant strain rate of $\dot{\varepsilon} = 0.06 \frac{\%}{\text{min}}$ . . . . .	72
4.3	Simulation of several cycles in the LCF test: in comparison with the SIEMENS NX result (a) and with the experimental data (b) . . . . .	72
4.4	Simulated service-type loading profile of a power plant component, including cold, warm as well as hot starts [87] . . . . .	73
4.5	TMF test: comparison between the stress response and the FEM solution (a) and the resulting material response from experimental data (b) . . . . .	74
4.6	Results of the TMF profile: the stress (a) and the internal variables namely the inelastic strain $\varepsilon_{22}^{\text{c}}$ (b), the backstress $\beta_{22}$ (c) and the softening variable $\Gamma$ (d) . .	74
4.7	Fitting result of the experimental strain input . . . . .	77
4.8	Comparison of the cycle-by-cycle simulation with the two-time-scale approach for $N = 100$ cycles of the LCF profile with a constant strain rate of $\dot{\varepsilon} = 0.06 \frac{\%}{\text{min}}$ .	78
4.9	Comparison of the internal variables with respect to the multiscale solution: for the inelastic strain $\varepsilon^{\text{c}}$ (a), the backstress $\beta$ (b) and the softening variable $\Gamma$ (c) .	79
4.10	Hysteresis loop of the first cycle compared to the SIEMENS NX Solution (a) and the with respect to the 100 <sup>th</sup> cycle compared to the multiscale solution (b) . . .	79

4.11	Maximum normalized stress with respect to the different macro time steps referred to in Table 4.3 (top) and the error development (bottom) . . . . .	81
4.12	Comparison of normalized maximum stress values $\sigma_a/ \sigma_{a,\min} $ per cycle $N$ for the cycle-by-cycle simulation (reference), the multiscale solution ( $\Delta t_M = 10P$ ), and experimental measurements (the stress values are normalized using the absolute minimum of the reference simulation) . . . . .	82
5.1	Qualitative sketch to show the dependency of the cyclic strain (a) and plastic strain amplitudes (b) on time . . . . .	85
5.2	Fitting result of the experimental strain input . . . . .	87
5.3	Comparison of the experimental data, the two-time-scale approach and the fully resolved simulation for $N = 800$ cycles of the LCF profile with the exponent $m = 2.0$ . . . . .	89
5.4	Comparison of the internal variables between the cycle-by-cycle integration and the multiscale solution for $m = 2.0$ for the inelastic strain $\varepsilon_{22}^c$ (a), the backstress $\beta_{22}$ (b) and the softening variable $\Gamma$ (c) . . . . .	90
5.5	Comparison of the experimental data, the two-time-scale approach including the new cyclic softening evolution and the applying the previous definition . . . . .	91
5.6	Comparison of the cyclic softening evolution with the previous definition with respect to a large number of cycles . . . . .	92

# Tables

1.1	Chemical composition of the alloys . . . . .	3
3.1	Parameter values for the X20CrMoV12-1 material model [48] . . . . .	39
3.2	Coefficients and root mean square error to the function described in Eq. (3.91) .	56
3.3	Comparison of the simulation times for the phase-mixture-model of the alloy X20CrMoV12-1 between the cycle-by-cycle and two-time-scale simulation . .	60
3.4	Influence of the size of the scaling factor $\mu$ on the simulation time as well as the accuracy of results using the cycle-by-cycle simulation as reference to calculate the relative error at the 100 <sup>th</sup> cycle . . . . .	64
3.5	Comparison of the simulation times for the phase-mixture-model of the alloy X20CrMoV12-1 between the cycle-by-cycle and two-time-scale simulation . .	65
4.1	Coefficients and root mean square error of the function Eq. (4.40) . . . . .	77
4.2	Comparison of the simulation times for the cycle-by-cycle simulation and two-time-scale solution for X12CrMoWVNbN10-1-1 . . . . .	80
4.3	Comparison of different simulation parameters for $N = 100$ cycles with respect to the reduction in computational time . . . . .	81
5.1	Coefficients and root mean square error of the power law function fitting the experimental values . . . . .	87
5.2	Error calculation with respect to the cycle number for the different simulations varying the exponent $m$ in the softening evolution compared to the experimental data . . . . .	89

# Nomenclature

## Tensor Notation Conventions

- $a, A$  : Scalars, tensor of zeroth rank
- $\mathbf{a}$  : Vector, tensor of first rank
- $\mathbf{A}$  : Dyad, tensor of second rank
- $\mathcal{A}$  : Tetrad, tensor of fourth rank

## Products in Direct Tensor Notation (Orthonormal Bases)

Scalar product of two vectors  $\mathbf{a} = a_i \mathbf{e}_i$  and  $\mathbf{b} = b_j \mathbf{e}_j$ :

$$\mathbf{a} \cdot \mathbf{b} = a_i b_i$$

Vector product of vectors  $\mathbf{a} = a_i \mathbf{e}_i$  and  $\mathbf{b} = b_j \mathbf{e}_j$  including the LEVI-CIVITA symbol for three dimensions  $\epsilon_{ijk}$ :

$$\mathbf{a} \times \mathbf{b} = a_i b_j \epsilon_{ijk} \mathbf{e}_k$$

Dyadic product of two vectors  $\mathbf{a} = a_i \mathbf{e}_i$  and  $\mathbf{b} = b_j \mathbf{e}_j$ :

$$\mathbf{a} \otimes \mathbf{b} = a_i b_j \mathbf{e}_i \otimes \mathbf{e}_j$$

Dyadic product of second-rank tensors  $\mathbf{A} = A_{ij} \mathbf{e}_i \otimes \mathbf{e}_j$  and  $\mathbf{B} = B_{kl} \mathbf{e}_k \otimes \mathbf{e}_l$ :

$$\mathbf{A} \otimes \mathbf{B} = A_{ij} B_{kl} \mathbf{e}_i \otimes \mathbf{e}_j \otimes \mathbf{e}_k \otimes \mathbf{e}_l$$

Double scalar product of second-rank tensors  $\mathbf{A} = A_{ij} \mathbf{e}_i \otimes \mathbf{e}_j$  and  $\mathbf{B} = B_{kl} \mathbf{e}_k \otimes \mathbf{e}_l$ :

$$\mathbf{A} : \mathbf{B} = A_{ij} B_{ji}$$

Scalar products between the tensor of second rank  $\mathbf{A} = A_{ij} \mathbf{e}_i \otimes \mathbf{e}_j$  and the vector  $\mathbf{a} = a_i \mathbf{e}_i$ :

$$\mathbf{a} \cdot \mathbf{A} = A_{ij} a_j \mathbf{e}_i,$$

$$\mathbf{A} \cdot \mathbf{a} = A_{ij} a_i \mathbf{e}_j$$

Double scalar products between a second-rank tensor  $\mathbf{A} = A_{ij} \mathbf{e}_i \otimes \mathbf{e}_j$  and a fourth-rank tensor  $\mathcal{C} = C_{abcd} \mathbf{e}_a \otimes \mathbf{e}_b \otimes \mathbf{e}_c \otimes \mathbf{e}_d$ :

$$\mathcal{C} : \mathbf{A} = C_{abcd} A_{dc} \mathbf{e}_a \otimes \mathbf{e}_b,$$

$$\mathbf{A} : \mathcal{C} = A_{ba} C_{abcd} \mathbf{e}_c \otimes \mathbf{e}_d$$



- Names are written in small capitals, e.g., EULER.
- The EINSTEIN summation is applied, latin indices take the values 1, 2, and 3 (unless mentioned otherwise).

## Latin Symbols

$A$	area	$g$	objective function
$a$	lower limit of interval	$G_1$	material parameter
$\mathbf{a}$	position vector	$G_2$	material parameter
$a_\beta$	material parameter	$h$	coefficient of time integration method
$a_\Gamma$	material parameter	$H$	hardening variable
$a_\sigma$	material parameter	$\mathbf{I}$	unit tensor of second rank
$A_E$	material parameter	$J$	tensor invariant
$A_h$	material parameter	$K$	bulk modulus
$A_S$	material parameter	$\mathbf{k}$	vector of body forces
$A_\nu$	material parameter	$L_e$	mechanical power
$b$	upper limit of interval	$\mathbf{l}$	vector of angular momentum
$b_\beta$	material parameter	$m$	mass
$b_\Gamma$	material parameter	$\mathcal{M}$	time averaging operator
$b_\sigma$	material parameter	$m_\sigma$	material parameter
$B_E$	material parameter	$n$	exponent in power law
$B_\nu$	material parameter	$N$	number of cycles
$C$	material parameter	$\mathbf{n}$	normal vector
$\mathbf{C}$	right CAUCHY-GREEN strain tensor	$O$	LANDAU notation
$\mathcal{C}$	elastic stiffness tensor	$p$	pressure
$c_\Gamma$	material parameter	$\mathbf{p}$	vector of linear momentum
$c_\sigma$	material parameter	$P$	period
$C_1$	material parameter	$\mathbf{P}$	PIOLA-KIRCHHOFF stress tensor
$C_2$	material parameter	$Q$	activation energy
$C_3$	material parameter	$Q_e$	rate of change non-mechanical energy
$C_\Gamma$	material parameter	$q$	scalar internal variable
$d$	diameter	$\mathbf{Q}$	tensorial internal variable
$D$	material parameter	$\mathbf{r}$	position vector
$D_E$	material parameter	$R$	universal gas constant
$D_\nu$	material parameter	$s$	number of stages of time integration method
$\mathbf{e}$	unit basis vector	$S$	entropy
$E$	YOUNG's modulus	$\mathbf{S}$	second PIOLA-KIRCHHOFF stress tensor
$E_e$	total energy of the system	$S_1$	linear subspace
$\mathbf{E}^G$	GREEN strain tensor	$S_{nl}$	non-linear subspace
$E_1$	material parameter	$s_n$	element solution
$E_2$	material parameter	$t$	time
$E_3$	material parameter	$\mathcal{T}$	time scale
$f$	frequency	$t_{\mathrm{macro}}$	macro (slow) time
$\mathbf{f}$	vector of forces	$\mathbf{t}$	stress vector
$\mathbf{F}$	deformation gradient	$\mathbf{t}_{PK}$	PIOLA-KIRCHHOFF stress vector
$f_T$	temperature response function	$\mathbf{t}_{PKII}$	second PIOLA-KIRCHHOFF stress vector
$f_\sigma$	stress response function	$T$	temperature
$G$	shear modulus	$T_h$	homologous temperature

## Nomenclature

$T_L$	liquidus temperature	$x$	coordinate
$\mathbf{u}$	displacement vector	$\mathbf{x}$	vector of unknown variables
$V$	volume	$y$	function in differential equation
$\mathbf{v}$	velocity vector	$\mathbf{Y}$	tensorial variables in differential equation

## Greek Symbols

$\beta$	component of the backstress	$\tilde{\sigma}$	effective stress
$\boldsymbol{\beta}$	backstress tensor	$\boldsymbol{\sigma}$	CAUCHY stress tensor
$\gamma$	isotropic hardening variable	$\tilde{\boldsymbol{\sigma}}$	effective stress tensor
$\Gamma$	softening variable	$\sigma_{\text{mean}}$	mean stress
$\varepsilon$	engineering strain	$\tau$	micro (fast) time scale
$\boldsymbol{\varepsilon}$	engineering strain tensor	$\varphi$	phase angle
$\varepsilon_V$	volumetric strain	$\Phi$	flow of balance quantity
$\eta$	volume fraction	$\Psi$	potential
$\mu$	scaling parameter	$\Psi$	balance quantity
$\nu$	POISSON's ratio	$\Xi$	growth of the balance quantity
$\rho$	mass density	$\omega$	angular frequency
$\sigma$	component of the stress tensor		

## Mathematical Operators

$d\Box$	infinitesimal value	$\partial\Box$	partial derivative
$\det \Box$	determinant	$\nabla\Box$	nabla operator
$\exp \Box$	exponential function	$\langle \Box \rangle$	time averaged value
$\lim \Box$	limit	$\Box \cdot \Box$	scalar product
$\ln \Box$	natural logarithm	$\Box : \Box$	double scalar product
$\sinh \Box$	hyperbolic sine function	$\Box \times \Box$	vector product
$\text{tr} \Box$	trace	$\dot{\Box}$	1 <sup>st</sup> derivative w.r.t. time
$\Delta\Box$	incremental value	$\ddot{\Box}$	2 <sup>nd</sup> derivative w.r.t. time

## Super- and subscripts

$\Box^c$	creep	$\Box_h$	hard phase
$\Box^{el}$	elastic	$\Box_M$	w.r.t the macro time
$\Box^{in}$	inelastic	$\Box_m$	w.r.t the micro time
$\Box^{pl}$	plastic	$\Box_{\text{max}}$	maximum
$\Box^T$	transposed value	$\Box_{\text{min}}$	minimum
$\Box^{-1}$	inverse value	$\Box_n$	w.r.t. the $n$ -th time step
$\Box^{(\cdot)}$	order of asymptotic series expansion	$\Box_p$	index for phase: $p \in \{s, h\}$
$\tilde{\Box}$	active part	$\Box_s$	soft phase
$\bar{\Box}$	averaged value	$\Box_{vM}$	VON MISES variable
$\Box'$	deviator	$\Box_*$	saturation value
$\Box_{\text{end}}$	w.r.t. the last time step	$\Box_0$	reference configuration

## **Abbreviations**

FEM	finite element method	LCF	low cycle fatigue
FFT	fast FOURIER transformation	ODE	ordinary differential equation
HT	high temperature	PDE	partial differential equation
IBVP	initial boundary value problem	RMSE	root mean square error
IC	initial condition	TMF	thermo-mechanical fatigue
LATIN	large time increments	UMAT	user defined material

# 1 Introduction

The world's rapid ecologic and economic growth nowadays is also associated with an increasing demand in energy, especially power and heat [25]. In 1973, a total energy supply of 254 EJ was documented which grew to be more than twice as much, 606 EJ, 46 years later in 2019 [76]. The statistic considers conventional sources, such as coal, oil, natural gas and nuclear power but also renewable sources like wind, solar or biofuels. The major part of  $\approx 80\%$  of the global energy supply in the past as well as today is granted by traditional methods [76] showing that fossil fuels will remain indispensable parts of the world's energy supply for decades to come. This results in the central task of researchers to enhance the responsiveness and flexibility of the energy supply by securing and expanding technological options [23]. Furthermore, the International Energy Agency published an outlook for the year 2040 which estimates the use of the three main suppliers to be rather persistent. Of the total supply of 715 EJ approximately 73% are contributed by them, where the natural gas is expected to experience the largest increase from 23% to 25%. From an environmental point of view, this tendency may also be considered positive, since natural gas power plants emit remarkably less green house gases compared to a world average coal-fired power plant [25]. Therefore, modern gas turbine power plants generate a significant amount of electricity. Their history dates back over a century, when in 1872, STOLZE patented first developments of a turbine powered by gas [96]. They were mainly limited by the possible turbine-inlet temperature so that ever since then, the concept evolved due to ongoing research which focusses on enhancing efficiency, reducing emissions, and increasing the flexibility of gas turbines [109]. During World War II, the technology primarily contributed to aviation applications, where gas-turbine jet engines manufactured in Britain, Germany and the United States served in combat aircraft [96]. At the same time, gas turbines started being adapted for power generation. In 1940, the world's first successful gas turbine power plant, the Neuchâtel Power Station, began operating in Switzerland. It produced 4 MW of power by a process known as simple cycle, meaning that hot gas is passed through a single turbine at high pressure [109]. However, it soon became clear that this performance needed improvement. First, larger plants followed, then in 1961, a new concept was introduced: the combined-cycle power plant. They utilize both gas turbines and steam turbines to generate electricity, allowing for higher overall efficiency of 50 – 60% producing more than 1500 MW [109].

This configuration remains the leading technology today for several reasons, e.g. outstanding flexibility and maintainability, low investment costs and high electrical efficiency [51]. The ongoing reform of energy sources states the increasing use of renewable resources which suffer from one major complication: they are depending on ambient conditions, like seasons or geographics resulting in intermittent and unpredictable output which then leads to a gap between energy supply and demand. Gas turbine power plants are considered to be well suited to fill this void, mainly because of their superior operational flexibility which refers to the capability of producing when required with decent reaction times [51]. Once invented, they were supposed to be running for long time spans under stationary conditions, thus having a constant, high loading regime. This new, efficient mode implies more start-ups and shut-downs of the system as well

as enormous load changes subjecting the components not only to high temperature conditions but also cyclic loads in the form of periodic stress and strain states [55, 51]. The combination of both, mechanical and thermal demands greatly influences the component's life and may lead to premature failure. To prevent unforeseen events and investment costs, an understanding of the material's behavior and response through a reliable simulation is mandatory.

## 1.1 High-Temperature Materials

The request for environmentally friendly and resource-saving processes, as well as the need to increase the efficiency in power plants result in higher operating temperatures. Consequently, these conditions lead to extreme demands on the materials used. In order to evaluate if an application involves high temperature (HT) conditions, the homologous temperature  $T_h$  can be used which describes the relation between the absolute temperature  $T$  and the liquidus temperature of the material  $T_L$  [60, 111]. Materials operating within the temperature range of  $0.3 < T/T_L < 0.7$  are called high-temperature materials [111]. Currently, the operating temperature of a power plant is estimated to be around 873 K [43, 49]. Under this premise, the targeted and continuous development of steam turbine components, shown in Fig. 1.1, and their materials is of crucial importance, as any increase in steam parameters progressively affects the overall thermal efficiency of the system.

Tempered martensitic steels are well suited for those applications. They contain a chromium content of 9 – 12%, often turbines, expander blades, or tubes are made of them [48, 51, 116]. Here, a chromium content of 9% is considered as the lower limit for sufficient carbide formation and a chromium content of 12% represents the upper boundary where a complete austenitization and subsequent martensitic transformation is still possible [50]. Typical materials of this class are applied in tubes and temperature vessels [128], namely the alloys X12CrMoWVNbN10-1-1 and X20CrMoV12-1, steel numbers 1.4903 and 1.4922 according to [45]. Their chemical composition is summarized in Table 1.1.

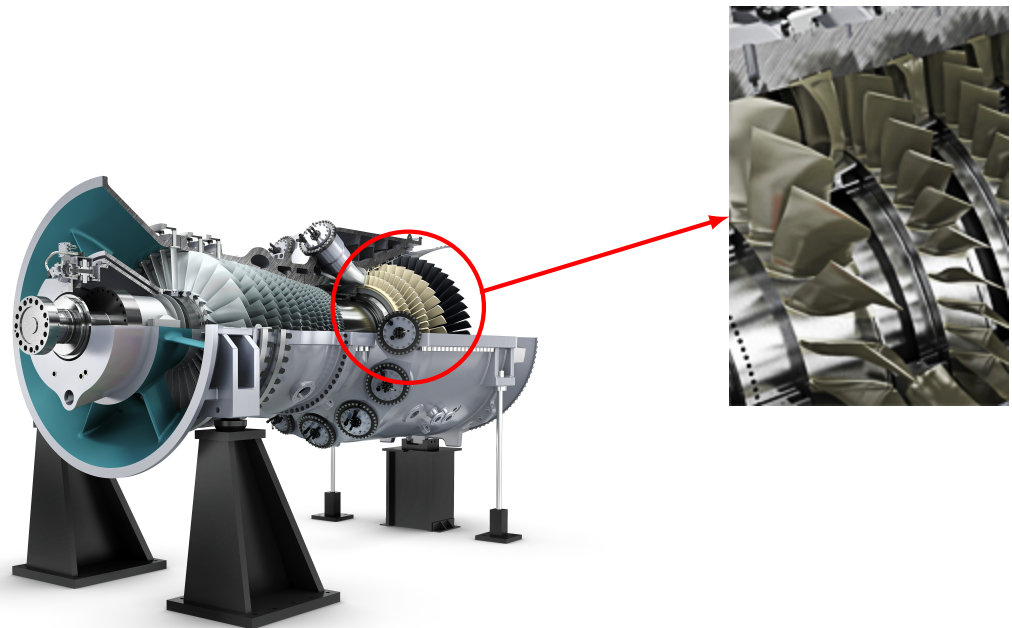


Figure 1.1: Heavy duty gas turbine SGT6-9000HL [144]

Table 1.1: Chemical composition of the alloys

Element	X12CrMoWVNbN10-1-1 [154]	X20CrMoV12-1 [156]
Carbon (C)	0.12%	0.17 – 0.23%
Chromium (Cr)	10.0%	10.00 – 12.50%
Molybdenum (Mo)	1.0%	0.80 – 1.20%
Vanadium (V)	0.2%	0.25 – 0.35%
Manganese (Mn)	–	$\leq 1.00\%$
Niobium (Ni)	0.8%	0.30 – 0.80%

For X20CrMoV12-1, the liquidus temperature was calculated in [48] based on an average composition of 0.20% Carbon (C), 11.25% Chromium (Cr), 1.00% Molybdenum (Mo), 0.30% Vanadium (V), 0.50% Manganese (Mn) and 0.50% Niobium (Ni) to be  $T_L \approx 1764$  K [48]. Therefore, the relative temperature yields  $T_h \approx 0.49$  proving that power plant components are subjected to high temperature creep according to [60] where the homologous temperature is also described as a measure to classify creep loads. The creep process itself is characterized as a relatively slow time-dependent irreversible deformation due to changes in the microstructure occurring over a long period of time [5]. These microstructural evolutions typically include grain boundary sliding, dislocation movement, and phase transformations, which progressively degrade the mechanical performance of the material.

In addition, the frequent start-ups and shut-downs result in cyclic loads due to the temperature changes, which are crucial for the material and the component's lifespan. Furthermore, there are mechanical loads like the steam pressure of  $p = 20 - 30$  MPa [48] and centrifugal forces to withstand due to the rotational frequency which is normally  $f = 50 - 60$  Hz [144]. These loads act simultaneously, creating a complex stress state within critical components like rotors, turbine blades, and thick-walled pressure vessels.

In conclusion, this represents a comprehensive problem due to the combined and interacting effects of complex thermal and mechanical loadings, as depicted in Fig. 1.2. A reliable lifetime prediction requires suitable material laws which describe the stress-strain-time behavior with sufficient accuracy and which can be applied to multiaxial loading cases, as commonly encountered in practice. Only through such detailed and physically grounded modeling approaches can the structural integrity and safe operation of high-temperature components be ensured over extended service periods.

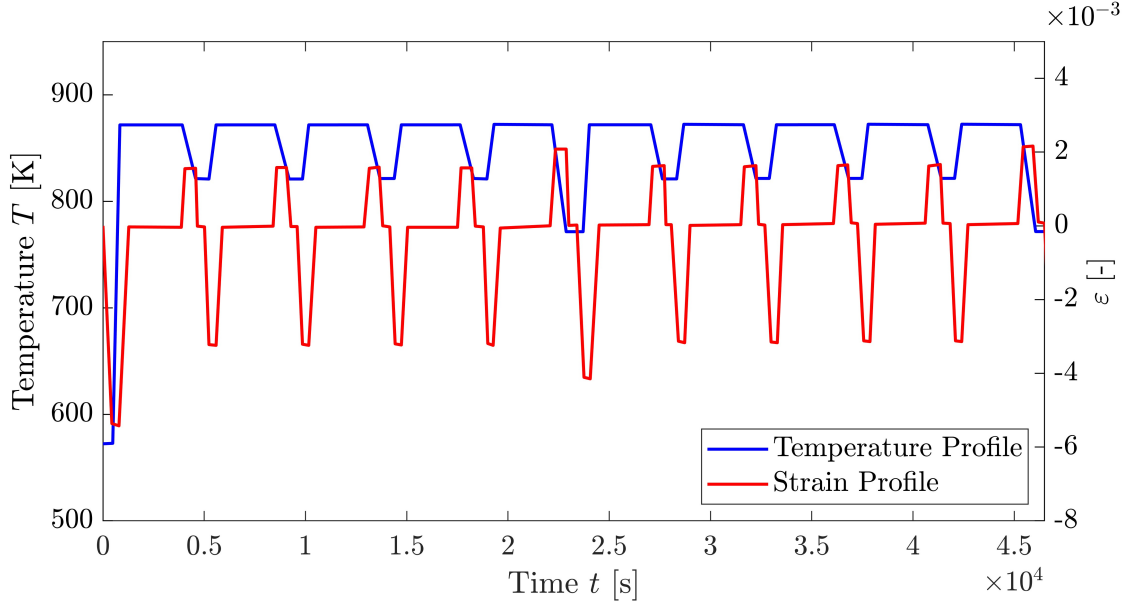


Figure 1.2: Real-life cyclic loading condition of power plant components due to start-ups and shut-downs according to [87, 113]

### 1.1.1 Mechanical Behavior

The goal of this thesis is to depict the response of high temperature steels to variable loading conditions. The macro-mechanical behavior of such tempered martensitic steels is greatly influenced by the microstructure which itself is depending on the chemical composition and the heat treatment conducted to improve the mechanical properties. The microstructural analysis can then be done by light optical microscopy, allowing the lattice structure made of individual grains and their boundaries to be seen [3]. The grain boundaries are considered to be two-dimensional lattice defects in the form of an interface between two grains of the same phase but different orientation. The change in orientation between two bordering grains is measured as angle, differentiating between low- and high-angle grain boundaries [40, 131]. Low-angle grain boundaries can also be found within a single grain, dividing it into subgrains and therefore forming a subgrain structure [3, 48]. They are also described as one-dimensional lattice defects, called dislocations.

Usually, these materials are heat-treated to improve their performance. The process consists of the austenitization, the forming of martensite and annealing [48, 63]. At room temperature, the body-centered cubic ferrite is the primary stable phase, the austenitization then happens when the steel is heated up to 1343 K. The dissolving of carbon and special carbide formers also takes place for sufficient holding times of 30 – 60 minutes [63]. Afterwards, the material is cooled down, during which martensite with a body-centered tetragonal crystal structure is formed. A schematic sketch of those unit cells can be found in Fig. 1.3. Typically, during the last step, the annealing, steels with high chromium content are heated up to 1033 K depending on the size of the component [63, 149]. The heat treatment of those materials aims at forming a complete martensite microstructure which is characterized by its high hardness and strength.

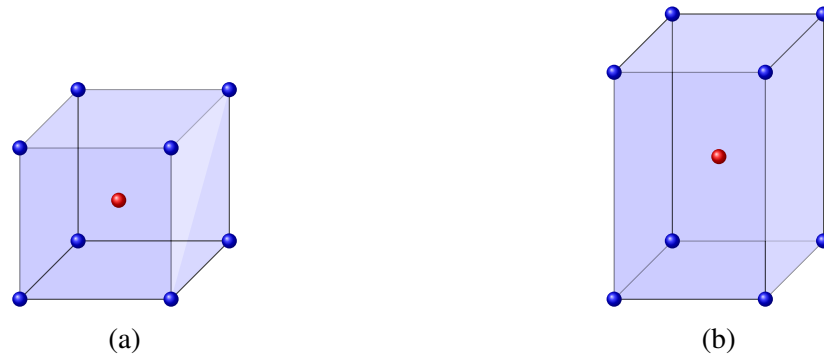
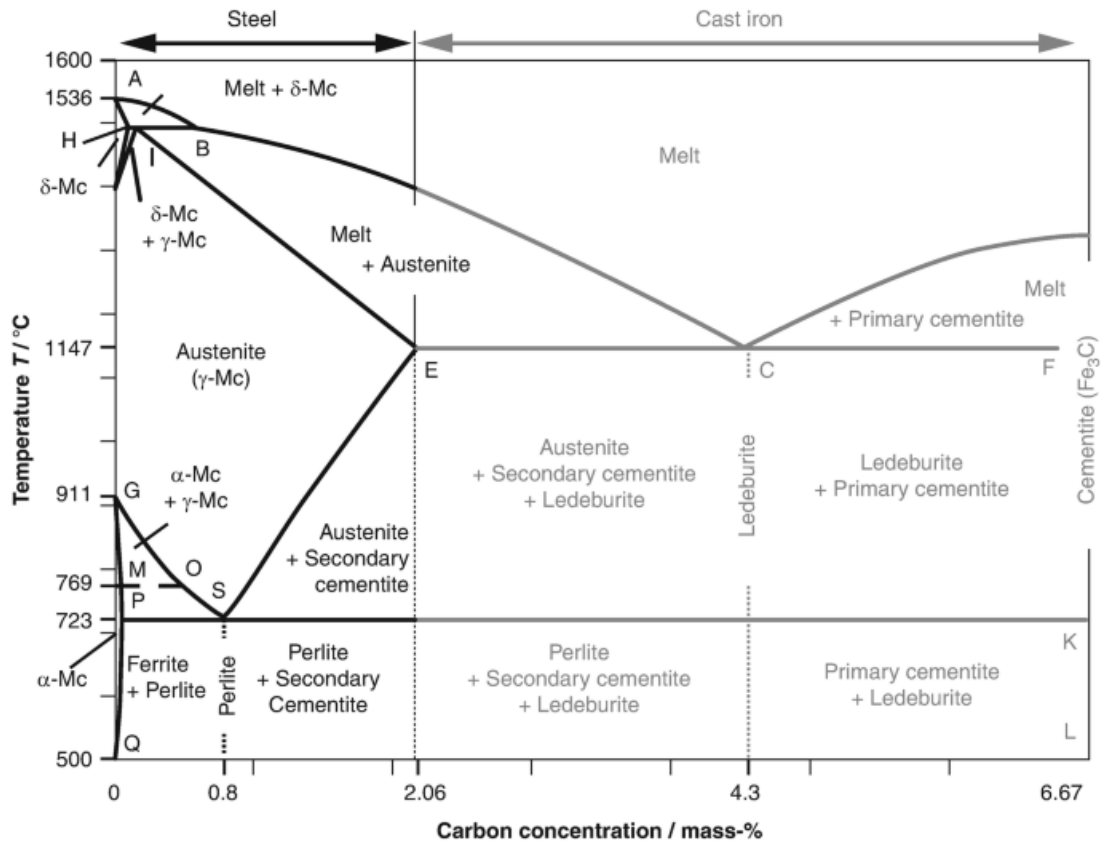


Figure 1.3: Iron-carbon phase diagram [103] (top) and schematic sketches of a body-centered cubic (a) and body-centered tetragonal (b) unit cell after [41]

When dealing with variable loading conditions at elevated temperatures, the choice of material is strongly depending on mechanical and thermal properties. High chromium martensitic steels such as X12CrMoWVNbN10-1-1 and X20CrMoV12-1 are known to have a high tensile strength, a low coefficient of thermal expansion and an increased thermal conductivity as well as a good corrosion resistance and creep strength [48, 63, 87]. On the other hand, this class of materials undergoes softening, the increasing strain rate with increasing time and deformation, especially under creep and fatigue loads [54, 149]. Generally, they exhibit only primary and tertiary creep stages. In the beginning, the strain rate decreases due to hardening effects until a minimum value. After that, the strain rate increases which can be traced back to softening processes [113]. The creep rate depends essentially on the generation, movement, hindered motion, and annihilation of dislocations. The dislocation structure results from a continuous process of formation and annihilation. Plastic deformation initially leads to a higher dislocation density



and associated strengthening. With increasing plastic deformation, an equilibrium is then established between the newly generated dislocations and those mutually annihilating, limiting the strengthening effect [77, 104]. At high stresses, the deformation process is mainly based on dislocation glide, which typically leads to transgranular fracture after significant plastic deformation. At higher temperatures, lower stresses also result in plastic deformation through dislocation creep. This involves diffusion processes and the climbing of stair-rod dislocations for plastic deformation [77, 104]. At high temperatures, the dislocation density can decrease due to thermally activated dislocation movements, a phenomenon referred to as static recovery. The high dislocation density formed during dislocation creep at grain boundaries promotes diffusion processes there. Grain boundaries and especially grain boundary triple junctions therefore represent weak points where pores and microcracks form, which coalesce and lead to intergranular fracture.

### 1.1.2 Modeling Approaches

In literature, numerous approaches to model the material behavior of tempered high chromium martensitic steel can be found. Since the macro-mechanical material response is directly related to the microstructure, approaches also considering the microstructural features become important which then serve as a bridge from micro- to macroscale. These micromechanical models are defined by parameters referring to e.g the grain sizes or dislocation densities [151]. In [54], a dislocation-mechanics model is applied to depict the material behavior of high chromium steels at an elevated temperature of 873 K. It includes 20 material parameters and therefore needs a complex calibration procedure for their determination.

In order to predict the behavior of materials with complex microstructures at a larger scale, there are several methods in material science to describe the behavior of composite materials, multiphase alloys, and heterogeneous structures. Generally, composite models are proposed to describe materials that consist of multiple phases or constituents with different properties. They are applied in [148] to characterize austenitic stainless steel or in [14] to investigate the link between microstructure and effective diffusivity of cement. A particular composite model, the rule of mixtures as a continuum mechanical model, assumes that the material is a mixture of different phases or constituents that are homogeneously distributed throughout the material. It calculates the effective properties of the material by taking a weighted average of the properties of the individual phases [8]. The phase mixture model is well established in literature [128, 149] where an iso-strain concept depicts the hardening and softening behavior related to the microscale. The model is also implemented in [48, 87, 118] for tempered martensitic steel with high chromium content. The same approach combined with the HALPIN-TSAI equations is also used in [61] to examine epoxy-based glass fiber reinforced plastic composites.

Usually, these micromechanical models are calibrated by transmission electron microscopes [128, 149], hence they are more time consuming and expensive compared to macromechanical tests like the tensile test. With the intention of modeling the inelastic behavior of a realistic gas turbine or shaft, using a microscale model had the advantage of depicting the local deformation better, however, computing the stress-strain state would be connected to a tremendous numerical effort. Therefore, in this thesis, a phase mixture model transformed into a macroscopic mixture model is applied for both of the materials considered.

In general, two main categories of macromechanical models are provided in literature: unified and nonunified constitutive models [48, 73, 111]. The latter introduce an instantaneous

plastic strain apart from the time-dependent inelastic deformation. They define separate variables for both of them so that the definition of a yield surface is required to account for the boundaries of the elastic regime [71]. In [151], tempered martensitic steel is investigated using a nonunified elasto-viscoplastic model. The thermo-mechanical modeling of high chromium steel through a nonunified viscoplastic approach was the focus in [153]. It needs to be noted that there are three disadvantages [30, 48]: the term 'instantaneous' is not clearly defined, the correlation of the creep behavior with the instantaneous inelastic strain is not considered and the numerical implementation of two different flow rules due to the two separate variables may be challenging.

Unified approaches on the other hand allow for the representation of inelastic, time-dependent deformation processes such as dislocation mechanisms, diffusion processes or also pore growth. Examples include the ROBINSON model, the visco-plastic CHABOCHE model, the structure-independent material model according to PENKALLA, and others [20, 32, 89, 122]. They differ in the functional relationship between strain rate and stress state, as well as in the development equations for the internal variables. These models use a scalar internal variable to describe isotropic hardening and a tensorial internal variable to represent the kinematic hardening behavior, such as the BAUSCHINGER effect. The disadvantage of these models lies in the large number of material constants and evolution equations, which significantly increases the computational effort.

The commonly known unified constitutive model was originally proposed by ARMSTRONG and FREDERICK [56], including an equation to describe the inelastic strain rate tensor and also considering an evolution equation for the backstress tensor to capture nonlinear kinematic hardening according to CHABOCHE. Additionally, the idea of the backstress tensor was expanded by introducing the superposition of several backstresses where each of them has its own evolution equation leading to a more accurate description of cyclic behavior [31]. The approach is limited though, since the number of material parameters and hence the complexity of the model are increasing and so is the numerical effort. In [86], three backstresses in combination with a unified viscoplastic model depict kinematic hardening of a high chromium steel for the temperature range of  $773 \text{ K} \leq T \leq 873 \text{ K}$  resulting in more than 20 temperature-dependent parameters, because additional material parameters are necessary to account for the temperature dependence itself. The description of isotropic metals subjected to arbitrary thermomechanical loading with a unified model has been done in [13]. The model depicts the material behavior on a macroscopic level under monotonic as well as cyclic loading with the background of an aero-engine application. Unified viscoplastic approaches are also used to investigate high temperature fatigue of P91 steel including isotropic and kinematic hardening [11]. In [139], a constitutive model to simulate creep and cyclic loading of P91 and P92 steels is developed based on the CHABOCHE-type equations. The model accounts for a temperature range of  $673 \text{ K} \leq T \leq 873 \text{ K}$ . Another unified material model of high chromium steel is shown in [162]. Here, the temperature is kept constant for the simulation of the creep and fatigue behavior including nonlinear isotropic and kinematic hardening with a total of 27 material parameters. Regardless of the high number of material parameters that may need to be determined, the CHABOCHE model can still be found widely spread in literature and is also implemented as a material model in various commercial finite element method software packages [1].

### 1.1.3 Simulation Approaches

The simulation of structures subjected to cyclic thermo-mechanical loading has been and still remains a challenge. Involving non-linearities and a large number of fatigue cycles, it becomes an unaffordable cycle-by-cycle simulation [21]. Several approaches have been developed during the past years to decrease the computational time of analyzing the material behavior over many loading cycles since the calculations are numerically expensive due to the time integration procedures with very small time increments [4]. In general, there are three categories of multi-scale computational strategies in time: multi-time-step methods, the variational multiscale method in time and methods considering cyclic loadings [70]. Since the focus of this thesis is depicting the material's response to a cyclic profile, the other methods are only briefly introduced for the sake of completeness.

The **multi-time-step method** was originally introduced in [15, 16]. The basic idea is to divide the nodes of the mesh into groups which are solved using different time steps or also varying integration rules in the elements if necessary, so if a deformable solid occupies a domain, this is separated into subdomains, each associated with a temporal discretization and integration scheme. The technique is mostly applied in multiphysics when physical equations are not considering the same time scale to couple the resolutions. It is especially suitable for parallel computers but may not be considered a full multiscale approach, since the spatial area is still only taking one time scale into account [38, 70].

If a problem is formulated using partial differential equations (PDEs), the **variational multi-scale method** starts by defining a variational form where the boundary value problem can be transformed and is therefore much easier to solve. The next step is a multiscale decomposition into a large and a small scale. It was firstly proposed in [22] where it was applied for a hyperbolic problem and in [75] for parabolic equations. However, the formulations derived through the variational multiscale method exhibit strong resemblance to regularization techniques over time which is why it may be declared as a p-version in time of the finite element method (FEM). Here, the mesh remains fixed whereas the degree  $p$  of the polynomial approximation is incrementally raised until a desired level of accuracy is achieved. This characterization aligns them closer to a refinement strategy within the FEM rather than a genuine multiscale computation approach in time [70].

There are three approaches suitable for a temporal description of **cyclic loading conditions**: the large time increments (LATIN) method, the cycle jump method and the two-time-scale homogenization method [70] as schematically shown in Fig. 1.4.

In the beginning, the **LATIN method** usually uses the elastic solution to calculate a coarse approximation. This method is considered as non-incremental meaning that there is no need to partition the interval of interest into small segments but in each iteration, the method produces an approximation of the solution of the entire time span, thus significantly decreasing computational time [70]. In [35, 92, 93], the approach was newly developed and later extended for the application to cyclic loadings with a large number of cycles. The first step is to sort the equations into two categories where two solution sub spaces are introduced, a linear one  $S_l$  for the boundary and equilibrium conditions and a non-linear one  $S_{nl}$  for the constitutive equations. The goal is finding the intersection between them by applying an iterative procedure in two stages where initially, a solution  $s_0$  is estimated by an elastic calculation.

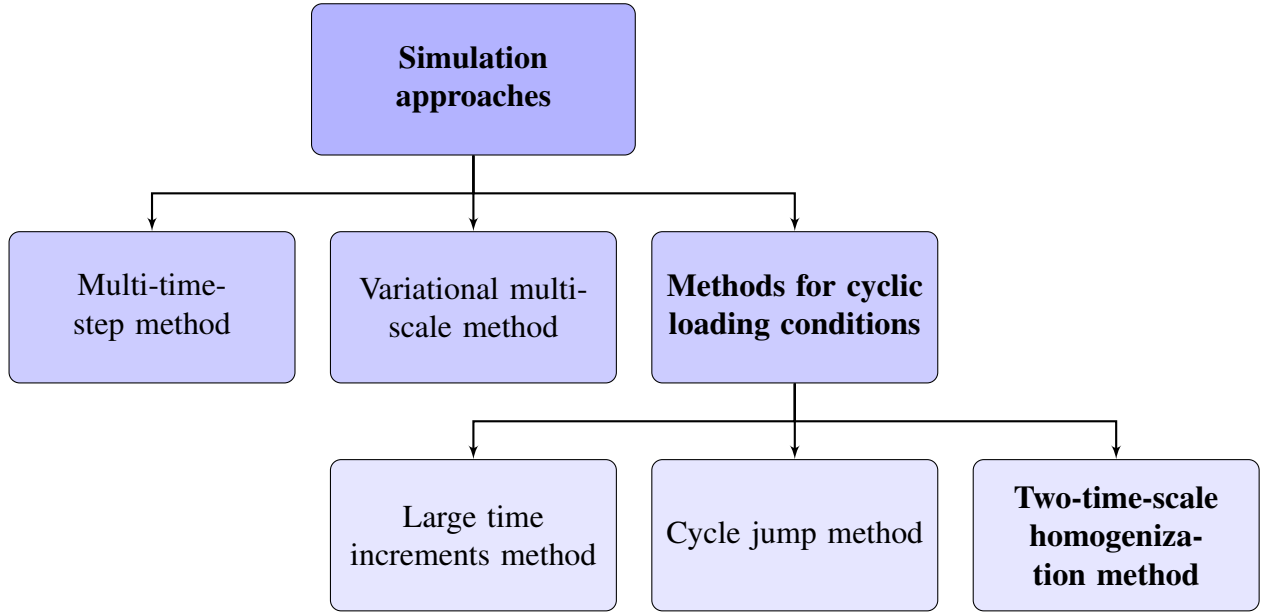


Figure 1.4: Overview of multi-scale computational strategies in time

When an element solution  $s_n$  of the linear subspace is known, the next solution  $s_{n+\frac{1}{2}}$  is determined in the non-linear one with a given search direction  $D^+$  which satisfies the constitutive equations and is part of  $S_{nl}$ . Afterwards, another element solution  $s_{n+1}$  of  $S_l$  is calculated in the opposite direction  $D^-$  so that the algorithm converges to the exact solution  $s$  eventually as shown in Fig. 1.5. The result is the splitting of the entire interval into sub intervals where each of them can depict tens or hundreds of cycles reducing the numerical calculation time significantly but at the same time, the implementation into the FEM software is too complex to be practically useful [70].

The **cycle jump technique** was firstly introduced in [99] to compute turbine paddels and was later also applied in [91] to predict the lifetime of a cylindrical specimen made of 316L steel using a fully coupled elastoplastic material model with fatigue damage. Assuming that the mechanical fields are not greatly changing from one cycle to the next, it is proposed to compute a larger interval containing a set of loading cycles. The evolution during these loading cycles is determined by extrapolating across the respective intervals. The concept is shown in Fig. 1.6,

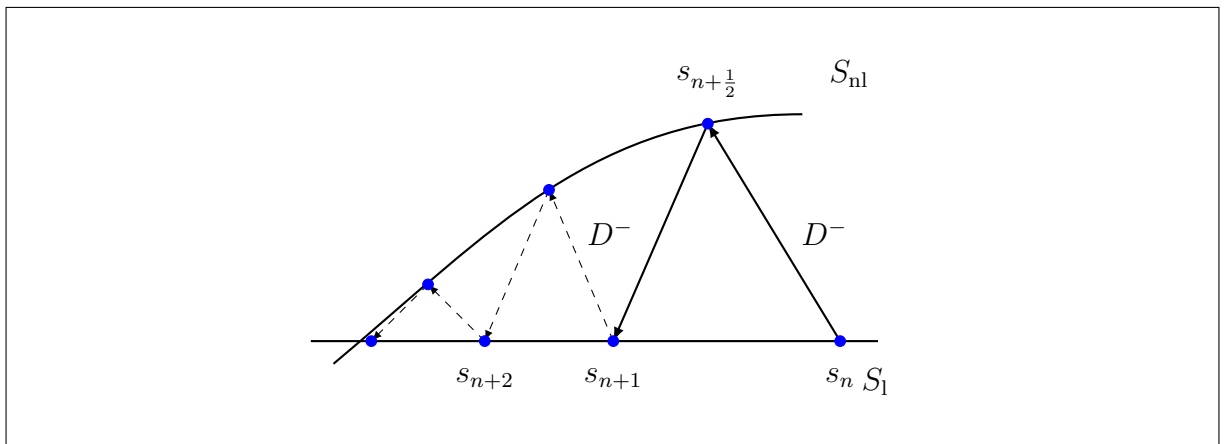


Figure 1.5: Principle of the LATIN algorithm after [92]

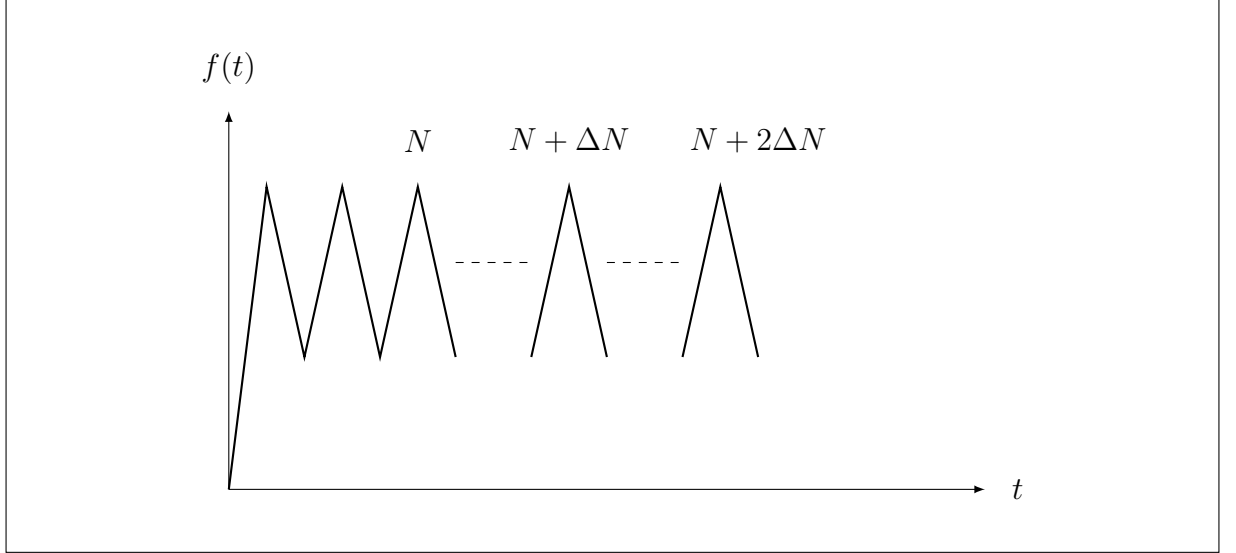


Figure 1.6: Schematic description of the cycle jump method after [70, 101]

where the mechanical quantities are described according to the number of cycles  $f(N)$ . In [36], multiple reference cycles are simulated to establish a function named the global evolution function which is used to extrapolate stresses, strains, and displacements over multiple cycles. The extrapolated state serves as the initial condition (IC) for the subsequent FEM simulation. Generally, the approach is able to treat large numbers of cycles but tends to be inaccurate for the first cycles, since the variables usually change significantly. The method is furthermore known to be effective but does not unconditionally guarantee the satisfaction of the governing equations [70].

The **two-time-scale homogenization method** is an application of the asymptotic spatial homogenization to time. The method was introduced in [66] for elasto-viscoplastic homogeneous materials. Originally, the approach was developed to solve differential equations of dynamical systems but is now also used to evaluate the inelastic material response [4]. The approach is based on the definition of two separate time scales, a slow and a fast one as also suggested in [123]. The slow or macro time is also referred to as physical time meaning it describes variations within the entire time interval of interest. The fast or micro one accounts for the rapidly varying behavior in the loading cycles. The technique can be utilized if the period of the fast time is much smaller than the total observation time. The original initial boundary value problem needs to be decomposed into a micro- and a macro-chronological problem where both of them are coupled. In [161], the approach served to describe thermo-viscoelastic composites, AUBRY and PUEL used it to predict the elasto-viscoplastic material response of a titanium alloy to a two-frequency cyclic load [9]. The method has also been applied to investigate the fatigue of titanium aluminum alloys during crystal plasticity finite element simulations [105] as well as with a biomechanical background, when the fatigue damage evolution of a bone was simulated in [44]. A combination of the multiscaling and the cycle jumping scheme can be found in [21] to enhance combined cycle fatigue calculations. Due to its wide range of application and mathematical rigorousness, the two-time-scale homogenization method will be implemented in this thesis at hand to model the inelastic behavior of high-temperature steels exerted to variable loading conditions. It will be further described in Sect. 2.5.

## **1.2 Outline**

The aim of the work at hand is to establish a numerical procedure that depicts the behavior of high-temperature steels subjected to a large number of cycles with reduced computational time. The two-time-scale approach is therefore applied to the material models of two specific alloys, namely X20CrMoV12-1 and X12CrMoWVNbN10-1-1, and is validated using the results of FEM simulations as well as experimental data.

The thesis consists of six chapters, starting with this introduction including general information concerning the materials themselves, their application and the literature research. Chapter 2 explains the theoretical foundations, covering key equations in continuum mechanics from the fields of kinematics, kinetics, balance laws, and constitutive equations, with a focus on rate-dependent inelasticity. It also introduces the principle of the two-time-scale approach, examining the asymptotic series expansion and the additive decomposition of the problem into a macrochronological and microchronological part. Afterwards, several time integration methods are briefly discussed which serve the purpose of implementing the constitutive equations in conjunction with the temporal multiscale technique in the form of a Python code.

The next chapter deals with the constitutive equations of the phase mixture model describing X20CrMoV12-1 steel and is mainly divided into two parts; the cycle-by-cycle or also called fully resolved simulations and the solution including the newly introduced two time scales. Each of them includes detailed information about their implementation and validation emphasizing cyclic benchmarks such as low cycle fatigue (LCF) and thermo-mechanical fatigue (TMF) tests where the temperature ranges from 500 – 650°C. These simulations depict the mechanical behavior under realistic operating conditions of power plant components, the reference results were gained using the FEM software ABAQUS.

The structure of the fourth chapter is identical to the third but it addresses the material response of X12CrMoWVNbN10-1-1 steel. The constitutive equations are derived, implemented and validated using experimental data in addition to the FEM results.

Due to a deviation between the multiscale computation and the experimental results, the evolution equation for the softening variable is discussed and adapted with respect to periodic loading conditions. The adjustment is presented in Chapt. 5, afterwards, the two-time-scale approach is employed to calculate the material parameter needed for the newly introduced equation. In the last chapter, the findings and results of the thesis are summarized and suggestions for further research regarding the topic are given. The thesis presents an efficient and experimentally validated two-time-scale simulation framework applied to two key high-temperature steel alloys, offering a significant computational advantage over existing methods in literature.

## 2 Theoretical Background

This section first provides a qualitative description of the cyclic material behavior followed by a brief overview of the basic concepts in continuum mechanics as the foundation for the subsequent chapters. In addition, the two-time-scale homogenization procedure is further introduced.

### 2.1 Cyclic Material Behavior

High-temperature components are typically subjected not only to primary creep stresses resulting from constant mechanical loading but also to secondary stresses induced by temperature fluctuations during service. These thermally induced strains and stresses lead to complex loading conditions where creep and fatigue mechanisms interact, often simultaneously affecting material performance over time [81, 98, 145]. To quantitatively predict the cyclic material behavior, it is essential to examine the material's stress–strain response under cyclic loading conditions. This work focuses on strain-controlled cyclic loading without dwell times, which is a common testing method to study the low-cycle fatigue behavior. In the inelastic domain, materials exhibit a characteristic stress–strain hysteresis loop where the enclosed area of this loop corresponds to the plastic work dissipated per cycle and is an indicator of the energy loss due to irreversible deformation [90].

After a strain reversal, the onset of inelastic deformation is reduced by the same amount it was increased prior to the reversal which is known as the Bauschinger effect. The tensile and compressive yield points shift in the same direction after an inelastic deformation, which is referred to as kinematic hardening [31, 56, 145]. Repeated cyclic loading with a constant strain amplitude leads, depending on the material, to either cyclic softening or cyclic hardening. This manifests as a uniform decrease or increase in the yield points and is referred to as isotropic softening or hardening, respectively [98].

The yield behavior under multiaxial loading can generally be described using the principal stresses  $\sigma_I$  and  $\sigma_{II}$ , while keeping  $\sigma_{III}$  constant. This behavior is represented by a yield surface in the  $\sigma_I - \sigma_{II}$  stress plane. Isotropic hardening is depicted as an expansion of the yield surface, as shown in Fig. 2.1. In contrast, kinematic hardening is characterized by a translation of the yield surface without changing its shape, size, or orientation [85]. Microstructurally, isotropic and kinematic hardening are associated with different changes in dislocation density within the material and the mobility of dislocations, depending on the material's deformation history [31, 107, 133].

The cyclic stress–strain behavior is commonly characterized using the cyclic yield curve, which can be obtained by halving the flank curve of a hysteresis loop [126, 138]. To determine this curve, the material is subjected to cyclic loading with a fixed load ratio while progressively reducing the strain amplitude, eventually reaching the purely elastic regime. This process serves to eliminate any accumulated kinematic and isotropic hardening or softening effects, after which a monotonic loading is applied to gain the quasi-static yield curve. This approach enables a direct comparison with the initial static yield curve, which represents the material

## 2 Theoretical Background

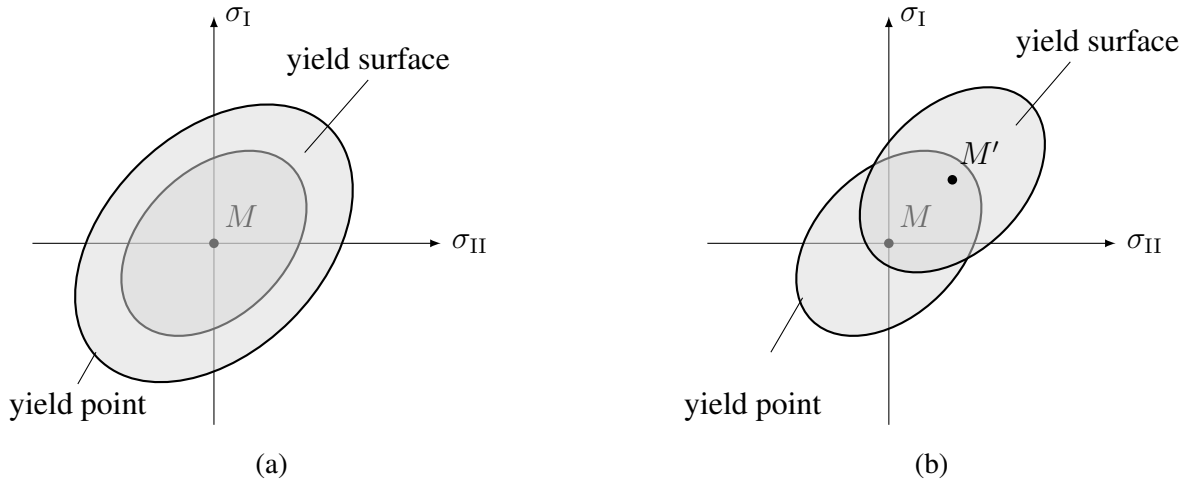


Figure 2.1: Evolution of the yield surface under isotropic expansion (a) and under kinematic translation (b)

in its virgin condition, thereby revealing the changes in deformation behavior resulting from cyclic loading [108]. However, quasi-static yield curves are independent of holding times and depend solely on the degree of fatigue damage describing cyclic material behavior better. Furthermore, due to their independence from the specific cycle shape, quasi-static yield curves are considered to be more universally applicable and transferable [108]. The schematical evolution of the softening with respect to the number of cycles  $N$  during a strain-controlled LCF test is depicted in Fig. 2.2, a typical profile of an LCF test at a constant temperature with and without dwell times including the corresponding stress result is shown in Fig. 2.3.

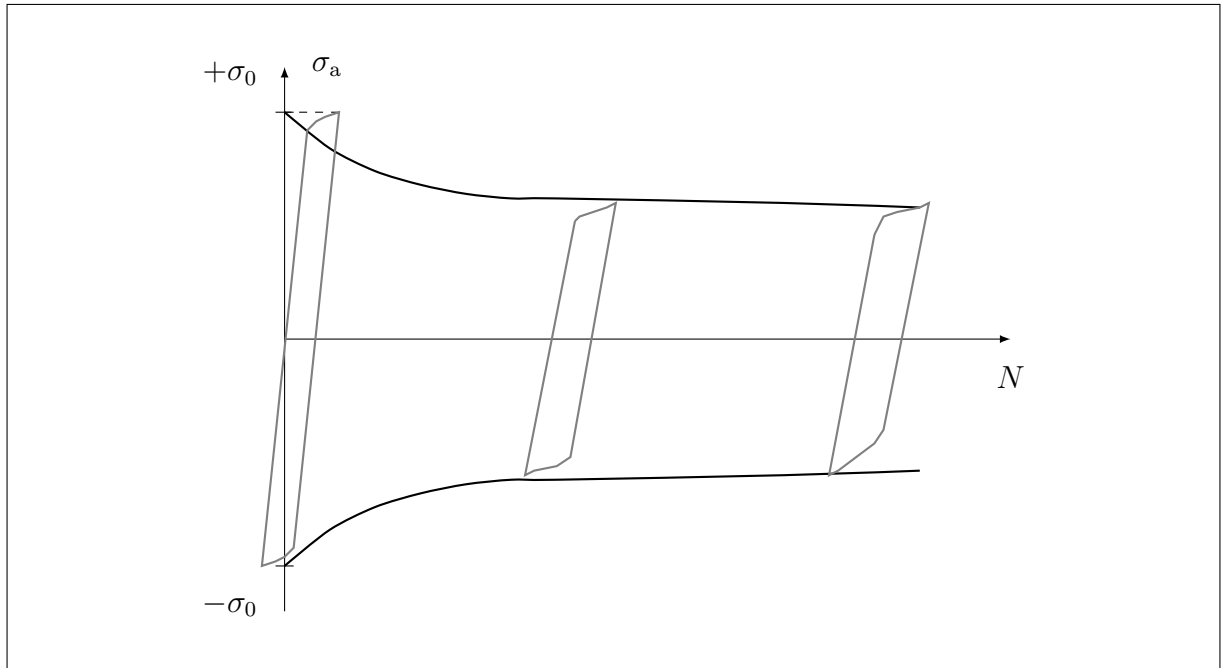


Figure 2.2: Qualitative evolution of the stress amplitude with respect to the number of LCF cycles, after [121]



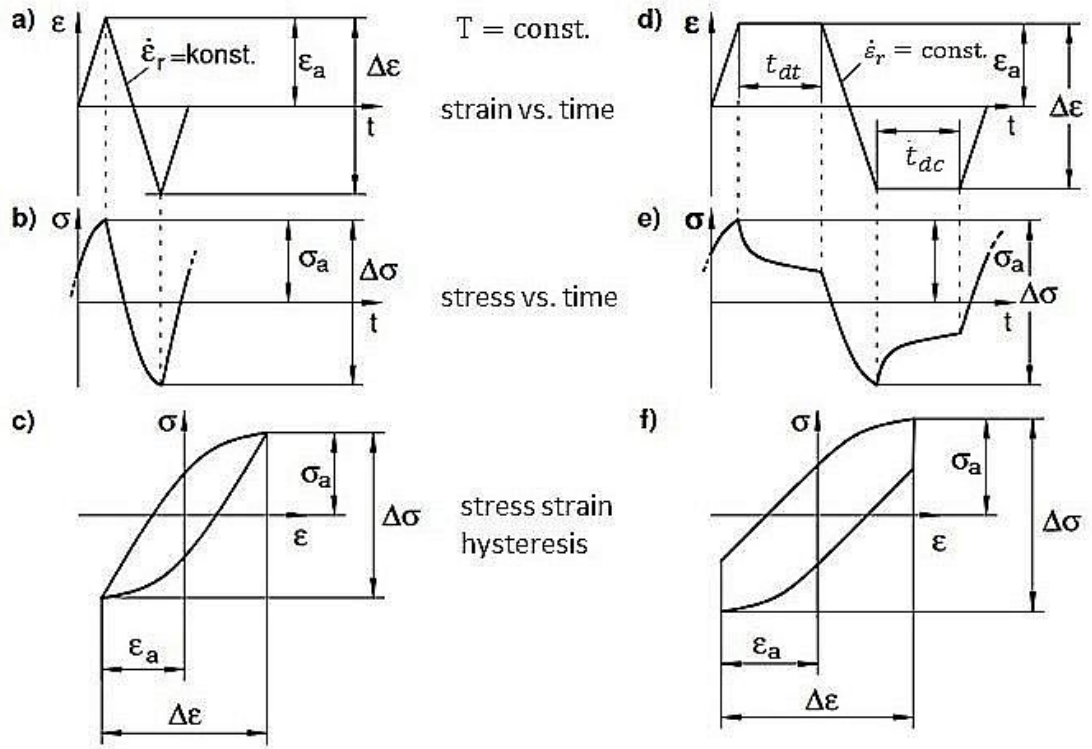


Figure 2.3: Strain-controlled loading path without (a–c) and with dwell times (d–f) marked as  $t_{dt}$  in the tensile region and  $t_{dc}$  in the compressive loading regime<sup>1</sup>

High-temperature components in turbine systems are subjected to complex thermal and mechanical loading conditions. During start-up, shutdown, and power fluctuations, transient temperature gradients develop across component cross-sections. These non-steady thermal fields, combined with variable mechanical loads, result in local changes in the stress and strain state, often involving localized plastic deformation [74, 141]. Under steady-state operation, creep phenomena, including time-dependent deformation, stress relaxation and redistribution, and microstructural evolution typically dominate [110]. The interaction of cyclic and time-dependent loading is often a critical factor in determining the component's life. A realistic material model requires a unified constitutive framework capable of capturing inelastic material behavior under non-steady, multiaxial mechanical loads and transient temperature profiles with sufficient accuracy. Such models enable a consistent representation of mechanisms such as plasticity, creep, stress relaxation, cyclic hardening as well as softening, and cyclic creep [32, 89, 122, 146]. Even within the high-temperature range and at moderate stress levels, a unified description can be challenging due to the dominance of different deformation and damage mechanisms depending on temperature and stress [112, 115]. For practical applications, it is therefore often usual to model plasticity (high strain rates, lower temperatures) and creep (low strain rates, high temperatures) using separate constitutive laws. For example, [74, 141] classify typical start-up procedures into cold, warm and hot starts. Cold starts are typically modeled using plasticity models with isotropic and kinematic hardening, whereas warm and hot starts and holding phases are generally analyzed using creep models, also incorporating isotropic and

<sup>1</sup>Kostenko, Y., Almstedt, H., Scholz, A., Linn, S., Naumenko, K., Kutschke, A., Prygorniev, O. (2012). Langzeitdehnverhalten (LCF-Ermüdung) von großen Dampfturbinenkomponenten im Hochtemperaturbereich. Verbundprojekt COORETEC-Turbo III.

kinematic hardening [74, 116] The following sections present a constitutive model developed to describe the inelastic behavior of 9–12% Cr steels under low strain rate conditions based on the continuum mechanics background.

## 2.2 Continuum Mechanics

The basic principles of continuum mechanics can be distinguished between kinematics and kinetics. The primary objective is to characterize the spatial and temporal motion of deformable bodies within a three-dimensional space, called the EUCLIDEAN space where geometric elements such as points or straight lines can be described and distances or angles may be quantified [6, 19, 147]. The spatial motion is defined by the Cartesian coordinate system and for the temporal aspect we differentiate between the current and the reference configuration. The reference configuration depicts the state at the initial time  $t = t_0$ , while the current one refers to the actual time  $t > t_0$  [6, 111]. The connection between both is done using the deformation gradient  $\mathbf{F}$ , a second rank tensor. It can be expressed in EULERian form which is usually done when dealing with fluid mechanics but for solid mechanics, the LAGRANGian form is considered. Equation (2.1) presents the LAGRANGian deformation gradient [6]

$$\mathbf{F}(\mathbf{a}, t) = (\nabla_{\mathbf{a}} \mathbf{x}(\mathbf{a}, t))^T \quad \text{respectively} \quad F_{ij} \mathbf{e}_i \mathbf{e}_j = \frac{\partial x_j}{\partial a_i} \mathbf{e}_i \mathbf{e}_j. \quad (2.1)$$

With the description of the deformation from reference to actual configuration as

$$\mathbf{x} = \mathbf{x}(\mathbf{a}, t) \quad (2.2)$$

the transformation of a line element  $d\mathbf{a}$  in the reference configuration into a line element  $d\mathbf{x}$  of the actual form yields

$$d\mathbf{x} = \mathbf{F} \cdot d\mathbf{a}. \quad (2.3)$$

The tensor  $\mathbf{F}$  has a positive determinant  $\det(\mathbf{F}) > 0$  where  $\det(\mathbf{F}) = 1$  for  $t = t_0$  [6]. The inverse is needed if the line element  $d\mathbf{x}$  is supposed to be transformed back to  $d\mathbf{a}$ , schematically depicted in Fig. 2.4

$$d\mathbf{a} = \mathbf{F}^{-1} \cdot d\mathbf{x} \quad \text{with} \quad \mathbf{F}^{-1} = \frac{\partial a_i}{\partial x_j} \mathbf{e}_i \mathbf{e}_j. \quad (2.4)$$

Furthermore, the tensor  $\mathbf{F}$  is not symmetric resulting in complications when performing some mathematical operations. To omit these, the CAUCHY-GREEN tensor  $\mathbf{C}$  is often used

$$\mathbf{C} = \mathbf{F}^T \cdot \mathbf{F} = (\nabla \mathbf{u})^T \cdot \nabla \mathbf{u} + \nabla \mathbf{u} + (\nabla \mathbf{u})^T + \mathbf{I}. \quad (2.5)$$

Here,  $\mathbf{I}$  represents the unit tensor and  $\mathbf{u}$  defines the displacement vector.

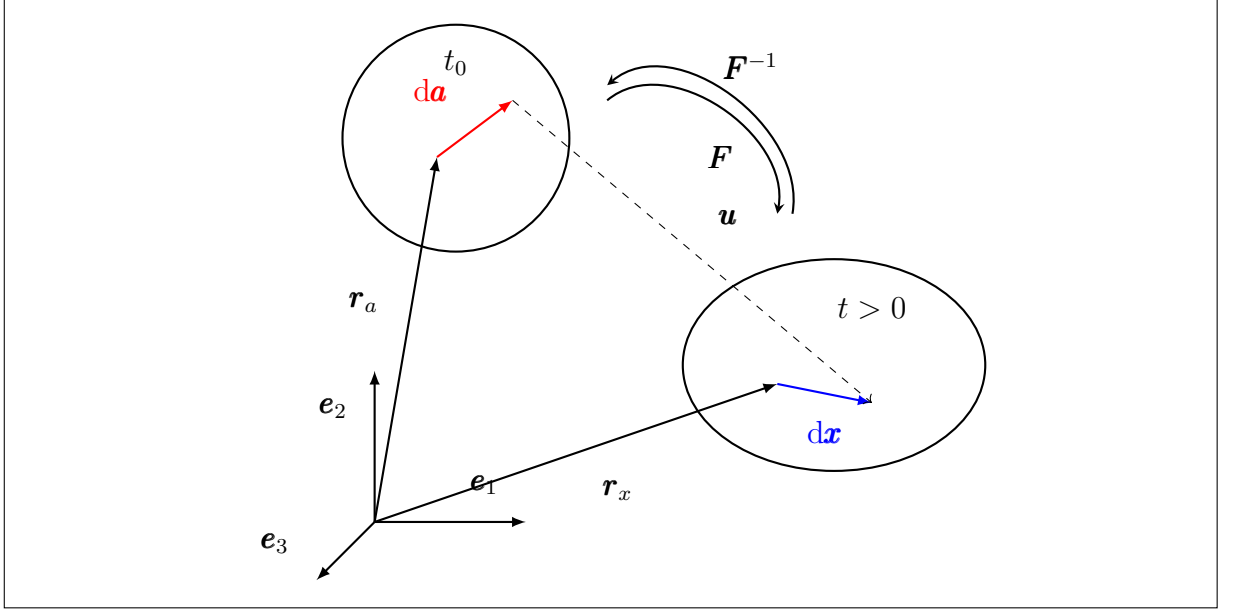


Figure 2.4: Change of line segment  $d\mathbf{a}$  in the reference configuration at time  $t_0$  (red arrow) in comparison to  $d\mathbf{x}$  in the actual configuration (blue arrow) after deformation  $\mathbf{u}$

The tensor  $\mathbf{C}$  holds the additional advantage of being invariant with respect to rigid body motions leading to this tensor as basis for the definition of different strain tensors such as the GREEN strain tensor, see Eq. (2.6) [6, 147]

$$\mathbf{E}^G = \frac{1}{2}(\mathbf{C} - \mathbf{I}) = \frac{1}{2} [(\nabla \mathbf{u})^T \cdot \nabla \mathbf{u} + \nabla \mathbf{u} + (\nabla \mathbf{u})^T]. \quad (2.6)$$

Due to the term  $(\nabla \mathbf{u})^T \cdot \nabla \mathbf{u}$  the GREEN strain tensor is nonlinear with respect to the displacement gradient. When restricted to small deformations, it then reduces to the linear strain tensor, also called engineering strain tensor  $\boldsymbol{\varepsilon}$

$$\boldsymbol{\varepsilon} = \frac{1}{2} [\nabla \mathbf{u} + (\nabla \mathbf{u})^T]. \quad (2.7)$$

This kinematic equation will be part of the initial boundary value problem considered in the following sections.

In order to not only examine motion and deformation but also the load causing them, the kinetic equations are needed. Generally, they can be calculated using the cut principle which is widely applied [6, 19]. The basic idea is to separate the material body from its environment and express the interaction with it by forces and moments. These influences can be classified as body, volume or surface loads. Considering the surface forces, also called contact forces, leads to the stress vector  $\mathbf{t}$  [6]

$$\mathbf{t} = \lim_{\Delta A \rightarrow 0} \frac{\Delta \mathbf{f}}{\Delta A}. \quad (2.8)$$

The CAUCHY lemma describes the relation between the stress vector  $\mathbf{t}$  and the stress tensor  $\boldsymbol{\sigma}$ .

## 2 Theoretical Background

It is a linear function of the normal vector  $\mathbf{n}$  of the area element  $\Delta A$  referred to [6, 19, 147]

$$\mathbf{t} = \mathbf{n} \cdot \boldsymbol{\sigma}. \quad (2.9)$$

In Eq. (2.9),  $\boldsymbol{\sigma}$  describes the CAUCHY stress tensor which is known to be symmetric. Further examining Eq. (2.8) from an experimental perspective shows that the current force and area have to be measured which is more complicated than measuring the area in the reference configuration. Therefore, another definition of the stress vector with respect to the element  $\Delta A_0$  in the reference configuration is described

$$\mathbf{t}_{\text{PK}} = \lim_{\Delta A_0 \rightarrow 0} \frac{\Delta \mathbf{f}}{\Delta A_0}. \quad (2.10)$$

Inserting the new stress vector  $\mathbf{t}_{\text{PK}}$  into Eq. (2.9) yields the PIOLA-KIRCHHOFF stress tensor  $\mathbf{P}$ , also known as engineering stress tensor

$$\mathbf{t}_{\text{PK}} = \mathbf{n}_0 \cdot \mathbf{P}. \quad (2.11)$$

Using the deformation gradient, the PIOLA-KIRCHHOFF stress tensor can also be calculated from the CAUCHY stress tensor according to [6]

$$\mathbf{P} = \det(\mathbf{F}) \mathbf{F}^{-1} \cdot \boldsymbol{\sigma}. \quad (2.12)$$

Due to the non symmetry of the deformation gradient, this property is passed on to the tensor  $\mathbf{P}$ . By introducing a new surface force vector  $\Delta \mathbf{f}_0$  in the reference configuration, calculating the stress vector according to it and inserting it again into Eq. (2.9), the second PIOLA-KIRCHHOFF stress tensor  $\mathbf{S}$  can be computed [6]

$$\Delta \mathbf{f}_0 = \mathbf{F}^{-1} \cdot \Delta \mathbf{f}, \quad (2.13)$$

$$\mathbf{t}_{\text{PKII}} = \lim_{\Delta A_0 \rightarrow 0} \frac{\Delta \mathbf{f}_0}{\Delta A_0}, \quad (2.14)$$

$$\mathbf{t}_{\text{PKII}} = \mathbf{n}_0 \cdot \mathbf{S}. \quad (2.15)$$

This tensor is now symmetric and therefore a lot easier to treat. It can also be calculated using the CAUCHY stress tensor with the following equation

$$\mathbf{S} = \det(\mathbf{F}) \mathbf{F}^{-1} \cdot \boldsymbol{\sigma} \cdot \mathbf{F}^{-\text{T}}. \quad (2.16)$$

Based on the findings from the kinematic and kinetic equations, the mechanical balance laws for the mass, the linear momentum, and angular momentum can be derived. The general form of any balance law holds [6]

$$\frac{\text{D}}{\text{D}t} \int_m \boldsymbol{\Psi}(\mathbf{x}, t) \, \text{d}m \equiv \frac{\text{D}}{\text{D}t} \int_V \boldsymbol{\Psi}(\mathbf{x}, t) \rho \, \text{d}V = \int_A \mathbf{n} \cdot \boldsymbol{\Phi}(\mathbf{x}, t) \, \text{d}A + \int_V \boldsymbol{\Xi}(\mathbf{x}, t) \rho \, \text{d}V, \quad (2.17)$$

where  $\boldsymbol{\Psi}(\mathbf{x}, t)$  and  $\boldsymbol{\Xi}(\mathbf{x}, t)$  are tensor fields of the same rank  $n$ ,  $\boldsymbol{\Phi}(\mathbf{x}, t)$  denotes a tensor field of the rank  $n + 1$ ,  $\mathbf{n}$  defines the normal of the surface  $A$  and  $m(\mathbf{x}, t)$  means the mass as a function

## 2 Theoretical Background

of the volume. Equation (2.17) states that the rate of change of the balance quantity  $\Psi(\mathbf{x}, t)$  is equal to the sum of inflow and outflow across the surface  $A$  of the body and the increase or decrease of the balance quantity within the body. The term  $\Phi(\mathbf{x}, t)$  represents the flow of the balance quantity  $\Psi(\mathbf{x}, t)$  through  $A$  in the direction of  $\mathbf{n}$ . The variable  $\Xi(\mathbf{x}, t)$  represents the positive or negative growth of the balance quantity in  $V$ . We focus on an infinitesimal material volume element  $dV$ . Its mass  $dm$  can be calculated using the density  $\rho$  [6, 111]

$$dm = \rho dV. \quad (2.18)$$

The assumption of mass conservation then yields

$$dm = \rho dV = \rho_0 dV_0. \quad (2.19)$$

Starting from Eq. (2.17), one finds  $\Psi(\mathbf{x}, t) \rightarrow 1$  to be a scalar field,  $\Phi(\mathbf{x}, t) = 0$  since there is no mass exchange across the surface and  $\Xi(\mathbf{x}, t) \rightarrow 0$  because there is no internal change of the mass due to production or supply

$$\frac{Dm}{Dt} = \frac{D}{Dt} \int_V \rho(\mathbf{x}, t) dV = \frac{\partial}{\partial t} \int_{V_0} \rho_0(\mathbf{a}) dV_0 = 0. \quad (2.20)$$

In order to formulate the balance of linear momentum, the vector of linear momentum  $\mathbf{p}$  needs to be calculated with the velocity vector  $\mathbf{v}$  as follows

$$d\mathbf{p} = \mathbf{v} dm = \mathbf{v} \rho dV. \quad (2.21)$$

According to EULER's first law of motion the rate of change of the linear momentum during the deformation of a body is equal to the sum of all external surface and volume forces acting on the body [6]. The balance of linear momentum then yields

$$\frac{D}{Dt} \int_V \mathbf{v}(\mathbf{x}, t) \rho(\mathbf{x}, t) dV = \int_A \mathbf{t}(\mathbf{x}, \mathbf{n}, t) dA + \int_V \mathbf{k}(\mathbf{x}, t) \rho(\mathbf{x}, t) dV, \quad (2.22)$$

which refers back to the general balance law Eq. (2.17) with  $\Psi = \mathbf{v}$ ,  $\Phi = \mathbf{T}$  and  $\Xi = \mathbf{k}$

$$\frac{D}{Dt} \int_V \mathbf{v} \rho dV = \int_A \mathbf{n} \cdot \mathbf{T} dA + \int_V \mathbf{k} \rho dV, \quad (2.23)$$

$$d\dot{\mathbf{p}} = \mathbf{t} dA + \rho \mathbf{k} dV. \quad (2.24)$$

Here, the dot denotes the first derivative with respect to time, the vector  $\mathbf{k}$  summarizes all body forces. If now the CAUCHY stress tensor from Eq. (2.9) is inserted in Eq. (2.24) and the GAUSS-OSTROGRADSKY theorem is applied which allows for the transformation of the surface integral into a volume integral we get

$$\nabla \cdot \boldsymbol{\sigma} + \rho \mathbf{k} = \rho \dot{\mathbf{v}}. \quad (2.25)$$

The balance of angular momentum can be derived analogously to the balance of linear momentum. First, the vector of angular momentum  $\mathbf{l}$  has to be defined [6, 111]

$$d\mathbf{l} = \mathbf{x} \times \mathbf{v} dm = \mathbf{x} \times \mathbf{v} \rho dV. \quad (2.26)$$

## 2 Theoretical Background

The balance of angular momentum states that the rate of change of the total angular momentum of a body with respect to a chosen point is equal to the total moment of all external surface and volume forces acting on the body at the chosen point

$$\frac{D}{Dt} \int_V \mathbf{x} \times \rho \mathbf{v} dV = - \int_A \mathbf{n} \cdot \mathbf{T} \times \mathbf{x} dA + \int_V \mathbf{x} \times \rho \mathbf{k} dV, \quad (2.27)$$

$$d\dot{\mathbf{l}} = \mathbf{x} \times \mathbf{t} dA + \rho \mathbf{x} \times \mathbf{k} dV. \quad (2.28)$$

Performing some mathematical operations leads to Eq. (2.28) proving the symmetry of the CAUCHY stress tensor for nonpolar media [6, 19, 111]

$$\boldsymbol{\sigma} = \boldsymbol{\sigma}^T. \quad (2.29)$$

The balance of energy or the first law of thermodynamics

$$\frac{d}{dt} E_e = L_e + Q_e \quad (2.30)$$

states that the rate of change of the energy of a body equals the mechanical power  $L_e$  plus the rate of change of non-mechanical energy  $Q_e$ . In order to account for the thermodynamic consistency of the material models presented in Chapt. 3 and Chapt. 4, the second law of thermodynamics in the form of the CLAUSIUS-PLANCK inequality

$$\frac{d}{dt} S_e - \left( \frac{Q}{T} \right)_e \geq 0 \quad (2.31)$$

has to be fulfilled [37, 111, 150]. Here,  $S$  describes the entropy and  $T$  the absolute temperature showing that the entropy production is always non-negative. The Eqs. (2.30) and (2.31) are stated for the sake of completeness but will not be applied within this work since the two material models considered were already proven to be thermodynamically consistent.

### 2.3 Constitutive Equations of the Phase Mixture Model

The goal of describing a certain material behavior can not be achieved only by the before mentioned equations. In order to close this gap, the constitutive equations relating stresses to strains are crucial which in this case, have been limited to isotropic materials where the material properties do not depend on specific directions. Additionally, the rule of mixtures is applied for the material model of both high-temperature steels. For this reason, the approach is now briefly introduced and afterwards, the constitutive equations with respect to the mixture are derived.

This type of model has already been treated in the 70s as documented in [8] and was continuously examined in [106, 114, 134]. In this study, we investigate a mixture composed of two distinct nonreacting solid components, meaning a 'hard' and a 'soft' phase which are denoted by the indices h and s. This characterization is with respect to the inelastic behavior since both phases are assumed to exhibit the same elastic behavior. Typically, a continuum mechanical framework is established for each of them separately, involving the formulation of kinematic equations, balance laws, and constitutive equations specific to each constituent.

## 2 Theoretical Background

Subsequently, these constituents are combined into a mixture by defining their interactions. Two basic concepts can be distinguished: the iso-strain concept and the iso-stress approach. The first was developed by VOIGT in [152] under the assumption of a homogenous strain field with the two constituents marked by the indices h and s [113]

$$\boldsymbol{\varepsilon}_h = \boldsymbol{\varepsilon}_s = \boldsymbol{\varepsilon} \quad (2.32)$$

and the latter was proposed by REUSS implying a homogeneous stress field [137]

$$\boldsymbol{\sigma}_h = \boldsymbol{\sigma}_s = \boldsymbol{\sigma}. \quad (2.33)$$

The material models presented in this work contain two phases and are supposed to account for hardening and softening based on the stress redistribution [48, 113, 149] so that the stress is defined based on the iso-strain ansatz as

$$\boldsymbol{\sigma} = \eta_h \boldsymbol{\sigma}_h + \eta_s \boldsymbol{\sigma}_s \quad \text{with} \quad \eta_h + \eta_s = 1. \quad (2.34)$$

In Eq. (2.34), the variables  $\eta_h$  and  $\eta_s$  refer to the volume fractions of each component [46, 127] where the approximation according to this rule of mixtures was already successfully used. To fully describe the mixture, an evolution equation for one of the phases is needed, since they are directly depending on each other. Here, the hard phase was chosen

$$\dot{\eta}_h = f_\eta(\boldsymbol{\sigma}_h, \hat{\varepsilon}_h^{\text{in}}, T). \quad (2.35)$$

Generally, the material models for the two steels considered are based on the additive decomposition of the strain tensor  $\boldsymbol{\varepsilon}$  into an elastic and an inelastic part [48, 111, 113, 116]

$$\boldsymbol{\varepsilon} = \boldsymbol{\varepsilon}_p^{\text{el}} + \boldsymbol{\varepsilon}_p^{\text{in}}. \quad (2.36)$$

The subscript p indicates the considered phase so that  $p \in \{h, s\}$ .

### 2.3.1 Elasticity

Elasticity describes rate-independent material behavior without hysteresis hence the stress state is only a function of the deformation which, in the case of linear isotropic elasticity, is expressed through HOOKE's law

$$\boldsymbol{\sigma} = K \text{tr}(\boldsymbol{\varepsilon}) \mathbf{I} + 2G\boldsymbol{\varepsilon}^{\text{el}} \quad \text{with} \quad \text{tr}(\boldsymbol{\varepsilon}) = \varepsilon_V \quad (2.37)$$

or, with respect to the two constituents

$$\boldsymbol{\sigma}_p = K \text{tr}(\boldsymbol{\varepsilon}_p) \mathbf{I} + 2G\boldsymbol{\varepsilon}_p^{\text{el}} \quad \text{with} \quad \text{tr}(\boldsymbol{\varepsilon}_p) = \varepsilon_{V_p}, \quad (2.38)$$

where  $\varepsilon_V$  denotes the volumetric strain. The superscript  $\square^{\text{el}}$  indicates all elastic variables. In Eq. (2.37) it becomes obvious, that the stress response does not depend on the deformation path or time. The material parameters included are the bulk modulus  $K$  and the shear modulus  $G$  which themselves are expressed as functions of the YOUNG's modulus  $E$  and the POISSON's

## 2 Theoretical Background

ratio  $\nu$  in the following way

$$G = \frac{E}{2(1+\nu)}, \quad K = \frac{E}{3(1-2\nu)}. \quad (2.39)$$

The elastic law may also be rewritten in terms of the two LAMÉ parameters  $\lambda$  and  $\mu$

$$\boldsymbol{\sigma} = \lambda \operatorname{tr}(\boldsymbol{\varepsilon}) \mathbf{I} + 2\mu \boldsymbol{\varepsilon} \quad (2.40)$$

with

$$\lambda = \frac{E\nu}{(1+\nu)(1-2\nu)} = K - \frac{2}{3}G, \quad \mu = G. \quad (2.41)$$

Due to the assumption of the two phases having the same elastic behavior, these material parameters are also equal for both of them. Making use of the decomposition of the stress tensor into a spheric and a deviatoric part

$$\boldsymbol{\sigma}_p = \sigma_{\text{mean}_p} \mathbf{I} + \boldsymbol{\sigma}'_p \quad \text{with} \quad \sigma_{\text{mean}_p} = \frac{1}{3} \operatorname{tr}(\boldsymbol{\sigma}_p), \quad \operatorname{tr}(\boldsymbol{\sigma}'_p) = 0 \quad (2.42)$$

results in a reformulation of Eq. (2.38) with respect to the elastic strain

$$\boldsymbol{\varepsilon}_p^{\text{el}} = \frac{\sigma_{\text{mean}_p}}{3K} \mathbf{I} + \frac{\boldsymbol{\sigma}'_p}{2G}. \quad (2.43)$$

In Eqs. (2.42) and (2.43),  $\sigma_{\text{mean}_p}$  denotes the mean stress, whereas the prime  $\square'$  defines traceless tensors, also called deviators. Additionally, it can be shown that the mean stress is the same throughout the mixture by using the trace operator on Eqs. (2.32), (2.36) and (2.43) resulting in

$$\operatorname{tr}(\boldsymbol{\varepsilon}) = \operatorname{tr}(\boldsymbol{\varepsilon}_h) = \operatorname{tr}(\boldsymbol{\varepsilon}_s), \quad (2.44)$$

$$\varepsilon_V = \varepsilon_{V_h} = \varepsilon_{V_s}, \quad (2.45)$$

$$\varepsilon_V = \varepsilon_{V_p}^{\text{el}} + \varepsilon_{V_p}^{\text{in}}, \quad (2.46)$$

$$\varepsilon_{V_p}^{\text{el}} = \frac{\sigma_{\text{mean}_p}}{K} \quad (2.47)$$

and applying the assumption of the classical theory of inelasticity that the change in volume of the inelastic deformation is neglectable [48] yields

$$\varepsilon_{V_p}^{\text{in}} = 0, \quad (2.48)$$

$$\sigma_{\text{mean}} = \sigma_{\text{mean}_h} = \sigma_{\text{mean}_s} = K\varepsilon_V. \quad (2.49)$$

Now, Eqs. 2.32 and 2.34 can be reformulated with respect to the deviators as

$$\boldsymbol{\varepsilon}' = \boldsymbol{\varepsilon}'_h = \boldsymbol{\varepsilon}'_s \quad (2.50)$$



and

$$\boldsymbol{\sigma}' = \eta_s \boldsymbol{\sigma}'_s + \eta_h \boldsymbol{\sigma}'_h = (1 - \eta_h) \boldsymbol{\sigma}'_s + \eta_h \boldsymbol{\sigma}'_h. \quad (2.51)$$

### 2.3.2 Inelasticity

The second part of the additive decomposition of the total strain in Eq. (2.36) needs to be defined. The inelastic behavior describes rate-dependent effects including hysteresis where the deformation is irreversible due to energy dissipating. The time-dependence caused by viscous effects is also taken into account.

Applying a unified constitutive model as explained in Subsect. 1.1.2, results in the term 'inelastic strains' meaning all irreversible deformation processes, without the definition of a yield surface, cf. [107] summarized by the inelastic strain tensor  $\boldsymbol{\varepsilon}^{\text{in}}$ . Furthermore, the presented model is restricted to small displacements, rotations and also deformations. These limitations are motivated by the computational time on one hand, since including finite strains or displacements would lead to an increased computational effort [48, 160]. On the other hand, they are also physically justified, because the considered power plant components are not allowed to exhibit large deformation states for the sake of safety.

The derivation of the inelastic part of the constitutive equations for the phase-mixture-model using internal variables is based on [48, 111, 113, 116]. In general, we consider tensorial internal variables defined as  $\boldsymbol{Q}_i \forall i \in \{1, 2, \dots, m\}$  and scalar internal variables  $q_j \forall j \in \{1, 2, \dots, n\}$  so that the stress tensor  $\boldsymbol{\sigma}$  not only depends on the strain tensor  $\boldsymbol{\varepsilon}$  but also on the internal state variables yielding

$$\boldsymbol{\sigma} = f(\boldsymbol{\varepsilon}, \boldsymbol{Q}_i, q_j). \quad (2.52)$$

When they are used to describe a material state, the process history is also taken into account therefore, the internal state variables are calculated by a system of ordinary differential equations (ODEs) also referred to as evolution equations [48, 71]

$$\dot{\boldsymbol{Q}}_i(t) = g_i(\boldsymbol{\varepsilon}(t), T(t), \boldsymbol{Q}_i(t), q_j(t)) \quad \forall i \in \{1, 2, \dots, m\}, \quad (2.53)$$

$$\dot{q}_j(t) = h_j(\boldsymbol{\varepsilon}(t), T(t), \boldsymbol{Q}_i(t), q_j(t)) \quad \forall j \in \{1, 2, \dots, n\}, \quad (2.54)$$

with respect to the influence of the temperature  $T(t)$ . The evolution equation for the inelastic strain tensor is formulated in the same manner

$$\dot{\boldsymbol{\varepsilon}}^{\text{in}}(t) = \mathcal{E}(\boldsymbol{\varepsilon}(t), T(t), \boldsymbol{Q}_i(t), q_j(t)) \quad (2.55)$$

and needed to fully describe the constitutive law of the mixture which is obtained by getting the expressions for the deviatoric stresses from Eq. (2.43) and inserting them into Eq. (2.51)

$$\boldsymbol{\varepsilon} = \frac{\sigma_{\text{mean}}}{3K} \boldsymbol{I} + \frac{\boldsymbol{\sigma}'}{2G} + \boldsymbol{\varepsilon}^{\text{in}} \quad (2.56)$$

with the inelastic strain of the mixture

$$\boldsymbol{\varepsilon}^{\text{in}} = (1 - \eta_h) \boldsymbol{\varepsilon}_s^{\text{in}} + \eta_h \boldsymbol{\varepsilon}_h^{\text{in}}. \quad (2.57)$$

## 2 Theoretical Background

Now the focus of this section is to derive the evolution equation for the inelastic strain. One can express it through the potential  $\Psi$  [120]

$$\dot{\epsilon}^{\text{in}} = \frac{\partial \Psi(\boldsymbol{\sigma})}{\partial \boldsymbol{\sigma}}, \quad (2.58)$$

which itself is a function of the three invariants  $J_1(\boldsymbol{\sigma})$ ,  $J_2(\boldsymbol{\sigma})$ , and  $J_3(\boldsymbol{\sigma})$  of the stress tensor for isotropic inelasticity [111]

$$\Psi(\boldsymbol{\sigma}) = \Psi(J_1(\boldsymbol{\sigma}), J_2(\boldsymbol{\sigma}), J_3(\boldsymbol{\sigma})). \quad (2.59)$$

Their definitions are shown in Eqs. (2.60) - (2.62)

$$J_1(\boldsymbol{\sigma}) = \text{tr}(\boldsymbol{\sigma}), \quad (2.60)$$

$$J_2(\boldsymbol{\sigma}) = \frac{1}{2} \{ [\text{tr}(\boldsymbol{\sigma})]^2 - \text{tr}(\boldsymbol{\sigma}^2) \}, \quad (2.61)$$

$$J_3(\boldsymbol{\sigma}) = \det(\boldsymbol{\sigma}). \quad (2.62)$$

Since the inelastic deformation does not result in a noteworthy change in volume as already discussed in Subsect. 2.3.1,

$$\text{tr}(\dot{\epsilon}^{\text{in}}) = 0 \quad \text{so that} \quad (\dot{\epsilon}^{\text{in}})' = \dot{\epsilon}^{\text{in}} \quad (2.63)$$

only the deviatoric part of the inelastic strain rate tensor needs to be considered. Therefore, the potential  $\Psi$  does not depend on the first invariant of the stress tensor anymore and the influence of the third invariant is often neglected [111]. Rewriting Eq. (2.59) yields the VON MISES potential

$$\dot{\epsilon}^{\text{in}} = \frac{\partial \Psi(J_2(\boldsymbol{\sigma}'))}{\partial \boldsymbol{\sigma}'} \quad (2.64)$$

with the evolution equation for the inelastic strain with respect to the two phases

$$\dot{\epsilon}_p^{\text{in}} = \frac{3}{2} \dot{\epsilon}_{\text{vM}_p}^{\text{in}} \frac{\boldsymbol{\sigma}'_p}{\sigma_{\text{vM}_p}}, \quad (2.65)$$

where  $\sigma_{\text{vM}_p}$  depicts the VON MISES stress and  $\dot{\epsilon}_{\text{vM}_p}^{\text{in}}$  the inelastic VON MISES strain rate with  $p \in \{h, s\}$  accounting for the soft and hard phase

$$\sigma_{\text{vM}_p} = \sqrt{\frac{3}{2} \boldsymbol{\sigma}'_p : \boldsymbol{\sigma}'_p}, \quad \dot{\epsilon}_{\text{vM}_p}^{\text{in}} = \sqrt{\frac{2}{3} \dot{\epsilon}_p^{\text{in}} : \dot{\epsilon}_p^{\text{in}}}. \quad (2.66)$$

Evaluating Eqs. (2.65) and (2.66) with respect to the soft and hard phases results in

$$\dot{\epsilon}_s^{\text{in}} = \frac{3}{2} \dot{\epsilon}_{\text{vM}_s}^{\text{in}} \frac{\boldsymbol{\sigma}'_s}{\sigma_{\text{vM}_s}}, \quad \dot{\epsilon}^{\text{in}} = \frac{3}{2} \dot{\epsilon}_{\text{vM}}^{\text{in}} \frac{\boldsymbol{\sigma}'_h - \boldsymbol{\sigma}'}{\sigma_{\text{vM}_*}}, \quad (2.67)$$

$$\sigma_{\text{vM}_s} = \sqrt{\frac{3}{2} \boldsymbol{\sigma}'_s : \boldsymbol{\sigma}'_s}, \quad \sigma_{\text{vM}_*} = \sqrt{\frac{3}{2} (\boldsymbol{\sigma}'_{h*} - \boldsymbol{\sigma}') : (\boldsymbol{\sigma}'_{h*} - \boldsymbol{\sigma}')}, \quad (2.68)$$

## 2 Theoretical Background

$$\dot{\epsilon}_{vM_s}^{in} = \sqrt{\frac{2}{3} \dot{\epsilon}_s^{in} : \dot{\epsilon}_s^{in}}, \quad \dot{\epsilon}_{vM}^{in} = \sqrt{\frac{2}{3} \dot{\epsilon}^{in} : \dot{\epsilon}^{in}} \quad (2.69)$$

with  $\dot{\epsilon}_{vM}^{in}$  the VON MISES inelastic strain rate for the mixture,  $\sigma_{vM*}$  the VON MISES saturation stress and  $\sigma'_{h*}$  the saturation stress deviator [48, 111, 113].

It is important to note that the inelastic strain rate is not only depending on the stress but also the temperature, so the mathematical description needs to capture both influences. Therefore, a product of two functions is suggested in literature

$$\dot{\epsilon}_{vM}^{in} = f_\sigma(\sigma_{vM}) f_T(T). \quad (2.70)$$

Different expressions for either of them can also be found in [32, 48, 78, 111]. The thesis at hand considers two internal variables: a scalar one  $\Gamma$  for the isotropic hardening and a tensorial one to account for kinematic hardening. In the case of the latter, we use a tensorial description where the stress deviator  $\sigma'$  can be separated into an active and a backstress part, defined by  $\tilde{\sigma}$  and  $\beta$  respectively

$$\sigma' = \tilde{\sigma} + \beta, \quad (2.71)$$

so that

$$\tilde{\sigma} = \sigma' - \beta. \quad (2.72)$$

Two evolution equations have to be defined as mentioned in Eq. (2.52). Based on the description of linear strain hardening and further developed to omit an infinite increase of the hardening, Eq. (2.73) was introduced in [19, 111]

$$\dot{\Gamma} = C(\Gamma_* - \Gamma) \dot{\epsilon}_{vM}^{in}, \quad (2.73)$$

where  $\Gamma_*$  represents a saturation value for steady state applications and  $C$  defines a material parameter determined by fitting the curve to experimental data. In order to account for the backstress, PRAGER made use of a linear equation including another material parameter  $C_1$  and suggesting a collinear dependence of the backstress on the inelastic strain [32, 130]

$$\dot{\beta} = C_1 \dot{\epsilon}^{in}, \quad (2.74)$$

which could not found to be physically motivated. In literature, cf. Subsect. 1.1.2, the ARMSTRONG- FREDERICK model is widely applied where a different evolution equation is formulated [56]

$$\dot{\beta} = C_2 \dot{\epsilon}^{in} - C_3 \dot{\epsilon}_{vM}^{in} \beta. \quad (2.75)$$

Later, CHABOCHE introduces the modelling of several backstresses where each of them has its own evolution equation with the intention to further improve simulation results, especially for cyclic loading cases [30]

$$\beta = \sum_{i=1}^r \beta_i \quad \text{with} \quad \dot{\beta}_i = C_{4_i} \dot{\epsilon}^{in} - C_{5_i} \dot{\epsilon}_{vM}^{in} \beta_i. \quad (2.76)$$

A major drawback of using this approach lies in getting all the different material parameter needed through numerous experiments. Since the resources are limited, the procedure is usually not carried out practically [84].

### 2.3.3 Initial Boundary Value Problem

This part is used as a summary to give a brief overview of the equations introduced in the previous sections. The equations below form the basis of the numerical implementation further explained in Chapt. 3. As usual, the mechanical initial boundary value problem (IBVP) consists of both, balance laws and constitutive equations as follows

- the conservation of mass  

$$dm = \rho dV = \rho_0 dV_0,$$
- the balance of linear momentum  

$$\nabla \cdot \boldsymbol{\sigma} + \rho \mathbf{k} = \rho \dot{\mathbf{v}},$$
- the balance of angular momentum  

$$\boldsymbol{\sigma} = \boldsymbol{\sigma}^T,$$
- the kinematic equation  

$$\boldsymbol{\varepsilon} = \frac{1}{2} [\nabla \mathbf{u} + (\nabla \mathbf{u})^T],$$
- the additive split of strains  

$$\boldsymbol{\varepsilon} = \boldsymbol{\varepsilon}^{\text{el}} + \boldsymbol{\varepsilon}^{\text{in}},$$
- HOOKE's law for linear isotropic elasticity  

$$\boldsymbol{\sigma} = K \operatorname{tr}(\boldsymbol{\varepsilon}^{\text{el}}) \mathbf{I} + 2G\boldsymbol{\varepsilon}^{\text{el}},$$
- an evolution equation to determine the inelastic strain tensor  $\dot{\boldsymbol{\varepsilon}}^{\text{in}}(t)$
- and evolution equations to account for the internal variables.

In the equations above,  $\nabla \cdot$  and  $\nabla$  depict the divergence and gradient operator. For any numerical implementation it is crucial to define the ICs. For all the cases considered in the thesis at hand, the following ICs hold

$$\boldsymbol{\varepsilon}^{\text{in}}(t = 0) = \mathbf{0}, \quad \beta(t = 0) = 0, \quad \Gamma(t = 0) = 1. \quad (2.77)$$

## 2.4 Methods of Time Integration

Time integration methods are a fundamental aspect of numerical analysis, particularly in the context of solving time-dependent differential equations. These methods are crucial in a wide range of scientific and engineering disciplines, where they are employed to simulate the behavior

of engineering and physical applications with respect to time. This section provides a brief overview of the different methods to serve as basis for the numerical implementations of Chapt. 3. In [17, 64, 79, 94, 111], further information on time integration methods can be found.

The study of time integration techniques has evolved significantly over the decades, driven by the need for accurate and stable methods to solve increasingly complex problems. The initial exploration of time integration methods can be linked to the work of early mathematicians like Carl Runge and Wilhelm Kutta, whose development of the RUNGE-KUTTA methods in the early 1900s laid the groundwork for modern numerical analysis [29]. These early methods provided a foundation for the systematic study of numerical solutions to differential equations, focusing on achieving higher accuracy and stability.

During the mid-20th century, researchers began to explore a variety of methods tailored to different types of differential equations, including both ordinary and partial differential equations. The ADAMS-BASHFORTH and ADAMS-MOULTON methods, developed in the 1950s and 1960s, exemplify this period of innovation, offering multi-step approaches that leveraged past information to enhance accuracy [65, 100]. These methods quickly gained importance in applications such as celestial mechanics, where long-term integration was necessary to accurately model the motion of planetary bodies over extended periods [29]. In the field of fluid dynamics, the application of time integration methods has been particularly impactful. The development of numerical techniques to solve the NAVIER-STOKES equations, which govern fluid flow, has relied heavily on both explicit and implicit time integration methods [7]. The stability and accuracy of these methods are critical in capturing the complex, often turbulent behavior of fluids. For instance, the development of the CRANK-NICOLSON method in the 1940s provided a valuable tool for solving PDEs in fluid dynamics with improved stability characteristics [100].

Time integration methods have been crucial in the development of weather prediction and climate models. These models often involve the integration of complex systems of PDEs over long periods, necessitating the use of stable and efficient numerical techniques [28, 65]. Methods like the semi-implicit scheme, which combines aspects of both explicit and implicit methods, have been particularly effective in this field, allowing for larger time steps without sacrificing stability [100]. Similarly, time integration methods are employed in aerospace engineering as referred to in [80] as well as in structural mechanics to analyze the response of structures under time-dependent loads, which is the focus of this thesis.

The key idea behind time integration methods is to discretize the considered time interval  $[t_0, t_k]$  into small increments  $\Delta t = t_{n+1} - t_n$ , where  $n = 0, 1, \dots, k$ , with corresponding discrete time points  $t_k$ , allowing the continuous evolution of a system to be approximated by a series of discrete steps.

Given an ODE of the form

$$\frac{dy}{dt} = \dot{y} = f(t, y) \tag{2.78}$$

or

$$\frac{dY}{dt} = \dot{Y} = f(t, Y) \tag{2.79}$$

with respect to tensorial variables, time integration methods seek to compute the value of  $y(t)$  at successive time points based on known initial conditions and the function  $f(t, y)$ . The accuracy, stability, and computational efficiency of the solution depend heavily on the choice of the time

integration method. Time integration methods can be categorized into two main types: explicit and implicit methods.

### 2.4.1 Explicit Time Integration Methods

Explicit methods are widely used in numerical analysis for solving ODEs due to their simplicity and computational efficiency. They compute the solution at the next time step  $t_{n+1}$  directly from the known values at the current time step  $t_n$  [160]. Typically, explicit methods approximate the solution of the in Eq. (2.78) as:

$$y_{n+1} = y_n + \Delta t f(t_n, y_n), \quad (2.80)$$

where  $\Delta t$  is the time step, and  $y_n$  is the solution at the  $n$ -th time step. In Fig. 2.5, the calculation method to approximate the blue curve is shown graphically.

One of the most fundamental explicit methods is the EULER forward method, which approximates the solution of an ODE by taking small steps forward in time using the current derivative to estimate the future value. Despite its simplicity, the EULER forward method can suffer from stability issues, especially when dealing with stiff equations, which often necessitates smaller time steps to maintain accuracy and stability resulting in longer computational times [27, 67].

In addition to EULER forward, the RUNGE-KUTTA methods provide a more sophisticated approach by evaluating the derivative at multiple points within each time step, improving accuracy without significantly increasing computational cost. The classical fourth-order RUNGE-KUTTA method is particularly popular due to its balance between accuracy and computational

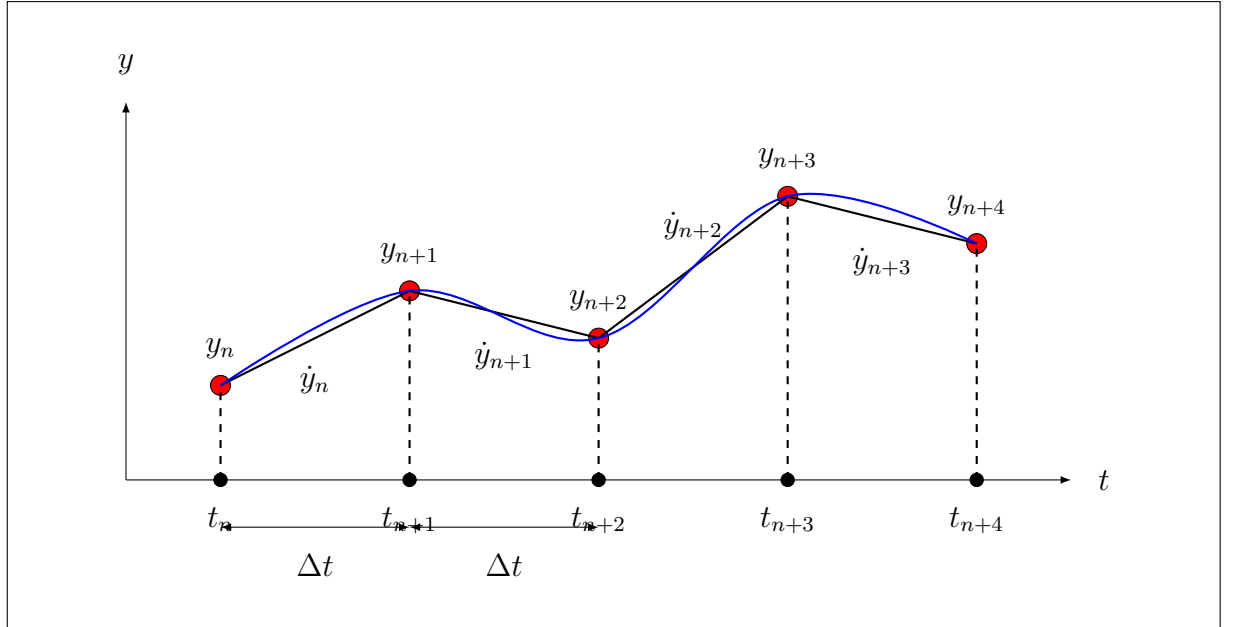


Figure 2.5: Schematic diagram for an explicit time integration procedure

effort [29]. The method using the four points  $p_1 - p_4$  in one time step can be described by

$$\begin{aligned}
 p_1 &= \Delta t f(t_n, y_n), \\
 p_2 &= \Delta t f\left(t_n + \frac{h}{2}, y_n + \frac{p_1}{2}\right), \\
 p_3 &= \Delta t f\left(t_n + \frac{h}{2}, y_n + \frac{p_2}{2}\right), \\
 p_4 &= \Delta t f(t_n + h, y_n + p_3), \\
 y_{n+1} &= y_n + \frac{1}{6}(p_1 + 2p_2 + 2p_3 + p_4).
 \end{aligned} \tag{2.81}$$

Another example is the ADAMS-BASHFORTH method, which is a multi-step approach that uses information from several previous time steps to predict the future state. This method is particularly efficient for problems where the computational cost of evaluating derivatives is high, though it requires the storage of previous solution values [67, 79]. The second order ADAMS-BASHFORTH method including the previous  $n - 1$  and current time step  $n$  can be written as

$$y_{n+1} = y_n + \frac{\Delta t}{2} (3f(t_n, y_n) - f(t_{n-1}, y_{n-1})) \tag{2.82}$$

or in terms of tensorial variables as

$$\mathbf{Y}_{n+1} = \mathbf{Y}_n + \frac{\Delta t}{2} (3f(t_n, \mathbf{Y}_n) - f(t_{n-1}, \mathbf{Y}_{n-1})). \tag{2.83}$$

The general form for the  $k$ -th order with the corresponding coefficients  $h_i$  is expressed through

$$y_{n+1} = y_n + \Delta t \sum_{i=0}^{k-1} h_i f(t_{n-i}, y_{n-i}). \tag{2.84}$$

Here, the coefficients  $h_i$  represent the method-specific weights for each previous function evaluation. These explicit methods are typically straightforward to implement and computationally inexpensive, making them popular for many applications [111]. However, their stability highly depends on the chosen time step size [29, 100, 102] so that a critical time step size has to be mathematically determined [39].

### 2.4.2 Implicit Time Integration Methods

Unlike explicit methods, which determine the future state of a system directly based on its current state, implicit methods require solving equations that involve both the current state at time step  $n$  and the unknown future state at time step  $n + 1$ . As a result, each time step involves solving a system of nonlinear equations [160]. This implicit formulation typically offers unconditional stability, enabling the use of larger time steps without sacrificing the accuracy or stability of the solution.

In the case of an implicit scheme, Eq. (2.78) is solved in the following way

$$y_{n+1} = y_n + \Delta t f(t_{n+1}, y_{n+1}). \tag{2.85}$$

## 2 Theoretical Background

This equation is implicit because  $y_{n+1}$  appears on both sides. Figure 2.6 illustrates the differences in the corresponding program flow charts for the two methods.

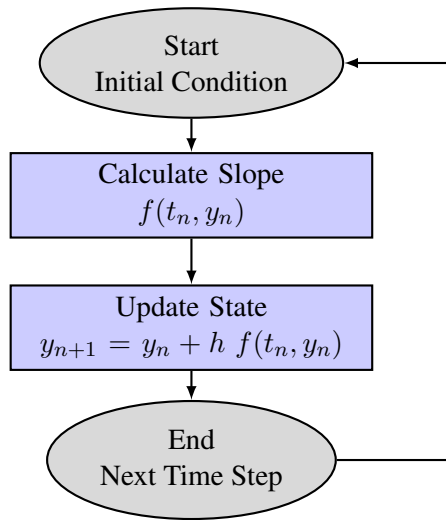
A well-known example is the backward EULER method which is often preferred for stiff problems. The computational costs usually increase due to the need to solve nonlinear equations, using e.g. the NEWTON-RAPHSON method at each step [7, 65, 67].

Another widely used implicit method is the trapezoidal rule, also known as the CRANK-NICOLSON method when applied to parabolic partial differential equations. This method is second-order accurate and combines the implicit stability with the midpoint evaluation of the derivative, offering a good balance between accuracy and stability [7, 79]. It can be expressed through

$$y_{n+1} = y_n + \frac{\Delta t}{2} (f(t_n, y_n) + f(t_{n+1}, y_{n+1})). \quad (2.86)$$

Additionally, the family of implicit RUNGE-KUTTA methods, such as the GAUSS-LEGENDRE methods, are valuable for their high-order accuracy and stability, though they require solving

### Explicit Integration Scheme



### Implicit Integration Scheme

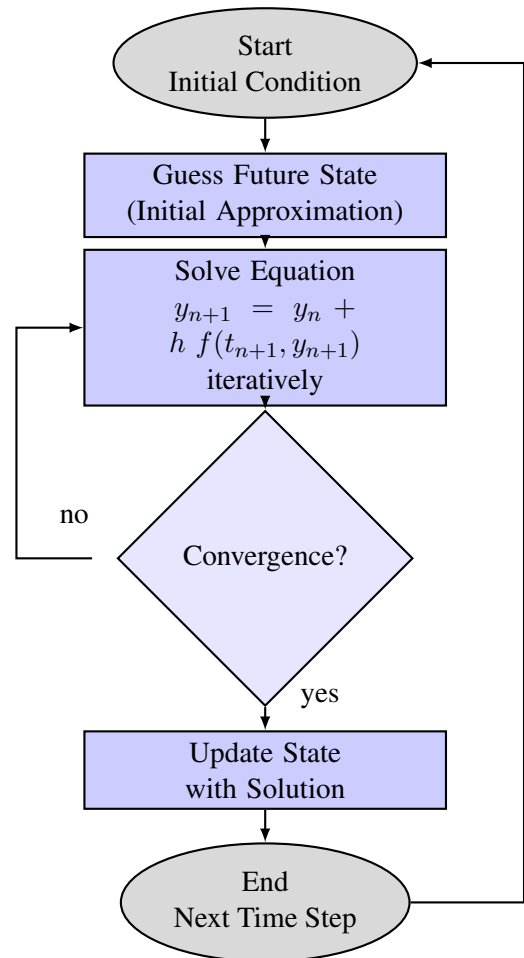


Figure 2.6: Comparison between the general program flowcharts of explicit and implicit time integration methods



multiple nonlinear equations per time step, which increases computational cost [68]. The two-stage GAUSS-LEGENDRE method is written as

$$y_{n+1} = y_n + \Delta t \sum_{i=1}^s b_i k_i, \quad (2.87)$$

$$k_i = f \left( t_n + c_i \Delta t, y_n + \Delta t \sum_{j=1}^s a_{ij} k_j \right), \quad i = 1, 2, \dots, s,$$

where  $s$  is the number of stages, and the coefficients  $a_{ij}$ ,  $b_i$ , and  $c_i$  are determined by the specific method [68].

## 2.5 Two-Time-Scale Approach

This section introduces the multi-timescaling procedure and the numerical techniques needed to implement a material model using this approach. The overall goal is to simulate a large number of cycles predicting the long-term response while reducing the computational cost significantly. The theory was initially proposed in [66], for elasto-viscoplastic homogeneous solids cf. Subsect. 1.1.3. It was inspired by and hence follows a similar calculation procedure as the widely known spatial homogenization [69, 70].

The two-time-scale approach is based on the introduction of two different time scales, as shown in Fig. 2.7. The first is denoted as  $t_M$  representing the slow or macro time scale associated with quasi-static loading, while  $\tau$  as the fast or micro time scale is used to capture the effects of rapidly varying oscillations characterized by the period  $P$  [4, 70, 84].

Considering a system of ordinary differential equations

$$\frac{d\mathbf{x}}{dt} = \mathbf{X}[t, \mathbf{x}(t)], \quad \mathbf{x}(t=0) = \mathbf{x}_0 \quad (2.88)$$

with

$$\mathbf{x} = (x_1, x_2, \dots, x_e)^T, \quad \mathbf{X} = (X_1, X_2, \dots, X_e)^T \quad (2.89)$$

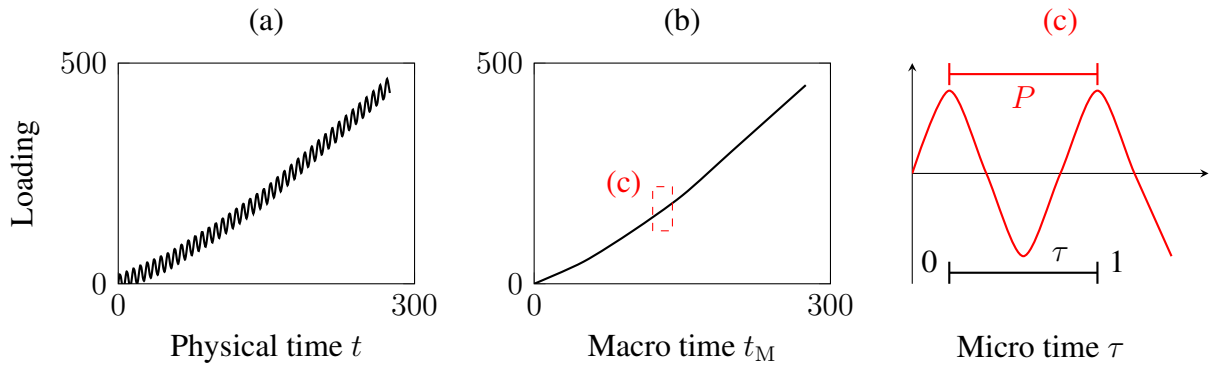


Figure 2.7: Basic principle of the two-time-scale approach by dividing the physical time  $t$  shown in (a) into the two time scales: the macro scale  $t_M$  illustrated in part (b) and the micro time  $\tau$  depicted in (c) after [69]

## 2 Theoretical Background

includes  $\mathbf{x}$  as a set of unknown variables such as the components of the inelastic strain or back-stress tensor and  $\mathbf{X}$ , continuous functions of time and  $\mathbf{x}$ . Now the solution  $\mathbf{x}(t)$  can be represented in dependence of the two time scales

$$\mathcal{T}_1(t) = t_M, \quad \mathcal{T}_2(t) = \tau(t), \quad (2.90)$$

so that

$$\mathbf{x}(t) = \mathbf{x}(\mathcal{T}_1(t), \mathcal{T}_2(t)) \quad (2.91)$$

and each point of the physical time  $t$  may be expressed as

$$t = t_M + P\tau. \quad (2.92)$$

The connection of the scales is pictured in Fig. 2.8. Both of the time scales are depending on one another which is expressed through a scaling parameter  $\mu$  with respect to the total time  $t_{\text{end}}$

$$\mu = \frac{P}{t_{\text{end}}} \ll 1. \quad (2.93)$$

The time interval  $[0, t_{\text{end}}]$  should be considered such that  $T \ll t_{\text{end}}$  is valid. The total time derivative with respect to the two time scales due to the chain rule yields

$$\frac{d}{dt} = \frac{\partial}{\partial t_M} + \frac{1}{\mu} \frac{\partial}{\partial \tau}. \quad (2.94)$$

Including the variable of interest results in

$$\frac{d\mathbf{x}}{dt} = \dot{\mathbf{x}} = \frac{\partial \mathbf{x}}{\partial t_M} + \frac{1}{\mu} \frac{\partial \mathbf{x}}{\partial \tau} = \mathbf{X}(t_M, \tau, \mathbf{x}) \quad (2.95)$$

where the superposed dot denotes the total time derivative with respect to the physical time  $t$ . Instead of ODEs as in Eq. (2.88), now a system of PDEs is obtained [4, 83, 84]. In the next step, in order to find the approximate solution of the PDEs, an asymptotic series expansion is applied

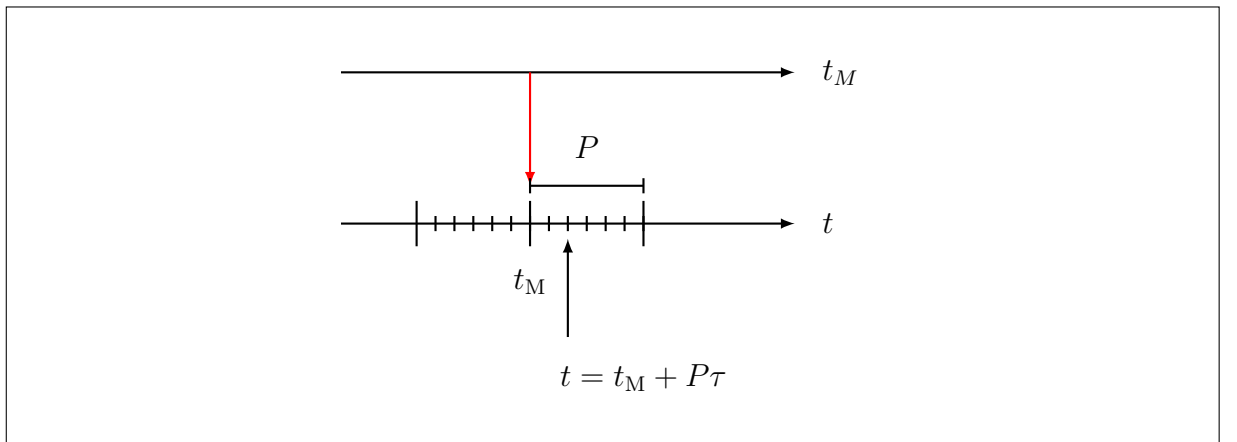


Figure 2.8: Schematic decomposition of the physical time  $t$  after [69]

## 2 Theoretical Background

with respect to the factor  $\mu$

$$\mathbf{x}(t_M, \tau) = \mathbf{x}^{(0)}(t_M, \tau) + \mu \mathbf{x}^{(1)}(t_M, \tau) + \mu^2 \mathbf{x}^{(2)}(t_M, \tau) + \dots \quad (2.96)$$

$$\mathbf{x}(t_M, \tau) = \mathbf{x}^{(0)}(t_M, \tau) + \mu \mathbf{x}^{(1)}(t_M, \tau) + O(\mu^2) \quad (2.97)$$

including  $O(\mu^2)$ , the BACHMANN-LANDAU notation (or asymptotic notation) [10, 95]. Inserting Eq. (2.97) into Eq. (2.94) results in

$$\dot{\mathbf{x}} = \left( \frac{\partial \mathbf{x}^{(0)}}{\partial t_M} + \frac{1}{\mu} \frac{\partial \mathbf{x}^{(0)}}{\partial \tau} \right) + \mu \left( \frac{\partial \mathbf{x}^{(1)}}{\partial t_M} + \frac{1}{\mu} \frac{\partial \mathbf{x}^{(1)}}{\partial \tau} \right) + \dots \quad (2.98)$$

and sorted according to the orders of  $\mu$

$$\dot{\mathbf{x}} = \frac{1}{\mu} \frac{\partial \mathbf{x}^{(0)}}{\partial \tau} + \left( \frac{\partial \mathbf{x}^{(0)}}{\partial t_M} + \frac{\partial \mathbf{x}^{(1)}}{\partial \tau} \right) + \mu \left( \frac{\partial \mathbf{x}^{(1)}}{\partial t_M} + \frac{1}{\mu} \frac{\partial \mathbf{x}^{(2)}}{\partial \tau} \right) + \dots \quad (2.99)$$

Also expanding the left-hand side of Eq. (2.99) in the form

$$\begin{aligned} \mathbf{X}(t_M, \tau, \mathbf{x}) &= \mathbf{X}(t_M, \tau, \mathbf{x}^{(0)} + \mu \mathbf{x}^{(1)} + \dots) \\ &= \mathbf{X}(t_M, \tau, \mathbf{x}^{(0)}) + \mu \frac{\partial \mathbf{X}}{\partial \mathbf{x}}(t_M, \tau, \mathbf{x}^{(0)}) \mathbf{x}^{(1)} + \dots \end{aligned} \quad (2.100)$$

and equating terms of the same orders of  $\mu$  yields the first part of the  $\mu^{(-1)}$ -order problem

$$\frac{\partial \mathbf{x}^{(0)}}{\partial \tau} = 0. \quad (2.101)$$

Following the same procedure for the increasing orders of the scaling factor, the result is a set of differential equations sorted with respect to the order of  $\mu$

$$\begin{aligned} \mu^{(-1)} : \quad & \frac{\partial \mathbf{x}^{(0)}}{\partial \tau} = 0, \\ \mu^{(0)} : \quad & \frac{\partial \mathbf{x}^{(0)}}{\partial t_M} + \frac{\partial \mathbf{x}^{(1)}}{\partial \tau} = \mathbf{X}(t_M, \tau, \mathbf{x}^{(0)}), \\ \mu^{(1)} : \quad & \frac{\partial \mathbf{x}^{(1)}}{\partial t_M} + \frac{\partial \mathbf{x}^{(2)}}{\partial \tau} = \frac{\partial \mathbf{X}(t_M, \tau, \mathbf{x}^{(0)})}{\partial \mathbf{x}} \mathbf{x}^{(1)}. \end{aligned} \quad (2.102)$$

As a result of Eq. (2.102), the zero order solution  $\mathbf{x}^{(0)}$  is only a function of the slow time  $t_M$ . According to [140], a time averaging operator  $\mathcal{M}$  is introduced

$$\mathcal{M} = \langle f(t_M, \tau) \rangle = \lim_{\mathcal{T} \rightarrow \infty} \frac{1}{\mathcal{T}} \int_0^{\mathcal{T}} f(t_M, \tau) d\tau \quad (2.103)$$

where we assume the existing time average of a vector function to be

$$\langle \mathbf{X}(t_M, \mathbf{x}^{(0)}) \rangle = \mathcal{M}(\mathbf{X}(t_M, \tau, \mathbf{x}^{(0)})) \quad (2.104)$$

so that

$$\mathcal{M} \left( \frac{\partial \mathbf{x}^{(1)}}{\partial \tau} \right) = \lim_{\tau \rightarrow \infty} \frac{1}{\tau} (\mathbf{x}^{(1)}(t_M, \tau) - \mathbf{x}^{(1)}(t_M, 0)) = 0. \quad (2.105)$$

The general decomposition of the variables into a mean and oscillatory part is suggested as follows

$$\mathbf{x}(t_M, \tau) = \mathbf{x}_M(t_M) + \mathbf{x}_m(t_M, \tau). \quad (2.106)$$

Applying the operator  $\mathcal{M}$  to the zero order  $\mu^{(0)}$  problem results in a system of ODEs

$$\frac{d\mathbf{x}^{(0)}}{dt} = \langle \mathbf{X}(t_M, \mathbf{x}^{(0)}) \rangle. \quad (2.107)$$

Integrating Eq. (2.107) yields the solution of the mean variable  $\mathbf{x}^{(0)}$  which is the goal of the work at hand. The solutions of higher orders can be found in [18, 119, 140]. Assuming  $P$ -periodicity, the average value with respect to the fast time scale at a certain macro time is given to be

$$\langle \mathbf{x}(t_M, \tau) \rangle = \frac{1}{P} \int_0^P \mathbf{x}(t_M, \tau) d\tau = \int_0^1 \mathbf{x}(t_M, \xi) d\xi, \quad \xi = \frac{\tau}{P} \quad (2.108)$$

with  $\langle \square \rangle$  marking the variable after the application of the averaging operator [4, 70]. The goal is to ensure the stability of the multiscale method so that the fast scale solution is part of the slow scale problem in terms of the average [2, 58, 157].

Such a form of averaging in terms of a definite integral can be calculated using different numerical methods, in [69], the quadrature rule was suggested. It is a numerical technique used to approximate definite integrals which relies on weighted sums of function values at specific points within the integration domain. One of the simplest quadrature rules is the midpoint rule, where the integral of a function  $f(x)$  over an interval  $[a, b]$  is calculated as

$$\int_a^b f(x) dx \approx (b - a) f\left(\frac{a + b}{2}\right). \quad (2.109)$$

Quadrature methods, including GAUSSIAN quadrature, are widely used in scientific computing and engineering applications, such as in the FEM for solving PDEs [164]. The choice of quadrature rule often depends on the problem at hand and the desired accuracy [42].

Trapezoidal averaging, also known as the trapezoidal rule, is a numerical integration technique that approximates the area under a curve by dividing the interval into smaller trapezoids rather than rectangles. It offers a more accurate estimation compared to simple rectangular methods, shown in Fig. 2.9. The trapezoidal rule estimates the finite integral of a function  $f(x)$  over an interval  $[a, b]$  by dividing it into subintervals. For each of them, the rule computes the area of a trapezoid with corners at  $(x_j, 0)$ ,  $(x_{j+1}, 0)$ ,  $(x_j, f(x_j))$ , and  $(x_{j+1}, f(x_{j+1}))$ , which is given by

$$\int_a^b f(x) dx \approx \sum_{j=0}^{n-1} \frac{h}{2} (f(x_j) + f(x_{j+1})) \quad \text{with} \quad h = \frac{b - a}{n} \quad (2.110)$$

with the approximation improving as the number of segments increases [33]. This method

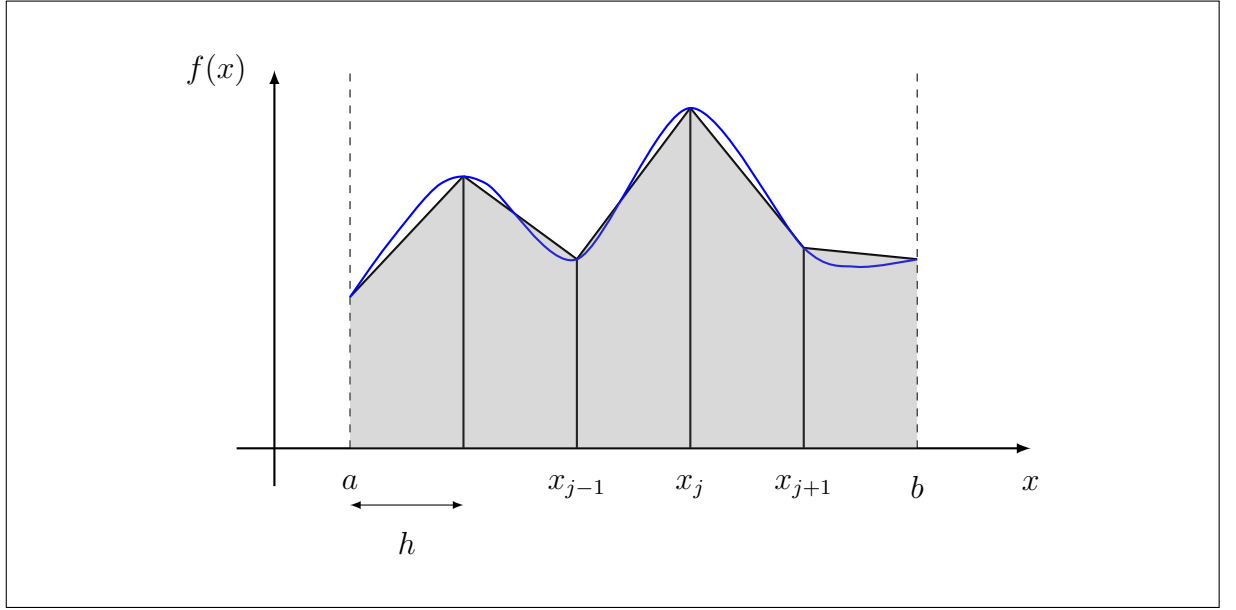


Figure 2.9: Sketch of an approximation to the arbitrary function  $f(x)$  in the interval from  $a$  to  $b$  depicted in blue using the trapezoidal rule with five segments after [33]

has widespread applications in computational science, especially when dealing with discretized data points [26]. It was already applied to solve differential equations in FEM, providing an efficient way to handle integral calculations for structural analysis [164]. For example, in the analysis of beam structures, trapezoidal integration is often used to evaluate internal forces and displacements across elements [12]. Furthermore, the method is also used in transient heat conduction problems, where it helps compute the temperature distribution in materials over time [136]. In the case of multiscale coupling, where systems or processes are studied across different spatial or temporal scales, it was suggested in [53] to compute quantities across varying scales. The simplicity and efficiency of the trapezoidal rule make it well-suited for problems where multiscale coupling requires frequent and fast evaluations of integrals over non-uniform grids, ensuring the computational feasibility of complex simulations [159].

The two-time-scale approach relies on the assumption of periodic or quasi-periodic loading and a clear separation between the macro and micro time scales. Consequently, its applicability is limited in cases with non-periodic loading, sudden transients, or strongly history-dependent material behavior. Additionally, the choice of the scaling parameter  $\mu$  and macro time step must be carefully calibrated to ensure numerical stability and physical accuracy [52, 132].

# 3 Numerical Implementation for X20CrMoV12-1

This chapter focuses on the numerical implementation of the constitutive model developed for the high-temperature steel X20CrMoV12-1. The focus lies on a fully resolved, cycle-by-cycle simulation approach that enables precise modeling of the material behavior under thermomechanical loading conditions. This methodology forms the foundation for the subsequent application of a multiscale modeling strategy, which will be introduced in the following Sect. 3.2. The implementation is carried out in Python using an explicit time integration scheme and is validated through comparison with finite element simulations conducted in ABAQUS. This validation ensures that the model captures both the global and local mechanical responses with sufficient accuracy. For completeness, the second steel under consideration, X12CrMoWVNbN10-1-1, is introduced in Chapt. 4, where the same numerical strategy is extended and adapted accordingly.

## 3.1 Cycle-by-cycle Simulations

The fully resolved problem describes the solution of the constitutive equations using the Python library. The material model was the main object of several studies and articles [55, 48, 59, 62, 138] including computational modeling approaches using continuum damage mechanics models or phase-mixture models. The steel is most commonly used in the construction of boilers, turbine components, pressure vessels, and piping systems in power plant components due to its ability to maintain mechanical strength and resist deformation under long-term exposure to high temperatures [57]. In [48], the same system of equations was solved via the finite element method. The software ABAQUS including a user defined material description (UMAT) was employed. These results will serve as comparison for the validation in Subsects. 3.1.3 and 3.2.3 of this chapter.

### 3.1.1 Constitutive Equations

The model for the high tempered martensitic steel X20CrMoV12-1 was developed in [48, 49, 113, 117, 118] with the aim to analyze power plant components. To derive the equations of the phase-mixture model, Eq. (2.56) and Eq. (2.65) are derived with respect to time and then read

$$\dot{\epsilon} = \frac{d}{dt} \left( \frac{\sigma_{\text{mean}}}{3K} \mathbf{I} + \frac{\boldsymbol{\sigma}'}{2G} \right) + \dot{\epsilon}^{\text{in}}, \quad (3.1)$$

$$\dot{\epsilon}^{\text{in}} = \dot{\epsilon} - \frac{d}{dt} \left( \frac{\sigma_{\text{mean}}}{3K} \mathbf{I} + \frac{\boldsymbol{\sigma}'}{2G} \right). \quad (3.2)$$

This equation describes the total strain rate as the sum of an elastic part, governed by the material stiffness parameters, and an inelastic part, accounting for time-dependent deformation mechanisms. It includes the evolution of the inelastic strain as

$$\dot{\epsilon}_s^{\text{in}} = \frac{3}{2} \frac{\dot{\epsilon}_{\text{vMs}}^{\text{in}}}{\sigma_{\text{vMs}}}, \quad \dot{\epsilon}^{\text{in}} = \frac{3}{2} \frac{\dot{\epsilon}_{\text{vM}}^{\text{in}}}{\sigma_{\text{vM}_*}} (\sigma'_h - \sigma'), \quad (3.3)$$

where the  $\dot{\epsilon}_{\text{vMs}}^{\text{in}}$  describes the VON MISES inelastic strain rate. Now, Eq. (2.69) defining the VON MISES stress yields

$$\dot{\epsilon}_{\text{vMs}}^{\text{in}} = \sqrt{\frac{2}{3} \text{tr} (\dot{\epsilon}_s^{\text{in}})^2}, \quad \dot{\epsilon}_{\text{vM}}^{\text{in}} = \sqrt{\frac{2}{3} \text{tr} (\dot{\epsilon}^{\text{in}})^2}. \quad (3.4)$$

The VON MISES inelastic strain rate with respect to the soft phase consists of a separation ansatz including the stress response function  $f_\sigma$  and a temperature response function  $f_T$

$$\dot{\epsilon}_{\text{vMs}}^{\text{in}} = f_\sigma(\sigma_{\text{vMs}}) f_T(T). \quad (3.5)$$

The internal variables  $\beta$  and  $\Gamma$  are introduced to define the inelastic behavior [113]. They are defined as follows including the VON MISES backstress  $\beta_{\text{vM}}$

$$\beta = \frac{\eta_{h_0}}{1 - \eta_{h_0}} (\sigma'_h - \sigma') \quad \forall \quad 0 < \eta_{h_0} < 1, \quad (3.6)$$

$$\beta_{\text{vM}} = \sqrt{\frac{3}{2} \beta : \beta} \quad \forall \quad 0 \leq \beta_{\text{vM}} \leq \beta_{\text{vM}_*}, \quad (3.7)$$

$$\Gamma = \frac{\eta_h}{1 - \eta_h} \frac{1 - \eta_{h_0}}{\eta_{h_0}} \quad \forall \quad \Gamma_* \leq \Gamma \leq 1, \quad (3.8)$$

with the saturation values

$$\beta_* = \frac{\eta_{h_0}}{1 - \eta_{h_0}} (\sigma'_{h_*} - \sigma'), \quad (3.9)$$

$$\beta_{\text{vM}_*} = \sqrt{\frac{3}{2} \beta_* : \beta_*}, \quad (3.10)$$

$$\Gamma_* = \frac{\eta_{h_*}}{1 - \eta_{h_*}} \frac{1 - \eta_{h_0}}{\eta_{h_0}} \quad \forall \quad 0 < \eta_{h_*} < 1. \quad (3.11)$$

Inserting the equations above into the definitions of the stress deviator with respect to the phases results in

$$\sigma'_h = \sigma' + \frac{1 - \eta_{h_0}}{\eta_{h_0}} \beta, \quad (3.12)$$

$$\sigma'_s = \tilde{\sigma}', \quad (3.13)$$

$$\dot{\epsilon}_h^{\text{in}} = \frac{3}{2} \frac{\dot{\epsilon}_{\text{vM}}^{\text{in}}}{\beta_{\text{vM}_*}} \beta, \quad (3.14)$$

$$\dot{\epsilon}_s^{\text{in}} = \frac{3}{2} f_\sigma(\sigma_{\text{vM}}) f_T(T) \frac{\tilde{\sigma}'}{\tilde{\sigma}_{\text{vM}}}. \quad (3.15)$$

Equation (2.42) still holds to compute the effective stress deviator

$$\tilde{\sigma}' = \sigma' - \Gamma\beta \quad \tilde{\sigma}_{\text{vM}} = \sqrt{\frac{3}{2} \text{tr} (\tilde{\sigma}'^2)}. \quad (3.16)$$

Since Eq. (3.1) is valid for both phases, the soft and the hard constituent, it is now evaluated for the soft phase and inserted into Eq. (3.2). Additionally, the definitions for the stress deviator and strain rate tensor for the soft phase are employed resulting in an evolution equation for the inelastic strain

$$\dot{\epsilon}^{\text{in}} = \frac{3}{2} f_{\sigma}(\tilde{\sigma}_{\text{vM}}) f_T(T) \frac{\tilde{\sigma}'}{\tilde{\sigma}_{\text{vM}}}. \quad (3.17)$$

Repeating the same process with respect to the hard phase results in an evolution equation for the backstress tensor

$$\dot{\beta} = \frac{1}{G(T)} \frac{dG(T)}{dT} \dot{T} \beta + 2G(T) \frac{\eta_{h0}}{1 - \eta_{h0}} \left[ \dot{\epsilon}^{\text{in}} - \frac{3}{2} \frac{\dot{\epsilon}_{\text{vM}}^{\text{in}}}{\beta_{\text{vM}}(\sigma_{\text{vM}})} \beta \right]. \quad (3.18)$$

In the case of  $\Gamma = 1$ , the system results in the FREDERICK-ARMSTRONG-CHABOCHE model with kinematic hardening [32, 56]. The internal variable  $\Gamma$  describes softening processes. For high temperature steels with 9 – 12%Cr, in [48, 113] the following equation is provided

$$\dot{\Gamma} = C_{\Gamma} [\Gamma_{\star}(\sigma_{\text{vM}}) - \Gamma] \dot{\epsilon}_{\text{vM}}^{\text{in}}. \quad (3.19)$$

The phase-mixture model applies the iso-strain concept which, under the assumption of constant volume fractions, can equivalently be represented by a rheological model as illustrated in Fig. 3.1, based on the works of [6, 48]. This model consists of two parallel elastic elements corresponding to the individual phase stiffnesses,  $E_s$  for the soft phase and  $E_h$  for the hard phase, respectively. Each elastic element is coupled with an inelastic element that accounts for phase-specific behavior, represented by the internal strains  $\epsilon_s^{\text{in}}$  and  $\epsilon_h^{\text{in}}$ . The use of such a rheological representation facilitates a modular and physically interpretable formulation of the overall inelastic response of the mixture, allowing separate treatment of the elastic and inelastic contributions from each constituent phase.

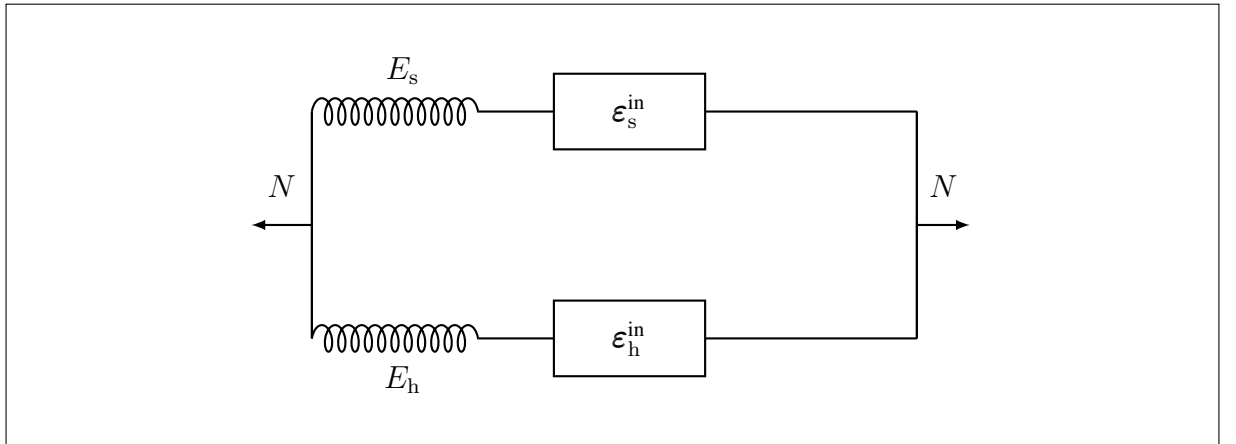


Figure 3.1: Rheological model of the iso-strain concept after [48]



Now, the material model is fully described. In the case of a strain rate controlled process, an evolution equation with respect to the stress tensor  $\sigma$  should be formulated

$$\begin{aligned} \dot{\sigma} = & K(T) \dot{\epsilon}_v \mathbf{I} + 2G(T) (\dot{\epsilon} - \dot{\epsilon}^{\text{in}}) + \left( \frac{dK(T)}{dT} + \frac{2}{3} \frac{dG(T)}{dT} \right) \dot{T} \frac{\sigma_{\text{mean}}}{K(T)} \mathbf{I} \\ & + \frac{1}{G(T)} \frac{dG(T)}{dT} \dot{T} \sigma'. \end{aligned} \quad (3.20)$$

The model was successfully calibrated and proven to be thermodynamically consistent in [48]. A function including three material parameters  $E_1, E_2$  and  $E_3$  was used to determine the YOUNG's modulus with respect to the temperature  $T$

$$E(T) = f_E(T) = E_1 + E_2 \left( \frac{T}{E_3} \right)^3. \quad (3.21)$$

The temperature dependence of the POISSON's ratio  $\nu(T)$  is expressed through

$$\nu(T) = \frac{1}{2} \frac{a_\nu T + b_\nu}{c_\nu T + d_\nu} - 1 \quad (3.22)$$

by four material parameters. The temperature response function to define the inelastic strain rate was based on the well-known ARRHENIUS law so that

$$f_T(T) = \exp \left( -\frac{Q}{RT} \right), \quad (3.23)$$

where  $Q$  describes the activation energy and  $R$  represents the universal gas constant. The stress response function introduces four material parameters,  $a_\sigma, b_\sigma, c_\sigma$  as well as the exponent  $m_\sigma$

$$f_\sigma(\tilde{\sigma}_{\text{vM}}) = a_\sigma \sinh \left( \frac{\tilde{\sigma}_{\text{vM}}}{b_\sigma} \right) \left[ 1 + \left( \frac{\tilde{\sigma}_{\text{vM}}}{c_\sigma} \right)^{m_\sigma} \right]. \quad (3.24)$$

The saturation values depending on the VON MISES stress for the backstress  $\beta_{\text{vM}\star}(\sigma_{\text{vM}})$  and the softening variable  $\Gamma_\star(\sigma_{\text{vM}})$  are defined as

$$\beta_{\text{vM}\star}(\sigma_{\text{vM}}) = \frac{2a_\beta}{1 + \exp(-b_\beta \sigma_{\text{vM}})} - a_\beta, \quad (3.25)$$

$$\Gamma_\star(\sigma_{\text{vM}}) = \frac{a_\Gamma}{1 + \exp[-b_\Gamma(\sigma_{\text{vM}} - c_\Gamma)]}, \quad (3.26)$$

where both of them make use of two more material parameters each,  $a_\beta, b_\beta$  and  $a_\Gamma, b_\Gamma$  respectively. When dealing with three-dimensional loading cases and therefore stress and deformation states, two independent elastic parameters have to be used [6]. To be able to capture the temperature dependence of the shear modulus  $G$ , experimental data found in [149] served as a basis. A cubic polynomial was suggested then

$$G(T) = G_1 + G_2 T^3. \quad (3.27)$$

Finally, all of the above named material parameters are summarized in Table 3.1.

Table 3.1: Parameter values for the X20CrMoV12-1 material model [48]

Variable	Value	Unit	Meaning
$E_1$	$2.23 \times 10^5$	MPa	Parameters in the temperature response function for YOUNG's modulus
$E_2$	$-1.31 \times 10^3$	MPa	
$E_3$	200.0	K	
$a_\nu$	$-9.56 \times 10^{-2}$	$K^{-1}$	Parameters in the temperature response function for POISSON's ratio
$b_\nu$	252.3	-	
$c_\nu$	$-3.88 \times 10^{-2}$	$K^{-1}$	
$d_\nu$	97.4	-	
$G_1$	$-9.56 \times 10^{-2}$	$K^{-1}$	Parameters in the temperature response function for the shear modulus
$G_2$	252.3	-	
$Q$	$540.6 \times 10^3$	$J \text{ mol}^{-1}$	Activation energy in the ARRHENIUS law for the inelastic strain rate
$R$	8.317	$J (\text{mol K})^{-1}$	Universal gas constant the ARRHENIUS law for the inelastic strain rate
$a_\sigma$	$1.54 \times 10^{24}$	$s^{-1}$	Parameters in the stress response function for the inelastic strain rate
$b_\sigma$	25.8	MPa	
$c_\sigma$	483.6	MPa	
$m_\sigma$	35.7	-	
$\eta_{h0}$	0.17	-	Value for the volume fraction of the hard constituent in the beginning
$a_\beta$	80.0	MPa	Parameters of the evolution function for the saturation backstress
$b_\beta$	$2.70 \times 10^{-2}$	$\text{MPa}^{-1}$	
$C$	5.0	-	Parameter in the evolution equation of the softening variable
$a_\Gamma$	1.0	-	Parameters in the stress response function for the saturation softening variable
$b_\Gamma$	$1.30 \times 10^{-2}$	$\text{MPa}^{-1}$	
$c_\Gamma$	520.0	MPa	

### 3.1.2 Implementation

In order to solve such a system of differential equations as described in Subsect. 3.1.1 either as UMAT in the FEM or in a Python code, a time integration procedure has to be applied. The first employs an implicit time integration scheme developed in [48], where also further information on the implementation using the stress update algorithm can be found. Within this work, the focus lies on the implementation via Python which serves as basis for the application of the two-time-scale approach. Here, the ADAMS-BASHFORTH of 5<sup>th</sup> order procedure was used in the Python code, as introduced in Subsect. 2.4.1 to integrate the constitutive equations of X20CrMoV12-1 steel with respect to time.

Switching from an implicit to an explicit integration method can be advantageous when computational efficiency and ease of implementation are priorities especially in large-scale or real-time simulations. Among explicit methods, EULER forward is the simplest, but it suffers from low accuracy and poor stability, especially when larger time steps are desired. While it is possible to apply the EULER forward method in a two-time-scale framework, doing so would require very small time steps to maintain accuracy and stability, negating much of the performance benefit gained from switching to an explicit scheme. The ADAMS-BASHFORTH 5<sup>th</sup>-order method, on the other hand, offers significantly higher accuracy and better stability characteristics. This makes it particularly suitable for integrating the slow dynamics in a two-time-scale approach, where fewer but larger macro-steps are preferred. It also leverages previously computed values, which improves efficiency without sacrificing precision. Therefore, once the transition to an explicit method is made, the ADAMS-BASHFORTH 5<sup>th</sup>-order method is a more effective choice than EULER forward, as it achieves a better balance between accuracy, efficiency, and numerical stability in two-time-scale simulations.

With the aim of solving Eq. (2.79), a time step  $\Delta t$  is prescribed and all the values at time  $t_n$  are considered as known, so the scheme according to ADAMS-BASHFORTH

$$\mathbf{Y}_{n+1} = \mathbf{Y}_n + \Delta t \sum_{i=0}^{k-1} h_i \mathbf{f}(t_{n-i}, \mathbf{Y}_{n-i}) \quad (3.28)$$

with respect to the tensorial variable  $\mathbf{Y}$  can be applied. The incremental contribution of Eq. (3.28) represents the change in a given state variable over the time step

$$\Delta \square_n := \Delta t \sum_{i=0}^{k-1} h_i \mathbf{f}_{\square}(t_{n-i}, \mathbf{Y}_{n-i}), \quad (3.29)$$

which will be summarized as  $\Delta \square_n$  so that based on a known state at time  $t_n$  the total strain  $\boldsymbol{\varepsilon}$ , the inelastic strain  $\boldsymbol{\varepsilon}^{\text{in}}$ , the backstress  $\boldsymbol{\beta}$ , the softening variable  $\Gamma$ , the temperature  $T$  and the stress  $\boldsymbol{\sigma}$  at  $t_{n+1}$  are computed using

$$\boldsymbol{\varepsilon}_{n+1} = \boldsymbol{\varepsilon}_n + \Delta \boldsymbol{\varepsilon}_n, \quad (3.30)$$

$$\boldsymbol{\varepsilon}_{n+1}^{\text{in}} = \boldsymbol{\varepsilon}_n^{\text{in}} + \Delta \boldsymbol{\varepsilon}_n^{\text{in}}, \quad (3.31)$$

$$\boldsymbol{\beta}_{n+1} = \boldsymbol{\beta}_n + \Delta \boldsymbol{\beta}_n, \quad (3.32)$$

$$\Gamma_{n+1} = \Gamma_n + \Delta \Gamma_n, \quad (3.33)$$

$$T_{n+1} = T_n + \Delta T_n, \quad (3.34)$$

$$\boldsymbol{\sigma}_{n+1} = \boldsymbol{\sigma}_n + \Delta \boldsymbol{\sigma}_n. \quad (3.35)$$

Accordingly, each state variable is incremented by evaluating its corresponding evolution equation, e.g.

$$\Delta \boldsymbol{\epsilon}_n^{\text{in}} = \Delta t \sum_{i=0}^{k-1} h_i \dot{\boldsymbol{\epsilon}}^{\text{in}}(t_{n-i}, \boldsymbol{\epsilon}_{n-i}^{\text{in}}), \quad (3.36)$$

$$\Delta \boldsymbol{\beta}_n = \Delta t \sum_{i=0}^{k-1} h_i \dot{\boldsymbol{\beta}}(t_{n-i}, \boldsymbol{\beta}_{n-i}), \quad (3.37)$$

$$\Delta \Gamma_n = \Delta t \sum_{i=0}^{k-1} h_i \dot{\Gamma}(t_{n-i}, \Gamma_{n-i}), \quad (3.38)$$

$$\Delta \boldsymbol{\sigma}_n = \Delta t \sum_{i=0}^{k-1} h_i \dot{\boldsymbol{\sigma}}(t_{n-i}, \boldsymbol{\sigma}_{n-i}). \quad (3.39)$$

These componentwise updates are applied after evaluating the multistep formula (3.28), allowing the full state at time  $t_{n+1}$  to be constructed based on the known history. Hence, the definition of the increments in the Python code is done directly through the evaluation of the differential equations, where in the UMAT, a time discrete form of the evolution equations was needed.

The initial conditions are defined as

$$\boldsymbol{\epsilon}^{\text{in}}(t=0) = \mathbf{0}, \quad \boldsymbol{\beta}(t=0) = \mathbf{0}, \quad \Gamma(t=0) = 1, \quad \boldsymbol{\sigma}(t=0) = \mathbf{0}. \quad (3.40)$$

The procedure is summarized in Algorithm 1.

In order to include the two-time-scale approach, a differential equation with respect to the variable of interest, in this case the stress, is also needed. Therefore, the time derivative of the three dimensional elastic law is already employed to calculate the material's response in the fully resolved problem the following way

$$\dot{\boldsymbol{\sigma}} = \dot{\lambda} \text{tr}(\boldsymbol{\epsilon}) \mathbf{I} + \lambda \text{tr}(\dot{\boldsymbol{\epsilon}}) \mathbf{I} + 2\dot{\mu} \boldsymbol{\epsilon} + 2\mu \dot{\boldsymbol{\epsilon}} \quad (3.41)$$

with the time dependent LAMÉ parameters  $\lambda$  and  $\mu$ .

---

**Algorithm 1** ADAMS-BASHFORTH 5<sup>th</sup>-Order Time Integration

---

**1. Initialize:**

- Set all state variables at  $t = 0$ :

$$\epsilon^{\text{in}}(0) = \mathbf{0}, \quad \beta(0) = \mathbf{0}, \quad \Gamma(0) = 1, \quad \sigma(0) = \mathbf{0}, \quad T(0) = T_0$$

**2. For each time step**  $n = 4$  to  $N$ , **do:**

- Evaluate time derivatives at  $t_{n-i}$  for  $i = 0, \dots, 4$ :

$$\dot{\square}_{n-i} = f(t_{n-i}, \square_{n-i})$$

- Compute the increment using ADAMS-BASHFORTH formula:

$$\Delta \square_n = \Delta t \sum_{i=0}^4 h_i \dot{\square}_{n-i}$$

- Update the state variable:

$$\square_{n+1} = \square_n + \Delta \square_n$$

- Repeat for each variable:  $\epsilon^{\text{in}}, \beta, \Gamma, \sigma, T$

**3. Return:** Updated states over all time steps.

---

### 3.1.3 Validation

To validate the Python implementation, basic HT tensile tests were simulated at two constant strain rates,  $\dot{\epsilon}_{22} = 5.0 \cdot 10^{-5} \text{ s}^{-1}$  and  $\dot{\epsilon}_{22} = 1.0 \cdot 10^{-4} \text{ s}^{-1}$ , in reference to [48]. The tests were performed at discrete temperature levels  $T \in \{673 \text{ K}, 773 \text{ K}, 873 \text{ K}, 923 \text{ K}\}$  to assess the model's thermomechanical response across a representative range. The resulting stress-strain curves, shown in Fig. 3.2, exhibited very good agreement with the data published in [48, 49]. This consistency confirms the model's capability to capture the temperature effects with high accuracy, and demonstrates the reliability of the numerical implementation for subsequent cyclic and multiscale simulations.

The resulting stress-strain curves obtained from the Python implementation closely match the reference data reported in the literature, both in terms of maximum stress levels and overall curve shape. This agreement across different temperatures and applied strain rates confirms the accuracy of the material model and validates the numerical integration procedure used.

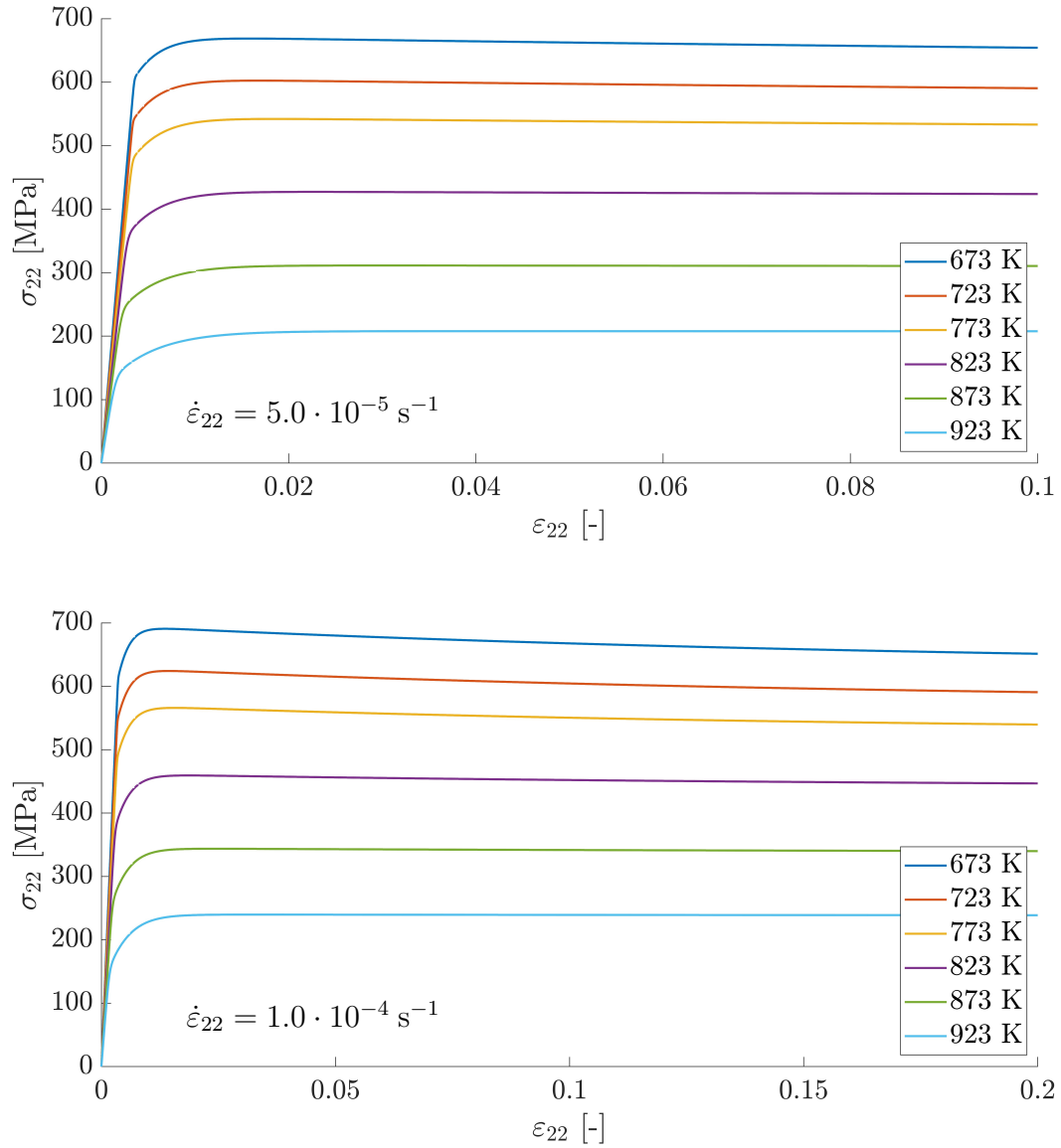


Figure 3.2: Results of the HT tensile tests with a the constant strain rates  $\dot{\varepsilon}_{22} = 1.0 \cdot 10^{-4} \text{ s}^{-1}$  and  $\dot{\varepsilon}_{22} = 5.0 \cdot 10^{-5} \text{ s}^{-1}$  at different temperatures

The cyclic benchmarks were also carried out via the FEM program ABAQUS. A simple model of a pipe is chosen where the load is applied at the upper edge and the results are extracted at the node depicted in blue on the left in Fig. 3.3. The mesh consists of CAX8R elements which are used for axisymmetric modeling of solid bodies. It's an 8-node biquadratic quadrilateral element, meaning each corner and mid-side point of the quadrilateral is defined by a node, making it a higher-order element which uses second-order interpolation to describe the displacements. The 'R' indicates a reduced integration scheme, applying less GAUSS points per element to calculate its stiffness matrix [1].

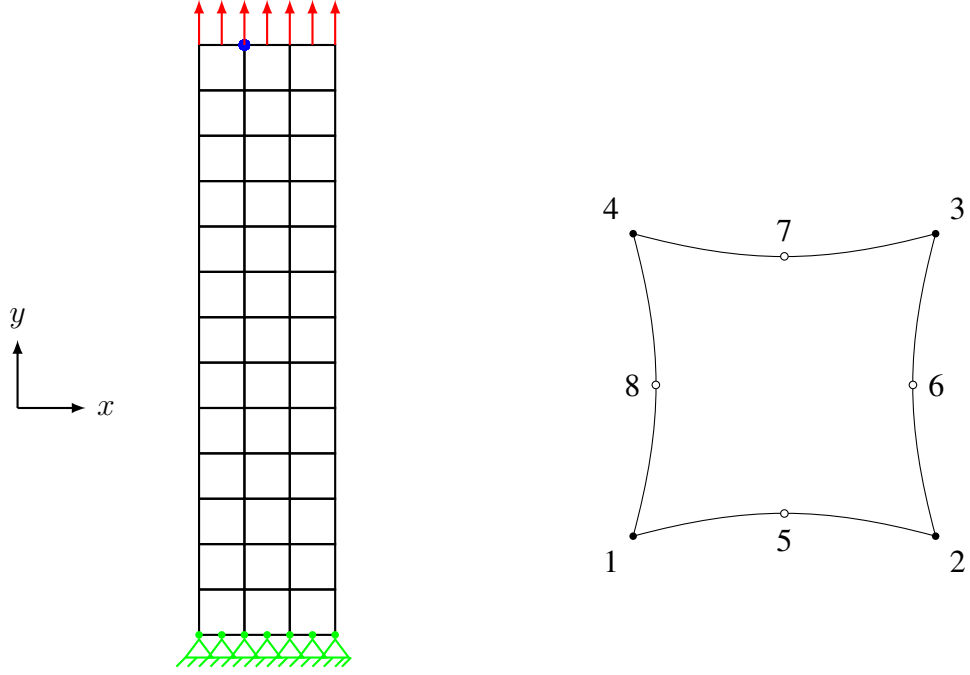


Figure 3.3: FEM model of the pipe including the loading direction as well as the point to extract the results from (left) and a schematic representation of the elements used (right)

### 3.1.3.1 Low Cycle Fatigue Test

At first, a uniaxial low cycle fatigue test with a strain rate of  $\dot{\epsilon} = 0.046 \frac{\%}{\text{min}}$  and a strain amplitude of  $\epsilon_a = 0.4\%$  at an absolute temperature of  $T = 873 \text{ K}$  is simulated. Figure 3.4 illustrates the cyclic stress response. The model is able to represent the FEM simulations accurately and captures the trends, such as the increase of the stress amplitude in the tensile region and its decrease in the compressive region, indicating that the model accurately reproduces both the magnitude and the trend of cyclic stress evolution under high-temperature conditions.

To further validate the temperature dependence of the model, additional simulations are conducted across a range of temperatures between  $773 - 923 \text{ K}$ , within the calibrated domain of the material model. Each simulation again includes three full cycles under identical mechanical loading conditions. The results are illustrated in Fig. 3.5, showing that the model reliably captures the temperature-sensitive nature of the material's stress response. In particular, both the maximum and minimum stress values are closely reproduced when compared with the ABAQUS simulations. The excellent agreement across varying temperature levels confirms the robustness of the Python-based implementation in representing the effects in cyclic loading scenarios.

To verify convergence of the chosen explicit time integration technique, additional simulations were performed using different time step sizes. The diagram in Fig. 3.6 shows, that the performance is stable since the error as the difference between the Python and FEM simulation is decreasing the smaller the time step  $\Delta t$  is chosen. The calculation is based on three cycles of the LCF profile at a temperature of  $T = 873 \text{ K}$  applying the EUCLIDEAN norm  $\|\cdot\|_2$  according to

$$\text{Error}(\Delta t) = \left( \frac{\|\sigma_{\text{Python}} - \sigma_{\text{Abaqus}}\|_2}{\|\sigma_{\text{Abaqus}}\|_2} \right). \quad (3.42)$$

This formulation provides a normalized, dimensionless measure of the deviation between both solutions, making it suitable for evaluating convergence behavior across different time step sizes. As evident from the plot, the relative error decreases consistently, indicating that the explicit scheme exhibits good numerical stability and convergence properties under low cycle fatigue loading.

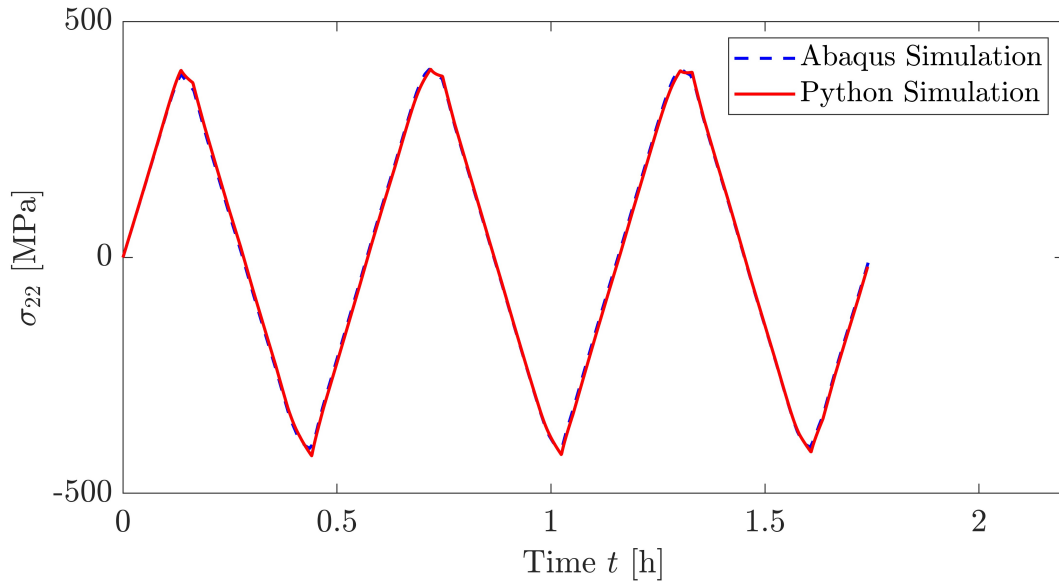


Figure 3.4: Simulation results of three cycles of the LCF test at elevated temperature and the comparison of them to the ABAQUS result

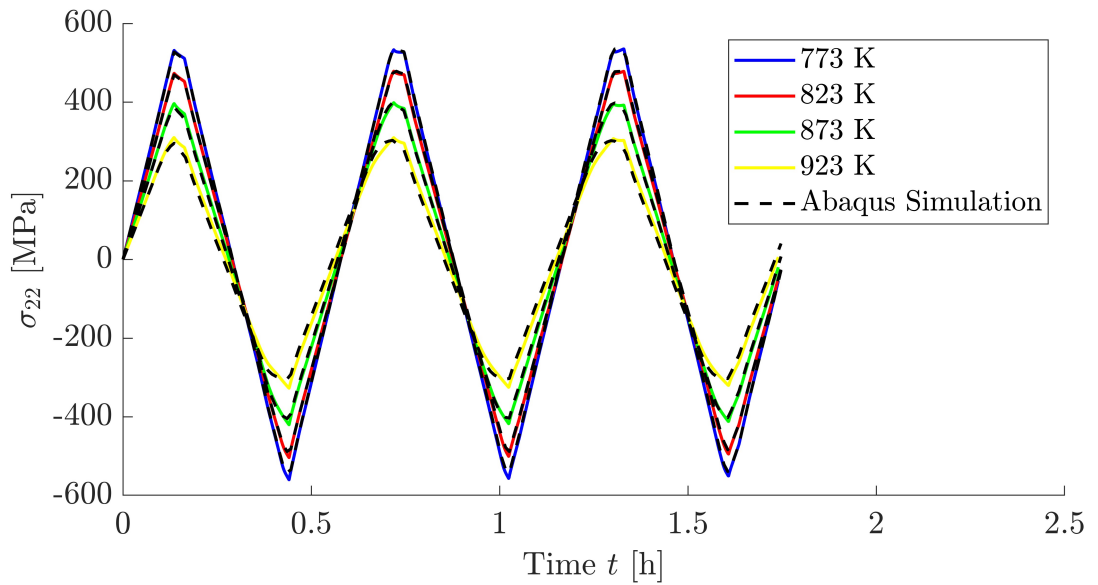


Figure 3.5: Simulation of the uniaxial low cycle fatigue test with respect to the different temperature levels compared to the corresponding ABAQUS simulation (dashed line)



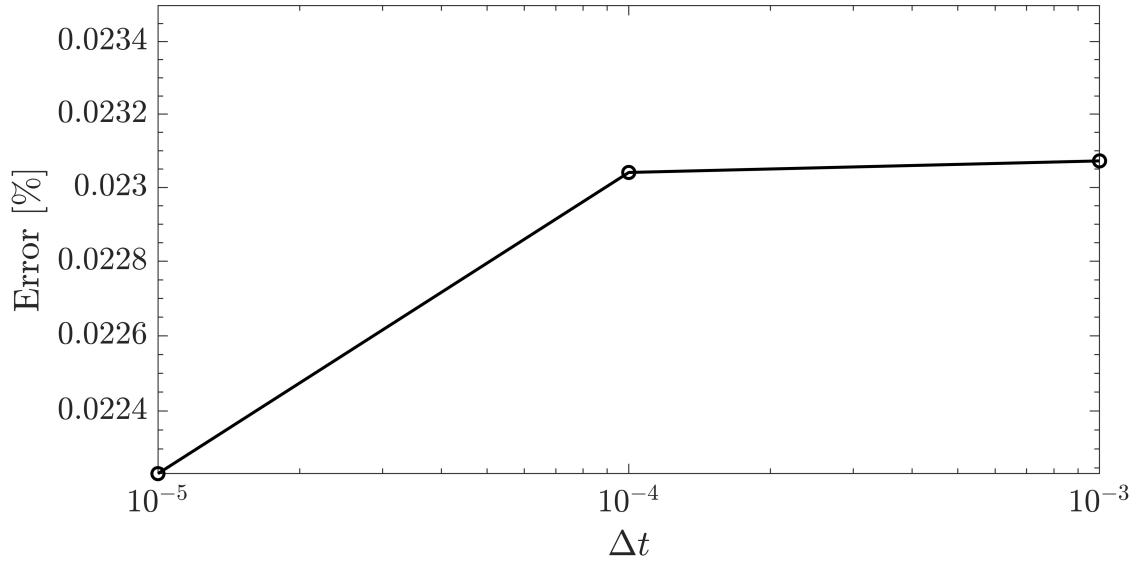


Figure 3.6: Convergence of the explicit time integration; logarithmic error vs. time step size

### 3.1.3.2 Thermo-Mechanical Fatigue Test

The second important benchmark is the thermo-mechanical fatigue test which includes a strain and temperature input. Both of them vary with respect to time as shown in Fig. 3.7. The corresponding simulation results are depicted in Fig. 3.8. This type of loading scenario is considerably more complex than isothermal LCF tests due to the simultaneous variation of both mechanical and thermal inputs over time. The coupling between strain and temperature introduces non-linear material behavior, which must be captured accurately by the constitutive model.

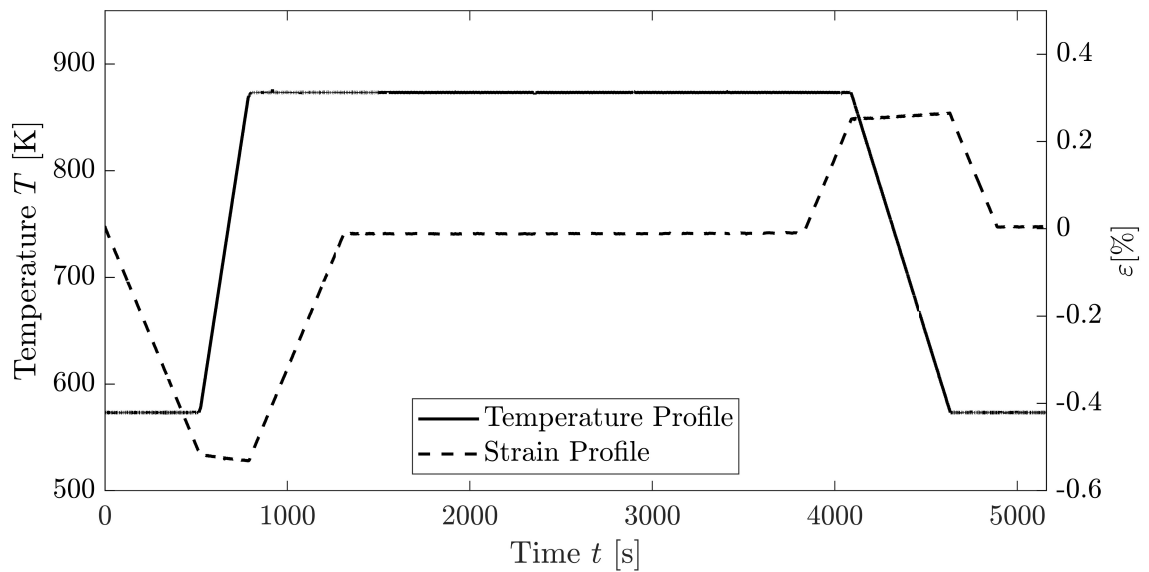


Figure 3.7: TMF test loading: strain and temperature profile after [87]

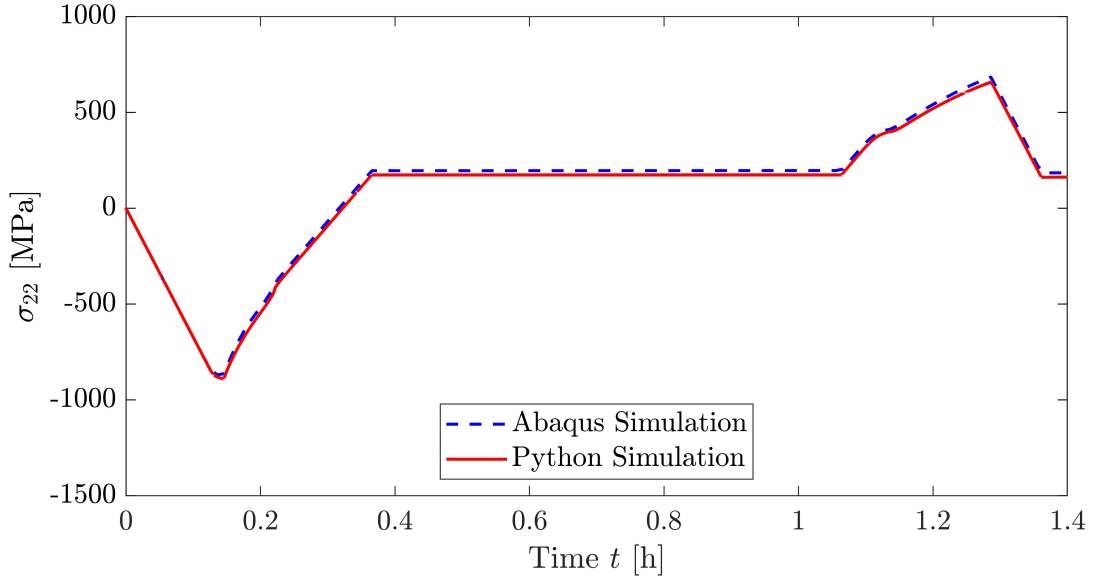


Figure 3.8: Comparison of the resulting material response between ABAQUS and Python simulations

Both of the cyclic benchmarks came to good agreement with the FEM results, the behavior with respect to the changing temperature and strain profiles was depicted well. Now, a series of TMF cycles is simulated as part of the real-life loading profile which power plant components are subjected to (see Fig. 3.9). It depicts a mixture of cold, warm and hot starts. The curve in Fig. 3.10 at the top left again shows that the Python simulation matches the FEM solution very well. To also ensure the correct behavior of the internal variables, their comparison is illustrated in the top right and the two figures at the bottom of Fig. 3.10.

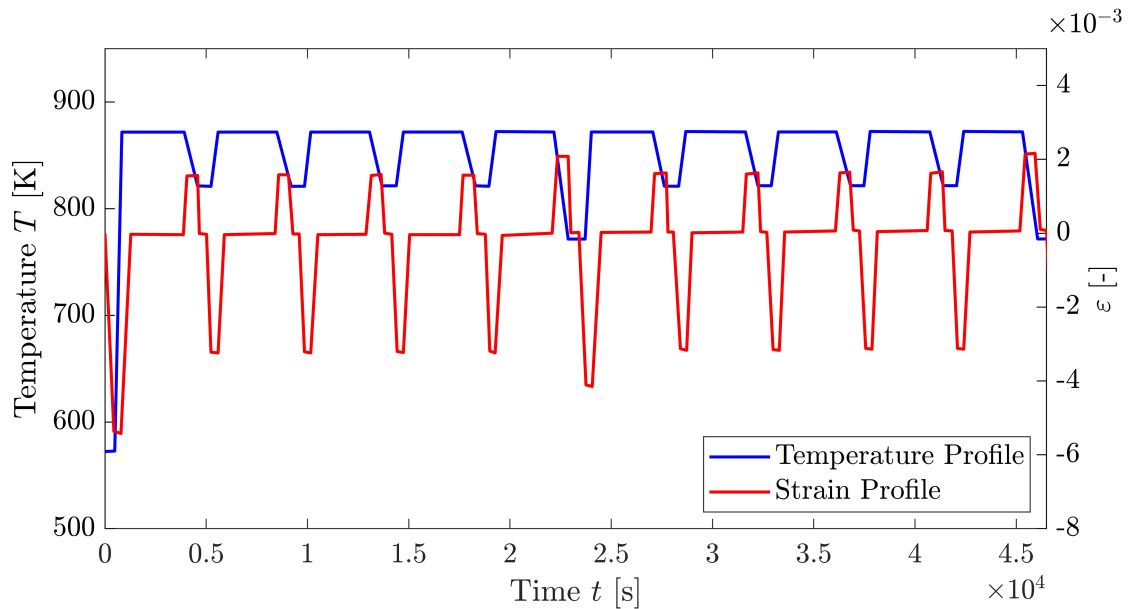


Figure 3.9: Service-type loading profile of a power plant component, including cold, warm as well as hot starts [87]

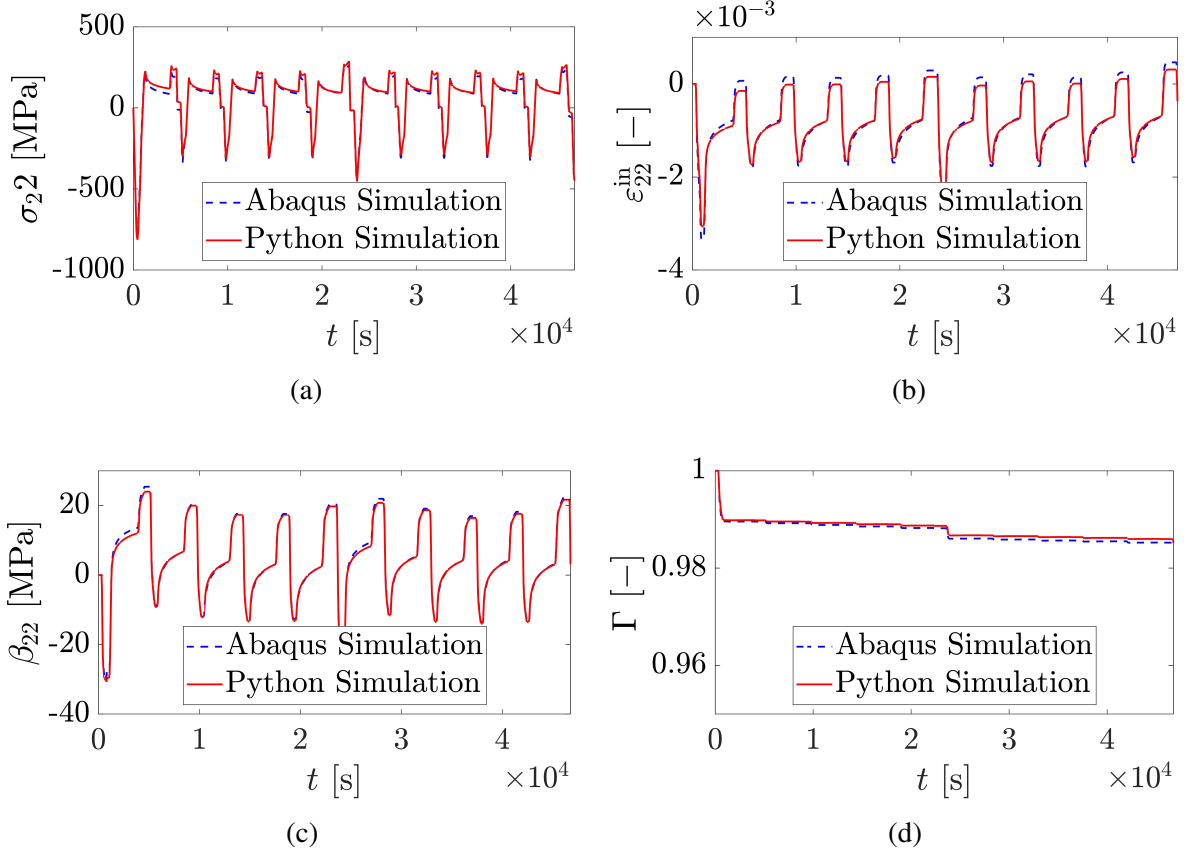


Figure 3.10: Results of the TMF profile: the stress (a) and the internal variables namely the inelastic strain  $\varepsilon_{22}^{\text{in}}$  (b), the backstress  $\beta_{22}$  (c) and the softening variable  $\Gamma$  (d)

In [87], normalized stress responses from both simulations and TMF tests are reported. A qualitative comparison shows that the results presented align well with the findings. Additionally, the bottom right diagram of Fig. 3.10 highlights a continuous increase in the softening variable  $\Gamma$  over the course of the cycles, indicating that the material undergoes progressive softening during TMF loading. The implemented Python model describes the stress behavior with sufficient accuracy, the trend of decreasing tensile stress amplitudes is accurately represented. Since all the results come to a good agreement, the model can be considered as validated.

## 3.2 Application of the Two-Time-Scale Approach

In general, the IBVP described in Subsect. 2.3.3 are expressed with respect to the two time scales in the following sections. The equilibrium condition yields

$$\nabla \cdot \boldsymbol{\sigma}(t_M, \tau) + \mathbf{f}(t_M, \tau) = \mathbf{0}. \quad (3.43)$$

The kinematic compatibility results in

$$\boldsymbol{\varepsilon}(t_M, \tau) = \frac{1}{2} [\nabla \mathbf{u}(t_M, \tau) + (\nabla \mathbf{u}(t_M, \tau))^T] \quad (3.44)$$

and the additive split of the strain is described by

$$\boldsymbol{\varepsilon}(t_M, \tau) = \boldsymbol{\varepsilon}^{\text{el}}(t_M, \tau) + \boldsymbol{\varepsilon}^{\text{in}}(t_M, \tau). \quad (3.45)$$

HOOKE's law can now also be expressed in terms of both the time scales

$$\boldsymbol{\sigma}(t_M, \tau) = K \operatorname{tr}(\boldsymbol{\varepsilon}^{\text{el}}(t_M, \tau)) \mathbf{I} + 2G\boldsymbol{\varepsilon}^{\text{el}}(t_M, \tau). \quad (3.46)$$

The detailed derivation of the constitutive equations including the evolution equations for the inelastic strain and the internal variables is explained in the next Subsect. 3.2.1.

### 3.2.1 Constitutive Equations

In this section, we derive the constitutive equations with respect to the two-time-scale approach meaning the equations and procedures introduced in Sect. 2.5 are now applied to the evolution equations describing the high-temperature steel X20CrMoV12-1 (Subsect. 3.1.1).

Considering Eq. (2.94), now  $\mathbf{x} = \boldsymbol{\varepsilon}^{\text{in}}, \beta$  and  $\Gamma$  have to be inserted in order to determine the equations which describe the multiscale problem. We now derive them for the case  $\mathbf{x} = \boldsymbol{\varepsilon}^{\text{in}}$ , where  $\mu$  defines the scaling parameter to express the temporal differences between the two scales so the total time derivative with respect to both of the time scales yields

$$\dot{\boldsymbol{\varepsilon}}^{\text{in}} = \frac{d\boldsymbol{\varepsilon}^{\text{in}}}{dt} = \frac{\partial \boldsymbol{\varepsilon}^{\text{in}}}{\partial t_M} + \frac{1}{\mu} \frac{\partial \boldsymbol{\varepsilon}^{\text{in}}}{\partial \tau}. \quad (3.47)$$

Now the concept of the asymptotic series expansion of the inelastic strain

$$\boldsymbol{\varepsilon}^{\text{in}} = \boldsymbol{\varepsilon}^{\text{in}(0)} + \mu \boldsymbol{\varepsilon}^{\text{in}(1)} + O(\mu^2) \quad (3.48)$$

is inserted on the right hand side into Eq. (3.47), considering the terms of the highest powers of the parameter  $\mu$  to be infinitesimally small

$$\dot{\boldsymbol{\varepsilon}}^{\text{in}} = \left( \frac{\partial \boldsymbol{\varepsilon}^{\text{in}(0)}}{\partial t_M} + \frac{1}{\mu} \frac{\partial \boldsymbol{\varepsilon}^{\text{in}(0)}}{\partial \tau} \right) + \mu \left( \frac{\partial \boldsymbol{\varepsilon}^{\text{in}(1)}}{\partial t_M} + \frac{1}{\mu} \frac{\partial \boldsymbol{\varepsilon}^{\text{in}(1)}}{\partial \tau} \right) + \dots \quad (3.49)$$

and sorted according to the orders of  $\mu$

$$\dot{\boldsymbol{\varepsilon}}^{\text{in}} = \frac{1}{\mu} \frac{\partial \boldsymbol{\varepsilon}^{\text{in}(0)}}{\partial \tau} + \left( \frac{\partial \boldsymbol{\varepsilon}^{\text{in}(0)}}{\partial t_M} + \frac{\partial \boldsymbol{\varepsilon}^{\text{in}(1)}}{\partial \tau} \right) + \mu \left( \frac{\partial \boldsymbol{\varepsilon}^{\text{in}(1)}}{\partial t_M} + \frac{1}{\mu} \frac{\partial \boldsymbol{\varepsilon}^{\text{in}(2)}}{\partial \tau} \right) + \dots \quad (3.50)$$

Substituting the left hand side of Eq. (3.50) with the series expansion according to (2.100) and equating the same orders of  $\mu$  yields the first part of the  $\mu^{(-1)}$ -order problem

$$\frac{\partial \boldsymbol{\varepsilon}^{\text{in}(0)}}{\partial \tau} = \mathbf{0}. \quad (3.51)$$

The analysis demonstrates that the zero-order inelastic strain is a function exclusively of the slow time scale  $t_M$  and remains invariant with respect to the fast time scale  $\tau$ . Consequently, the micro-scale problem reduces to a purely elastic formulation. This decoupling is also supported by the physical interpretation that inelastic strain represents a slowly evolving internal variable, characteristic of the material's long-term response [85].

Applying the same steps to the evolution equations for the backstress, Eq. (3.18) and to the softening variable, Eq. (3.19) then inserting in the IBVP and again equating terms of the same order of  $\mu$  results in

**the  $\mu^{(-1)}$ -order problem**

$$\frac{\partial \boldsymbol{\varepsilon}^{\text{in}(0)}}{\partial \tau} = \mathbf{0}, \quad (3.52)$$

$$\frac{\partial \boldsymbol{\beta}^{(0)}}{\partial \tau} = \mathbf{0}, \quad (3.53)$$

$$\frac{\partial \Gamma^{(0)}}{\partial \tau} = 0 \quad (3.54)$$

**and the  $\mu^{(0)}$ -order problem:**

$$\nabla \cdot \boldsymbol{\sigma}^{(0)}(t_M, \tau) + \mathbf{f}(t_M, \tau) = \mathbf{0}, \quad (3.55)$$

$$\boldsymbol{\varepsilon}(t_M, \tau) = \frac{1}{2} [\nabla \mathbf{u}^{(0)}(t_M, \tau) + (\nabla \mathbf{u}^{(0)}(t_M, \tau))^T], \quad (3.56)$$

$$\boldsymbol{\varepsilon}(t_M, \tau) = \boldsymbol{\varepsilon}^{\text{el}(0)}(t_M, \tau) + \boldsymbol{\varepsilon}^{\text{in}(0)}(t_M, \tau), \quad (3.57)$$

$$\boldsymbol{\sigma}^{(0)}(t_M, \tau) = K \text{tr}(\boldsymbol{\varepsilon}^{\text{el}(0)}(t_M, \tau)) \mathbf{I} + 2G \boldsymbol{\varepsilon}^{\text{el}(0)}(t_M, \tau), \quad (3.58)$$

$$\left( \frac{\partial \boldsymbol{\varepsilon}^{\text{in}(0)}}{\partial t_M} + \frac{\partial \boldsymbol{\varepsilon}^{\text{in}(1)}}{\partial \tau} \right) = \frac{3}{2} f_\sigma(\tilde{\sigma}_{\text{vM}}^{(0)}) f_T(T) \frac{\tilde{\boldsymbol{\sigma}}'^{(0)}}{\tilde{\sigma}_{\text{vM}}^{(0)}}, \quad (3.59)$$

$$\begin{aligned} \left( \frac{\partial \boldsymbol{\beta}^{(0)}}{\partial t_M} + \frac{\partial \boldsymbol{\beta}^{(1)}}{\partial \tau} \right) &= \frac{1}{G(T)} \frac{dG(T)}{dT} \dot{T} \boldsymbol{\beta}^{(0)} \\ &+ 2G(T) \frac{\eta_{h0}}{1 - \eta_{h0}} \left( \dot{\boldsymbol{\varepsilon}}^{\text{in}(0)} - \frac{3}{2} \frac{\dot{\boldsymbol{\varepsilon}}_{\text{vM}}^{\text{in}(0)}}{\beta_{\text{vM}}(\sigma_{\text{vM}}^{(0)})} \boldsymbol{\beta}^{(0)} \right), \end{aligned} \quad (3.60)$$

$$\left( \frac{\partial \Gamma^{(0)}}{\partial t_M} + \frac{\partial \Gamma^{(1)}}{\partial \tau} \right) = C_\Gamma \left[ \Gamma_\star(\sigma_{\text{vM}}^{(0)}) - \Gamma^{(0)} \right] \dot{\boldsymbol{\varepsilon}}_{\text{vM}}^{\text{in}(0)} \quad (3.61)$$

in the case of X20CrMoV12-1 steel. The Eqs. (3.52)-(3.54) show that at order 0, the inelastic strain  $\boldsymbol{\varepsilon}^{\text{in}(0)}$ , the backstress  $\boldsymbol{\beta}^{(0)}$  and the softening  $\Gamma^{(0)}$  are only depending on the slow time, so the fast part of the evolution vanishes leading to

$$\boldsymbol{\varepsilon}^{\text{in}(0)}(t_M, \tau) = \boldsymbol{\varepsilon}^{\text{in}(0)}(t_M), \quad (3.62)$$

$$\boldsymbol{\beta}^{(0)}(t_M, \tau) = \boldsymbol{\beta}^{(0)}(t_M), \quad (3.63)$$

$$\Gamma^{(0)}(t_M, \tau) = \Gamma^{(0)}(t_M). \quad (3.64)$$

### 3.2.1.1 Macrochronological Problem

For solving the  $\mu^{(0)}$ -order problem, the equations now have to be decomposed into a macro and micro part, meaning a slow and a fast changing portion according to Eq. (2.106). The time averaging operator with respect to the fast scale  $\mathcal{M}$  introduced in Eq. (2.108) is used on Eqs. (3.59)-(3.61) to obtain the decomposition [69, 70]. In general, the slow scale  $\mathbf{u}(t)$  and fast scale problem  $\mathbf{v}(\tau)$  can be written including the period  $P$  as

$$\frac{d\mathbf{u}(t)}{dt} = \mu f(\mathbf{u}(t), \mathbf{v}_{\mathbf{u}(t)}(t)), \quad u(0) = u_0, \quad (3.65)$$

$$\frac{d\mathbf{v}(t)}{dt} = g(\mathbf{u}(t), \mathbf{v}(t)), \quad v(P) = v(0), \quad (3.66)$$

where the functions  $f$  and  $g$  are differential operators. The macrochronological problem then includes

$$\nabla \cdot \boldsymbol{\sigma}_M^{(0)}(t_M) + \mathbf{f}_M(t_M) = \mathbf{0}, \quad (3.67)$$

$$\boldsymbol{\varepsilon}_M(t_M) = \frac{1}{2} \left[ \nabla \mathbf{u}_M^{(0)}(t_M) + (\nabla \mathbf{u}_M^{(0)}(t_M))^T \right], \quad (3.68)$$

$$\boldsymbol{\varepsilon}_M(t_M) = \boldsymbol{\varepsilon}_M^{\text{el}(0)}(t_M) + \boldsymbol{\varepsilon}_M^{\text{in}(0)}(t_M), \quad (3.69)$$

$$\boldsymbol{\sigma}_M^{(0)}(t_M) = K \operatorname{tr} \left( \boldsymbol{\varepsilon}_M^{\text{el}(0)}(t_M) \right) \mathbf{I} + 2G \boldsymbol{\varepsilon}_M^{\text{el}(0)}(t_M). \quad (3.70)$$

The evolution equations of the  $\mu^{(0)}$ -order on the macro scale are now

$$\left\langle \frac{d\mathbf{U}(t_M)}{dt_M} \right\rangle = \mathcal{M}(f(\mathbf{v}_{\langle \mathbf{U}(t_M) \rangle}(\tau), \langle \mathbf{U}(t_M) \rangle)), \quad \langle U(0) \rangle = \langle U_0 \rangle, \quad (3.71)$$

or in particular

$$\left\langle \frac{d\boldsymbol{\varepsilon}^{\text{in}}(t_M)}{dt_M} \right\rangle = \mathcal{M} \left( \frac{3}{2} f_\sigma(\tilde{\sigma}_{\text{vM}}(\tau)) f_T(T(t_M)) \frac{\tilde{\sigma}'(\tau)}{\sigma_{\text{vM}}(\tau)} \right), \quad (3.72)$$

$$\begin{aligned} \left\langle \frac{d\boldsymbol{\beta}(t_M)}{dt_M} \right\rangle &= \mathcal{M} \left( \frac{1}{G(T)} \frac{dG(T)}{dT} \frac{dT(t_M)}{dt_M} \langle \boldsymbol{\beta}(t_M) \rangle \right) \\ &+ \mathcal{M} \left( 2G(T) \frac{\eta_{h0}}{1 - \eta_{h0}} \left[ \frac{d \langle \boldsymbol{\varepsilon}^{\text{in}}(t_M) \rangle}{dt_M} - \frac{3}{2} \frac{\dot{\boldsymbol{\varepsilon}}_{\text{vM}}^{\text{in}}(t_M)}{\beta_{\text{vM}}(\sigma_{\text{vM}})} \langle \boldsymbol{\beta}(t_M) \rangle \right] \right), \end{aligned} \quad (3.73)$$

$$\left\langle \frac{d\Gamma(t_M)}{dt_M} \right\rangle = \mathcal{M} \left( C(\Gamma^*(\sigma_{\text{vM}}(\tau)) - \langle \Gamma(t_M) \rangle) \dot{\boldsymbol{\varepsilon}}_{\text{vM}}^{\text{in}}(t_M) \right). \quad (3.74)$$

Here, only the terms up to the first order of  $\mu$  were considered. Higher orders may be calculated according to [140]. Eqs.(3.72)-(3.74) can be rewritten in terms of the slow and fast scale

dependencies as

$$\dot{\epsilon}_M^{\text{in}(0)} = \frac{\partial \epsilon^{\text{in}(0)}}{\partial t_M} = \frac{\partial \epsilon^{\text{in}(0)}(\sigma_M^{(0)} + \sigma_m^{(0)})}{\partial t_M}, \quad (3.75)$$

$$\dot{\beta}_M^{(0)} = \frac{\partial \beta^{(0)}(\dot{\epsilon}_M^{\text{in}(0)})}{\partial t_M}, \quad (3.76)$$

$$\dot{\Gamma}_M^{(0)} = \frac{\partial \Gamma^{(0)}(\dot{\epsilon}_M^{\text{in}(0)})}{\partial t_M}. \quad (3.77)$$

Where, due to the fast time periodicity assumption the average of

$$\left\langle \frac{\partial}{\partial \tau} \epsilon^{\text{in}(1)}(t_M, \tau) \right\rangle = 0 \quad (3.78)$$

vanishes. Similarly, the averages of  $\frac{\partial}{\partial \tau} \beta^{(1)}(t_M, \tau)$  and  $\frac{\partial}{\partial \tau} \Gamma^{(1)}(t_M, \tau)$  disappear.

The macrochronological problem governs the slow evolution of the internal variables by incorporating the average influence of the fast-scale response over a given period. The derived equations show that the inelastic strain, backstress, and softening evolve on the slow time scale and are driven by the averaged quantities from the microchronological problem. This separation enables efficient computation while preserving the essential long-term behavior of the material under cyclic loading.

### 3.2.1.2 Microchronological Problem

Due to the result  $\epsilon_m^{\text{in}(0)}(t_M, \tau) = \mathbf{0}$  showing that the fast part of the evolution of the inelastic strain at order 0 is blocked, the microchronological problem yields

$$\nabla \cdot \sigma_m^{(0)}(t_M, \tau) + \mathbf{f}_m(t_M, \tau) = \mathbf{0}, \quad (3.79)$$

$$\epsilon_m(t_M, \tau) = \frac{1}{2} [\nabla \mathbf{u}_m^{(0)}(t_M, \tau) + (\nabla \mathbf{u}_m^{(0)}(t_M, \tau))^T], \quad (3.80)$$

$$\epsilon_m(t_M, \tau) = \epsilon_m^{\text{el}(0)}(t_M, \tau), \quad (3.81)$$

$$\sigma_m^{(0)}(t_M, \tau) = K \text{tr}(\epsilon_m^{\text{el}(0)}(t_M, \tau)) \mathbf{I} + 2G \epsilon_m^{\text{el}(0)}(t_M, \tau). \quad (3.82)$$

The fast scale variable depending on the slow scale is therefore defined as  $\mathbf{v}(\tau) = \sigma(\tau)$

$$\frac{d\mathbf{v}_{\langle U(t_M) \rangle}(\tau)}{d\tau} = g(\langle U(t_M) \rangle, \mathbf{v}_{\langle U(t_M) \rangle}(\tau)), \quad \mathbf{v}_{\langle U(t_M) \rangle}(t_n + P) = \mathbf{v}_{\langle U(t_M) \rangle}(t_n) \quad (3.83)$$

yielding

$$\begin{aligned} \frac{d\sigma_{\langle U(t_M) \rangle}}{d\tau} = & \lambda(T(\tau)) \text{tr} \left( \frac{d\epsilon(\tau)}{d\tau} - \frac{d\langle \epsilon^{\text{in}}(t_M) \rangle}{dt_M} \right) \mathbf{I} + \dot{\lambda} \text{tr}(\epsilon(\tau) - \epsilon^{\text{in}}(t_M)) \\ & + 2\mu(T(\tau)) \left( \frac{d\epsilon(\tau)}{d\tau} - \frac{d\langle \epsilon^{\text{in}}(t_M) \rangle}{dt_M} \right) + 2\dot{\mu}(\epsilon(\tau) - \epsilon^{\text{in}}(t_M)) \end{aligned} \quad (3.84)$$

with the temperature dependence of the LAMÉ parameters

$$\dot{\lambda} = \frac{d\lambda}{dT} \frac{dT}{d\tau}, \quad \dot{\mu} = \frac{d\mu}{dT} \frac{dT}{d\tau}. \quad (3.85)$$

The microchronological problem captures the rapid stress response of the material while assuming that the internal variables remain fixed over the fast scale. By resolving the short-term elastic dynamics within each period and feeding the result into the macro-scale evolution equations, the fast-scale problem enables accurate representation of the material's response without requiring full-resolution simulations at every time step. This decoupling is key to reducing computational cost while retaining physical fidelity.

### 3.2.2 Implementation

Considering the slow and fast variables, the temporal multiscale problem is fully defined by Eqs. (3.67)-(3.84) and can be solved in a staggered manner [123, 132]. This scheme reflects the separation of time scales: slow-evolving internal variables (e.g., inelastic strain, backstress, softening) evolving over macro time  $t_M$ , while fast fluctuations (e.g., stress response) are resolved over a fast time  $\tau$ . The solutions of the fast and slow processes are coupled through a time-averaging operation with respect to the fast scale  $\tau$ . The primary benefit of this decomposition lies in the efficiency of solving high-fidelity microproblems only locally in time, while still capturing the long-term evolution of internal state variables relevant for the inelastic behavior in materials like X20CrMoV12-1.

In the first step, the given periodic strain profile is additively divided into a mean and fluctuation part

$$\epsilon = \epsilon(t_M) + \epsilon(t_M, \tau) = \bar{\epsilon} + \epsilon(\tau) \quad (3.86)$$

or slow and fast portion respectively, with  $\bar{\epsilon}$  describing the medium strain. The two parts are calculated using a fast FOURIER transformation (FFT) to decompose the signal in its main parts, the direct current component which is also referred to as mean or average value operating in the slow scale and the oscillatory component representing the fast part  $\epsilon(\tau)$ . From Eqs. (3.75) - (3.77) it is evident that the macro scale evolution is depending on the microchronological solution  $\sigma_m$ . The slow-scale  $u(t_M)$  is treated as constant for each slow time step  $\Delta t_M$  during each fast time interval while the fast scale problem is solved. Consequently, the microchronological problem iterates in a fixed macrochronological point until local periodicity is achieved. After updating the fast scale variables, they serve as input for the slow scale problem which is solved afterwards. The average over one fast period is used to solve the right hand side of the evolution



equations of the slow variables

$$\frac{d}{dt} \begin{bmatrix} \epsilon^{\text{in}} \\ \beta \\ \Gamma \end{bmatrix} = \begin{bmatrix} \langle \dot{\epsilon}^{\text{in}} \rangle \\ \langle \dot{\beta} \rangle \\ \langle \dot{\Gamma} \rangle \end{bmatrix} = \begin{bmatrix} \frac{1}{P} \int_0^P \frac{3}{2} f_\sigma(\tilde{\sigma}_{\text{vM}}(\tau)) f_T(T(t_M)) \frac{\tilde{\sigma}'(\tau)}{\tilde{\sigma}_{\text{vM}}(\tau)} d\tau \\ \frac{1}{P} \int_0^P \left( \frac{1}{G(T)} \frac{dG(T)}{dT} \frac{dT(t_M)}{dt_M} \langle \beta(t_M) \rangle + 2G(T) \frac{\eta_{h0}}{1 - \eta_{h0}} \left[ \frac{d \langle \epsilon^{\text{in}}(t_M) \rangle}{dt_M} - \frac{3}{2} \frac{\epsilon_{\text{vM}}^{\text{in}}(t_M)}{\beta_{\text{vM}}(\sigma_{\text{vM}})} \langle \beta(t_M) \rangle \right] \right) d\tau \\ \frac{1}{P} \int_0^P C(\Gamma^*(\sigma_{\text{vM}}(\tau)) - \langle \Gamma(t_M) \rangle) \dot{\epsilon}_{\text{vM}}^{\text{in}}(t_M) d\tau \end{bmatrix}. \quad (3.87)$$

The averaging of the variables with respect to the fast scale  $\tau$  is numerically obtained by the trapezoidal rule. With the right hand side being calculated, the macro or slow problem can be integrated over one slow time step  $\Delta t_M$ . In the thesis at hand, the ADAMS-BASHFORTH integration method explained in Subsect. 2.4.1 is employed to integrate the multiscale constitutive equations with respect to time

$$\langle \mathbf{U}(t_{M+1}) \rangle = \langle \mathbf{U}(t_M) \rangle + \Delta t_M \cdot \Phi^{(5)}[\langle \dot{\mathbf{U}} \rangle] \quad (3.88)$$

with  $\mathbf{U}$  being the vector of all slow scale variables and where the multistep update  $\Phi^{(5)}$  is defined as

$$\begin{aligned} \Phi^{(5)} = \frac{1}{720} \bigg[ & 1901 \langle \dot{\mathbf{U}}(t_M) \rangle - 2774 \langle \dot{\mathbf{U}}(t_{M-1}) \rangle \\ & + 2616 \langle \dot{\mathbf{U}}(t_{M-2}) \rangle - 1274 \langle \dot{\mathbf{U}}(t_{M-3}) \rangle + 251 \langle \dot{\mathbf{U}}(t_{M-4}) \rangle \bigg]. \end{aligned} \quad (3.89)$$

This integration method allows efficient explicit time-stepping on the macro-scale without solving nonlinear systems. It relies on the assumption that the fast-scale problem has been solved and the corresponding right-hand sides, the averaged variables are known. The updated values serve as input for the next microchronological time step. The final fast state, e.g.  $\sigma(\tau = P)$  is stored which serves as IC for the next macro time step  $t_{M+1}$ , meaning the next triggered microchronological solution at the next macro time point.

The coupling is such that the fast problem must be solved first to inform the evolution of the slow variables. This ensures consistency with the asymptotic expansion and maintains the separation of scales. The basic working principle of the two-time-scale procedure in general can be found in Algorithm 2 which is schematically depicted in Fig. 3.11.

The application of the two-time-scale approach relies on the assumption that the fast-scale variables exhibit periodic behavior. Consequently, it is essential to verify this assumption during simulation. Numerically, several methods exist to assess periodicity, but the first step involves identifying the period  $P$ . This is achieved using a FFT, which converts the signal into the frequency domain. Dominant peaks in the frequency spectrum indicate the principal periods of the data [24]. To assess whether the solution has reached a periodic state, the present work employs a 'last element check'. Rather than evaluating periodicity over the entire time interval, this method compares only the final solution state of two consecutive cycles.

---

**Algorithm 2** General algorithm to describe the implementation of the two-time-scale approach

---

1. Initialize the slow variable  $\langle \mathbf{U}(t_M) \rangle$  and fast variable  $\mathbf{v}_{\langle \mathbf{U}(t_M) \rangle}(\tau)$  at  $t_M = t_{M_0}$
  2. Iterate in time from  $t_{M_0}$  to  $t_{M_n}$ :
    - a) Solve the microchronological (fast) problem with the slow variable fixed, using fixed-point iteration:
      - Initialize time window  $\tau \in [t_k, t_k + P]$  where  $P$  is the fast-scale period
      - Solve the fast problem over  $[\tau_0, \tau_1, \dots, \tau_n]$  with initial state  $\mathbf{U}_0$
      - Repeat
        - Use final state from previous period as new initial condition
        - Solve again over  $[\tau_0, \tau_1, \dots, \tau_n]$
        - Check convergence to periodicity using periodicity functional
      - until convergence or maximum number of iterations reached
    - b) Solve the macrochronological (slow) problem averaged with respect to the microchronological problem
      - Average fast-scale quantities over the converged period
      - Integrate slow ODE using these averaged values
    - c) Update the solution of the slow variable to  $\langle \mathbf{U}(t_{M+1}) \rangle$
    - d) Set the initial fast state for the next step equal to the final state from the converged fast-scale solution
  3. Return the macrochronological (slow) solution
- 

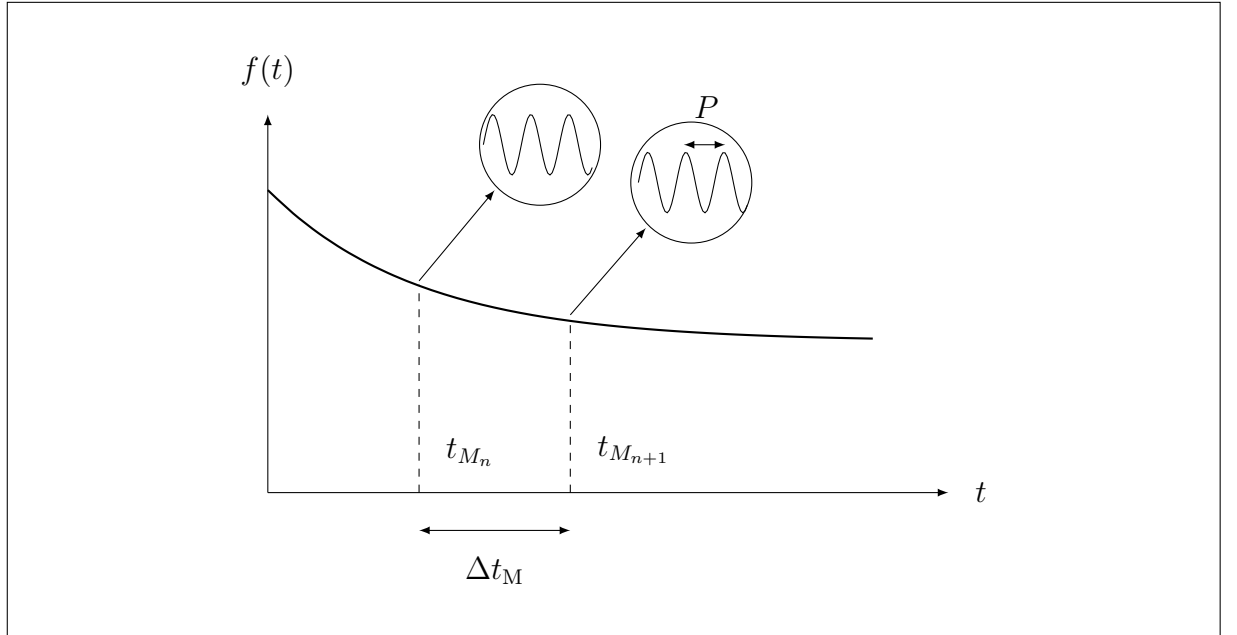


Figure 3.11: Scheme of the steps taken to solve the multiscale problem with respect to the fast and slow time scales  $\tau$  and  $t_M$  after [85]

Specifically, it computes the relative error between the stress tensors of the last time points in the reference and current cycles as

$$\left\| \frac{\sigma_{\text{ref}}^{\text{last}} - \sigma_{\text{cur}}^{\text{last}}}{\sigma_{\text{ref}}^{\text{last}}} \right\| < 10^{-3}. \quad (3.90)$$

The scalar error is then compared against a predefined relative tolerance, which is set to be  $10^{-3}$ . If the condition is met, periodicity is assumed. This criterion is computationally efficient and offers a simple scalar condition for convergence. However, applying the same scalar tolerance across all tensor components can be restrictive when dealing with quantities of varying magnitudes or when fast-scale variables involve multiple physical mechanisms. To address this, a vectorial tolerance criterion may be introduced, which allows for more flexible, component-wise control over periodicity assessment [33, 135, 143].

The overall program flowchart illustrating the numerical implementation of the two-time-scale approach for the implementation is shown in Fig. 3.12. The implementation of the two-time-scale algorithm follows a staggered scheme, alternating between the microchronological and macrochronological problems. The stress response is computed on the fast scale, while the internal variables evolve on the slow scale based on averaged quantities. The ADAMS-BASHFORTH integration method is used to advance the slow-scale solution efficiently. A convergence check ensures periodicity at each macro time step. This structure allows accurate modeling of long-term material behavior with significantly reduced computational cost.

### 3.2.3 Validation

The algorithm described in the previous Subsect. 3.1.3 is now carried out to validate the implementation of the multiscale procedure. Due to the periodicity assumption concerning the fast scale variables, a fourier transformation is applied to the strain input from the experiment or it has to be fitted so that the satisfaction of the periodicity check in the code is guaranteed. In Eq. (3.91), a sine function consisting of one term is chosen

$$y_1(x) = s_1 (\sin(s_2 x + s_3)). \quad (3.91)$$

The curve fitting was done using the least mean square error method. The function coefficients and the root mean square error (RMSE), which quantifies the average deviation between predicted and experimental values are also displayed in Table 3.2. Figure 3.13 shows the fit graphically compared to the experimental input data <sup>1</sup>.

Table 3.2: Coefficients and root mean square error to the function described in Eq. (3.91)

Function	RMSE	Coefficients		
$y_1$	0.00028	$s_1 = 0.00321$	$s_2 = 10.7490$	$s_3 = -6.31$

<sup>1</sup>Kostenko, Y., Almstedt, H., Scholz, A., Linn, S., Naumenko, K., Kutschke, A., Prygorniev, O. (2012). Langzeitdehnverhalten (LCF-Ermüdung) von großen Dampfturbinenkomponenten im Hochtemperaturbereich. *Verbundprojekt COORETEC-Turbo III*.

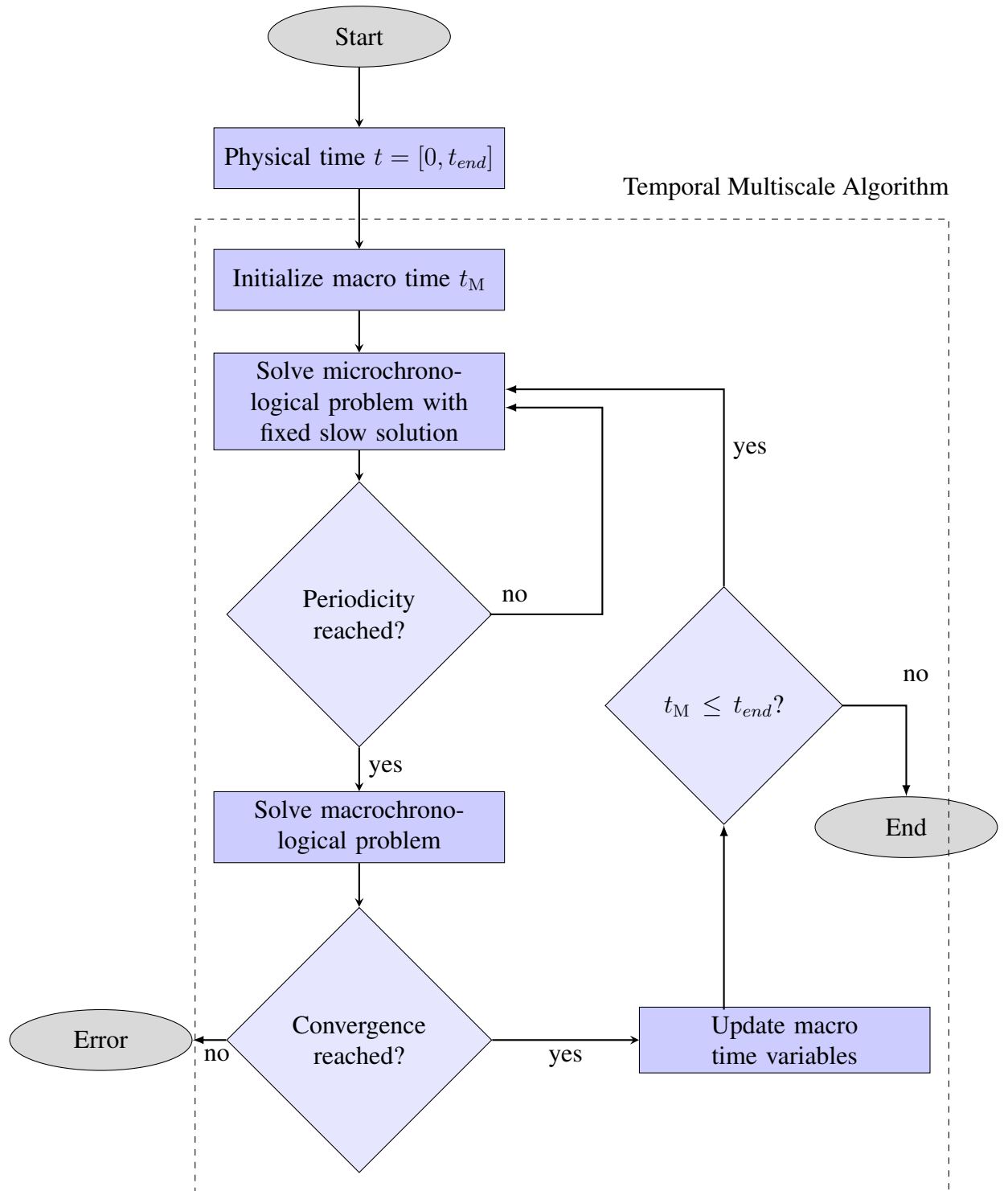


Figure 3.12: Program flowchart for the implementation of the two-time-scale approach for solving the constitutive equations for high temperature steel

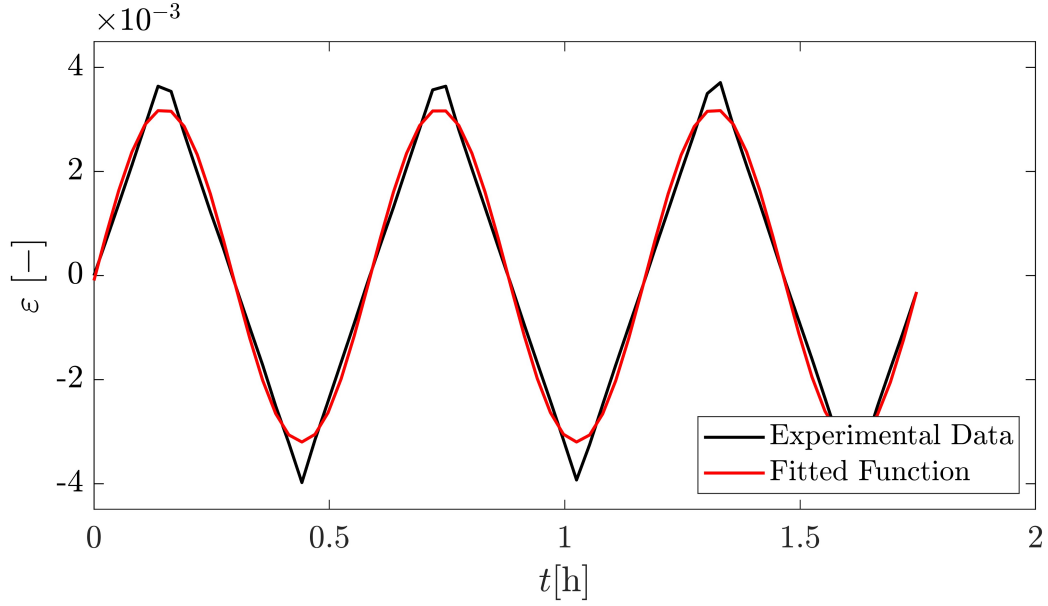


Figure 3.13: Comparison of the experimental input and the fitted sine function

In the remainder of this section, we use the fitted sine function profile in Eq. (3.92) with the angular frequency  $\omega = s_2$  and the phase angle  $\varphi = s_3$  to gain results from both, the fully resolved problem and the multiscale code

$$\varepsilon(t) = s_1 \sin(\omega t - \varphi) = 0.00321 \sin(10.749t - 6.31) \quad (3.92)$$

with the initial conditions

$$\begin{aligned} \varepsilon^{\text{in}}(t_M = 0, \tau = 0) &= \mathbf{0}, & \beta(t_M = 0, \tau = 0) &= \mathbf{0}, \\ \Gamma(t_M = 0, \tau = 0) &= 1, & \sigma(t_M = 0, \tau = 0) &= \mathbf{0}. \end{aligned} \quad (3.93)$$

To address the oscillating behavior in the evolution of the inelastic strain  $\varepsilon^{\text{in}}$  and the back-stress  $\beta$  which can be observed in the fully resolved simulation, a scaling parameter was introduced in the averaging procedure of the multiscale simulation framework. This parameter compensates for the discrepancy in amplitude and temporal behavior between the fluctuating variables, and the softening variable  $\Gamma$ , which evolves more smoothly and consistently over the slow timescale. The inclusion of the scaling factor ensures a better representation of scale separation, aligning the effective evolution rates of all slow variables. It also contributes to improved numerical stability, preventing extreme derivative magnitudes that can lead to stiff system behavior and convergence failures in the ODE solver. This approach is consistent with established strategies in multiscale and homogenization literature, where scaling is often applied to reconcile disparate micro- and macro-scale dynamics [158]. By regulating the averaged contributions of  $\beta$  and  $\varepsilon^{\text{in}}$ , the simulation not only respects the underlying physical timescales but also remains computationally robust.

To validate the multiscale algorithm, initial comparisons were made with a fully resolved elastic simulation. In this regime, the slow-scale variables do not yet influence the fast dynamics, making it an ideal case for assessing whether the averaging procedure correctly captures the macrochronological behavior. Because elastic responses are primarily governed by the fast-scale

dynamics, any mismatch between the fully resolved and averaged simulations can be clearly attributed to the performance of the averaging scheme itself, without interference from complex multiscale interactions. This makes the elastic case a reliable baseline for verifying that the slow-scale evolution is being accurately captured before progressing to inelastic or more strongly coupled scenarios. In the beginning, 100 cycles of the fitted sine function were simulated with the fully resolved and the multiscale Python code. The chosen time step for the fully resolved simulation with the unit corresponding to the input was

$$\Delta t = 10^{-2} \text{ h.} \quad (3.94)$$

In order to simulate the LCF profile with the multiscale method, the following time steps were chosen

$$\Delta t_M = 10 P, \quad \Delta \tau = P \times 10^{-3} \quad (3.95)$$

resulting in a scaling factor of

$$\mu = 10^{-4}. \quad (3.96)$$

The comparison of the elastic simulations with respect to the stress came to a close agreement as shown in Fig. 3.14. Additionally, the averaging procedure captured the behavior of the internal variables well, see Fig 3.15.

After the validation of the averaging procedure, the same amount of cycles was calculated again, using the complete multiscale scheme including the slow variables in the fast scale. In Table 3.3, the reduction of the computational time is shown for the profile containing 100 loading cycles.

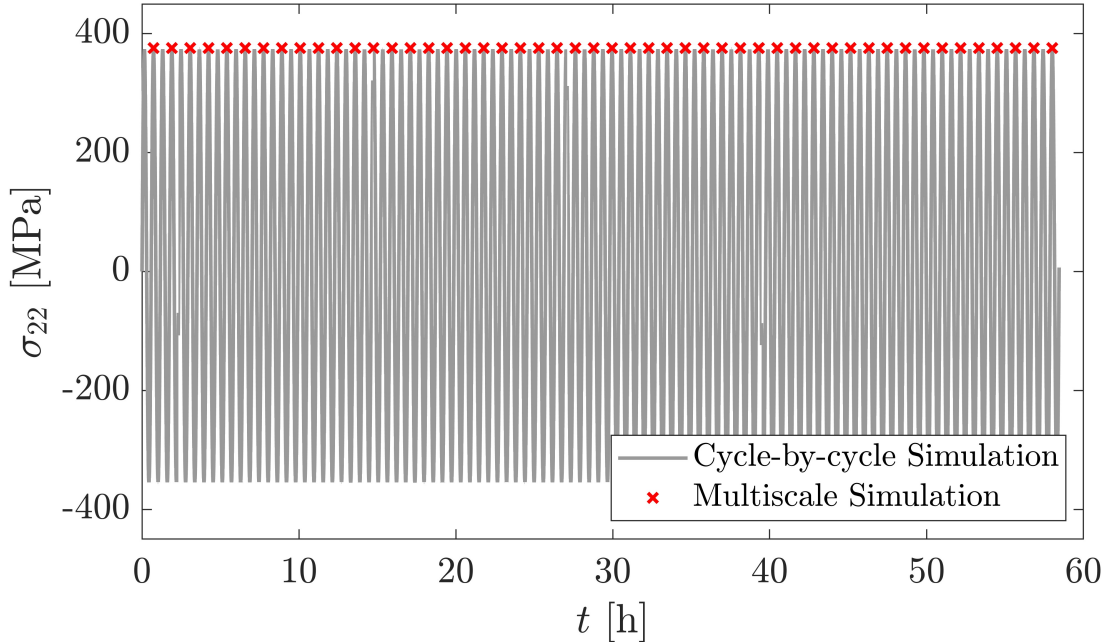


Figure 3.14: Comparison of the elastic cycle-by-cycle simulation with the elastic temporal multiscale algorithm for  $N = 100$  cycles

### 3 Numerical Implementation for X20CrMoV12-1

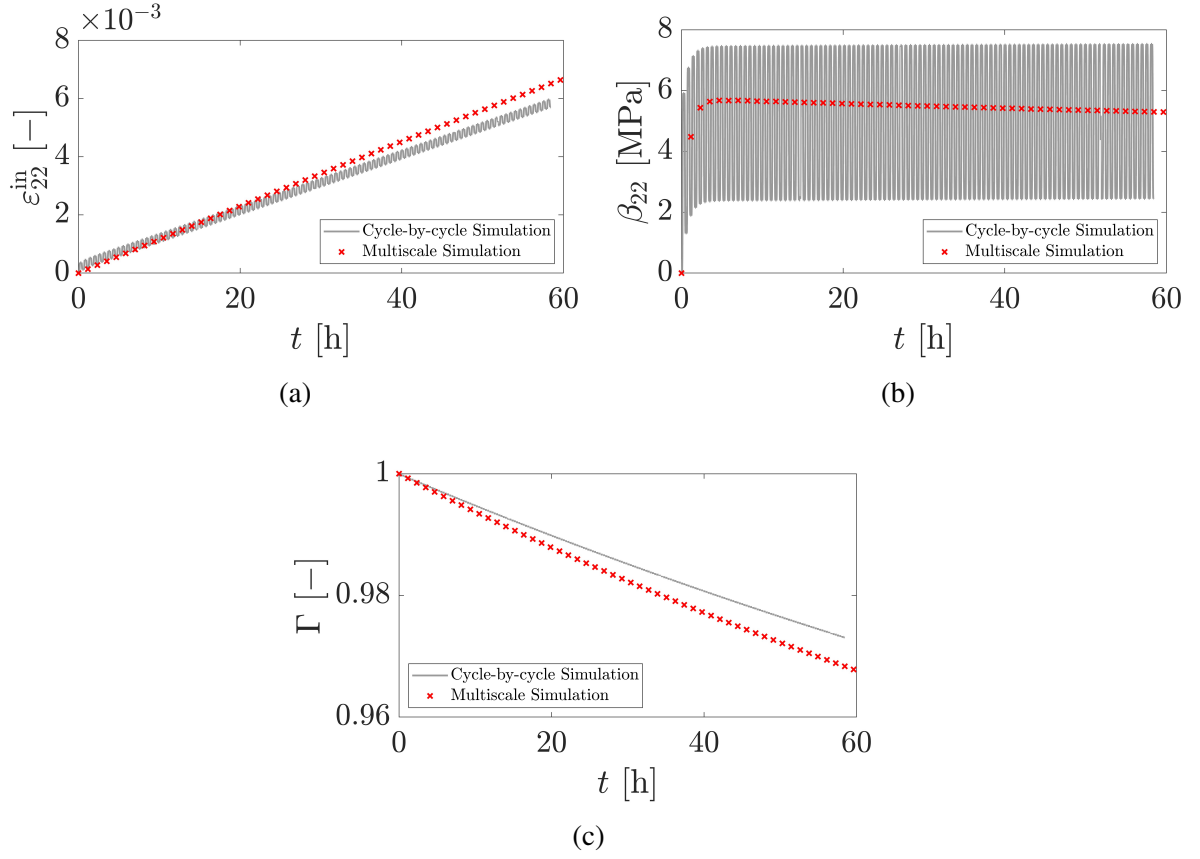


Figure 3.15: Comparison of the fully resolved internal variables and the averaged value of the elastic solution: for the inelastic strain  $\varepsilon^{\text{in}}$  (a), the backstress  $\beta$  (b) and the softening variable  $\Gamma$  (c)

Table 3.3: Comparison of the simulation times for the phase-mixture-model of the alloy X20CrMoV12-1 between the cycle-by-cycle and two-time-scale simulation

$N$	Cycle-by-cycle [s]	Multiscale [s]	Reduction [%]
$10^2$	78.54	2.12	97.29

As shown in Fig. 3.16, the stress responses exhibit good agreement between the multiscale and fully resolved simulations. The relative error decreases from 4.67% to 3.21% as the number of cycles increases, as illustrated in Fig. 3.17. This decreasing trend is consistent with findings in the literature, for instance, in [69], a continued reduction in error was observed for  $N = 300\,000$  cycles when comparing multiscale simulations with both experimental and cycle-by-cycle data. Moreover, the qualitative behavior of maintaining a nearly constant stress amplitude over a large number of cycles aligns well with experimental observations for X20CrMoV12-1 steel reported in [138]. However, it should be noted that the experimental tests in that study were performed at higher strain amplitudes, which fall outside the calibration range of the material model used here, limiting direct quantitative comparison. The comparison of the averaged internal variables with respect to the fully resolved simulation is shown in Fig. 3.18.

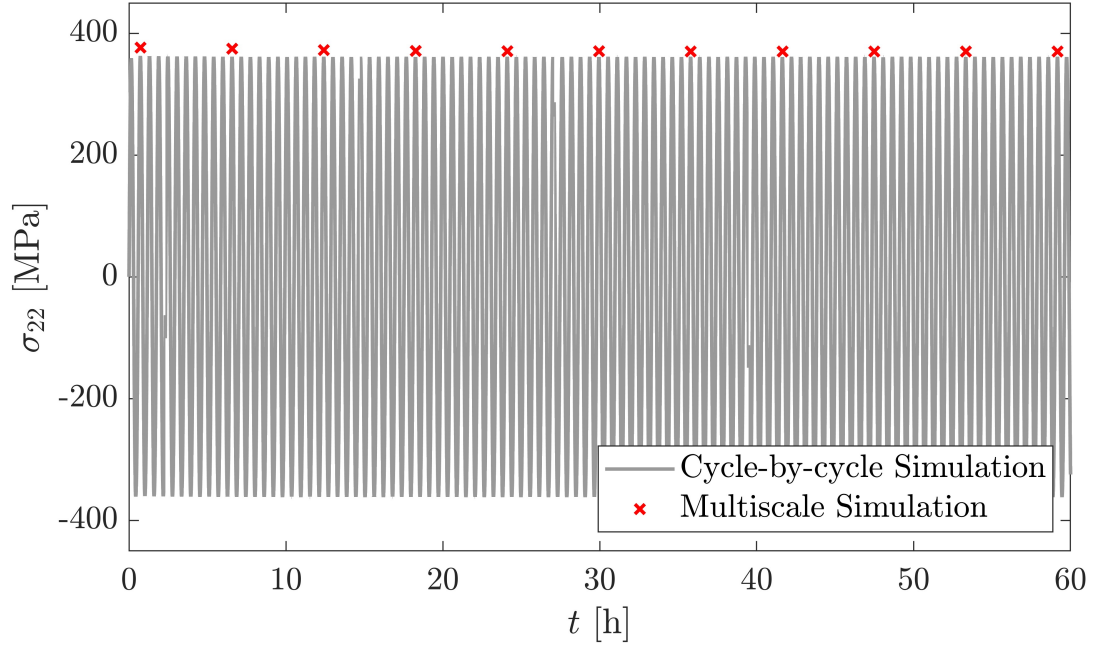


Figure 3.16: Comparison of the cycle-by-cycle simulation with the temporal multiscale algorithm for  $N = 100$  cycles

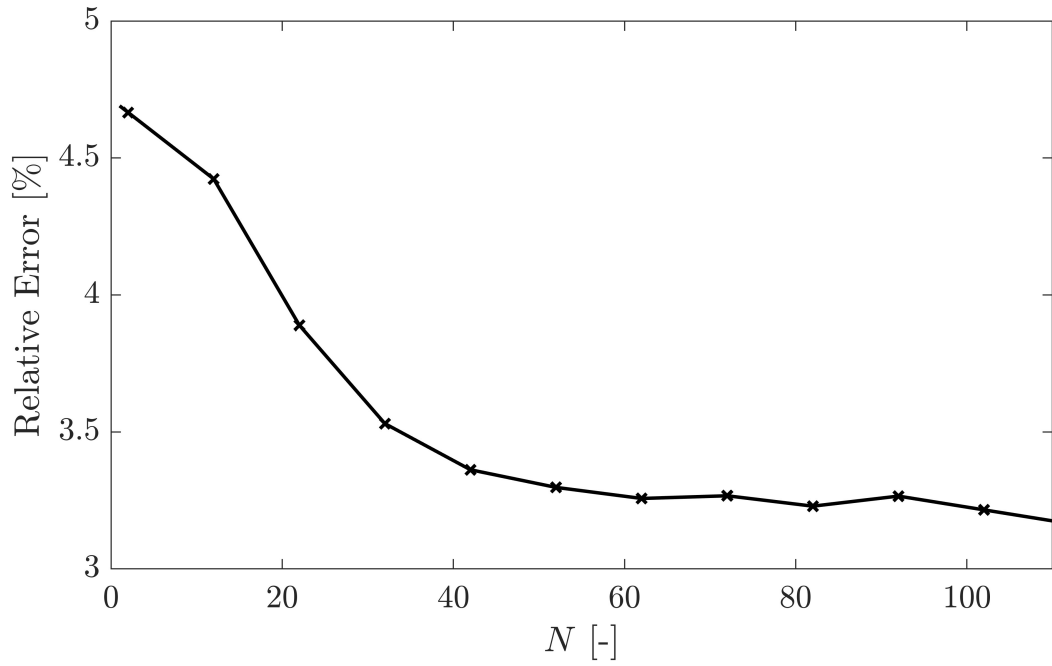


Figure 3.17: Relative error of the maximum stress values for  $N = 100$  cycles



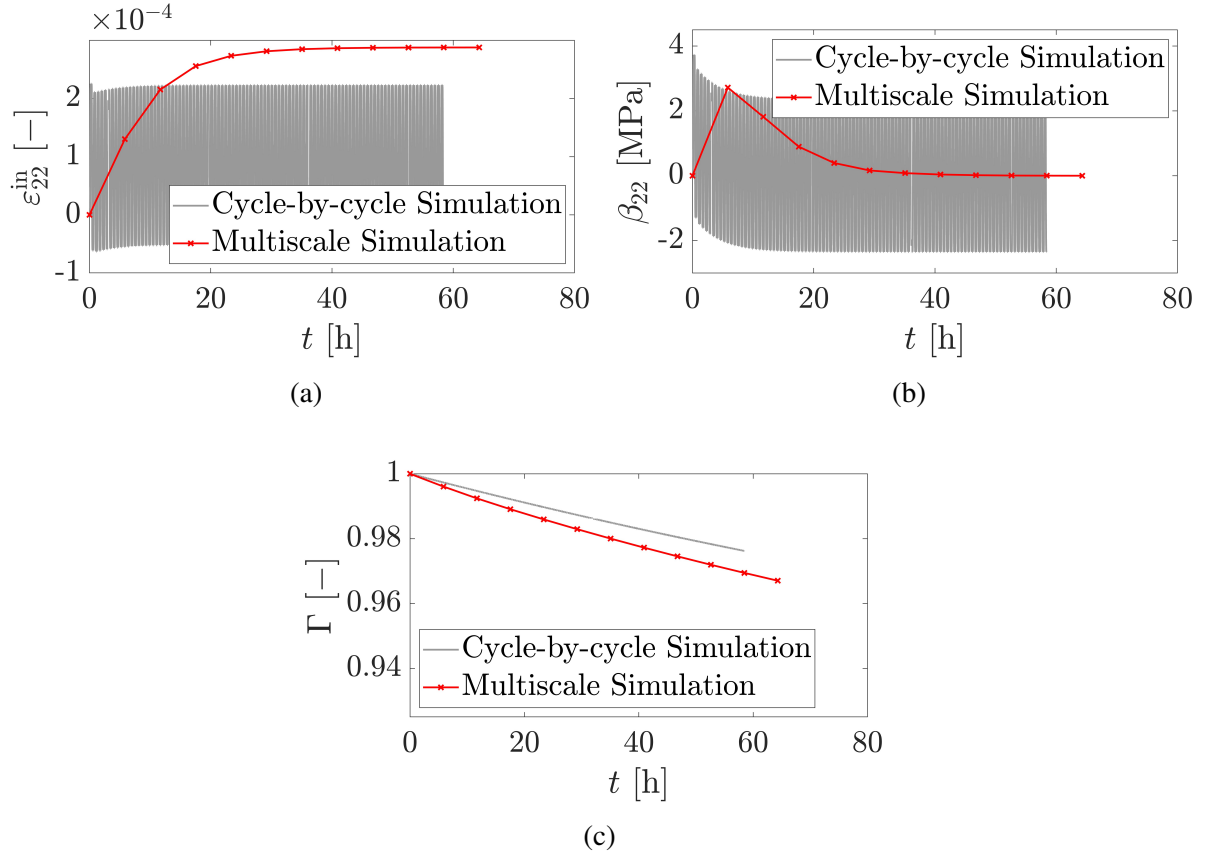


Figure 3.18: Comparison of the fully resolved internal variables and the averaged value: for the inelastic strain  $\varepsilon^{\text{in}}$  (a), the backstress  $\beta$  (b) and the softening variable  $\Gamma$  (c)

The averaged values tend to overestimate the evolution of the inelastic strain as well as the softening variable, a behavior that was already seen in the elastic solution. The previous macro and micro time step sizes were selected based on a balance between computational efficiency and numerical stability. It was identified as the step size that provided a stable solution with negligible deviation from the reference cycle-by-cycle simulation, while still offering a substantial reduction in computation time. For further validation, the macro step is decreased to enhance accuracy and examine the influence of the parameter. The results for the stress response are shown in Fig. 3.19, the averaged internal variables are illustrated in Fig. 3.20 for  $\Delta t_M = \{2, 5, 10\}$ . The results for a macro step of  $\Delta t_M = 2P$  are pictured in blue, the curve resulting from  $\Delta t_M = 5P$  is depicted in green and the simulation done with  $\Delta t_M = 10P$  is shown in red. The cycle-by-cycle simulation serves as reference and is printed in gray. The average values with decreasing  $\Delta t_M$  not only capture the trend of the internal variables but also reproduce the correct magnitude ranges, showing good qualitative agreement with the fully resolved simulation. However, a total of only  $N = 100$  simulated cycles is insufficient to fully assess the long-term behavior. For instance, the averaged backstress  $\beta$  continues to decrease and has not yet reached saturation. Therefore, a larger number of cycles should be studied to fully depict the long-term behavior.

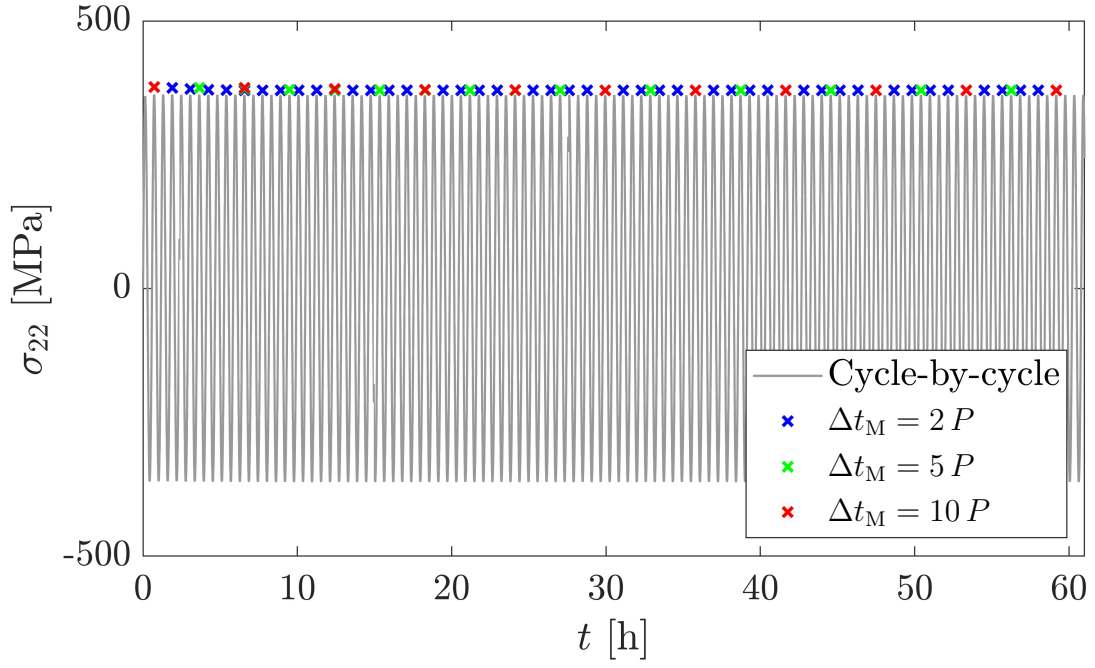


Figure 3.19: Result of the maximum stress calculated by the multiscale algorithm depending on the macro time step  $\Delta t_M$

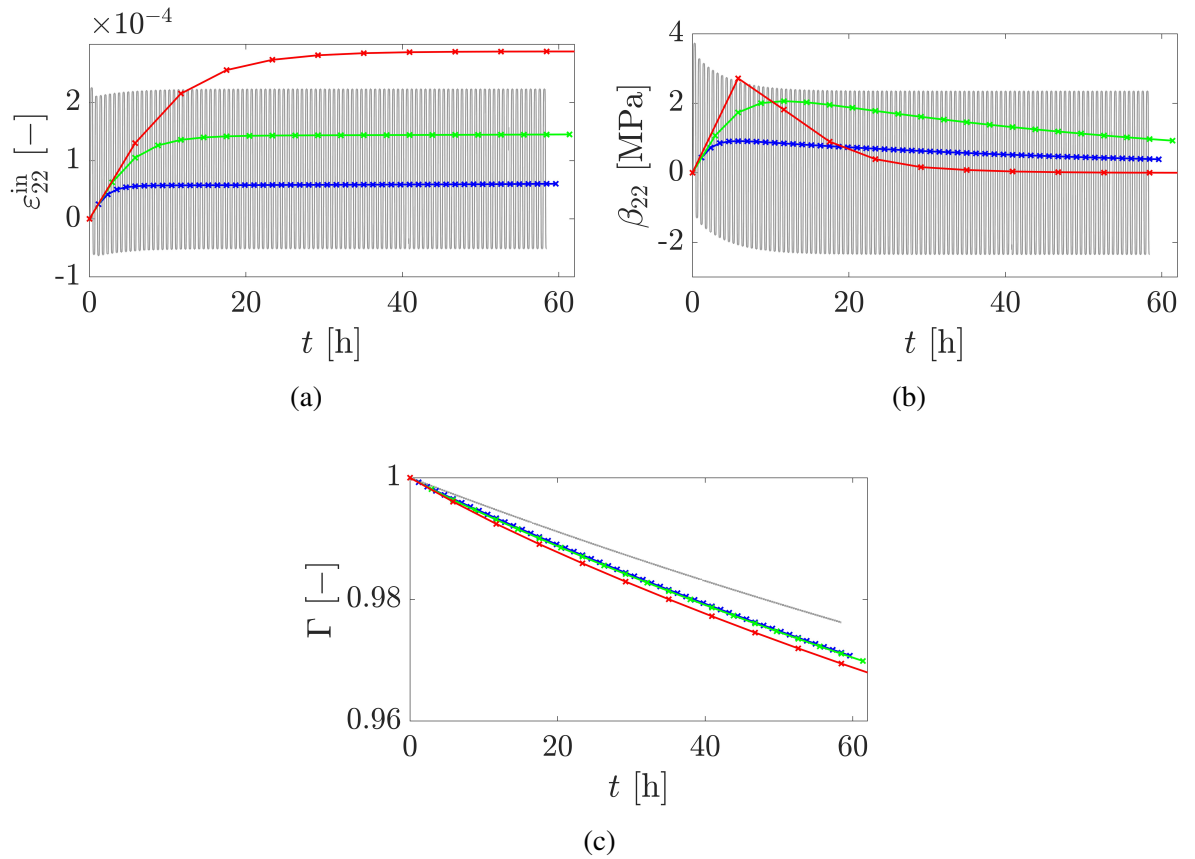


Figure 3.20: Comparison of the averaged internal variables for different  $\Delta t_M$ : the inelastic strain  $\varepsilon^{\text{in}}$  (a), the backstress  $\beta$  (b) and the softening variable  $\Gamma$  (c)

The validation confirms that the multiscale implementation reproduces the stress and in-

ternal variable evolution observed in fully resolved cycle-by-cycle simulations. Both elastic and inelastic simulations demonstrate strong agreement, and the influence of a key parameter, the macro time step  $\Delta t_M$  is systematically explored. The results verify the effectiveness of the multiscale framework in simulating long-term cyclic loading while offering substantial computational speedup.

### 3.3 Simulation of a Large Number of Cycles

For the application case considered in the work at hand, a large number of loading cycles are of interest. In this section, they are simulated with the temporal multiscale algorithm and compared to the cycle-by-cycle simulation also considering the influence of the scaling factor  $\mu$  or the macro time step  $\Delta t_M$  respectively. Their relationship is defined in Eq. (2.93) and can be reformulated as follows

$$\Delta \tau = \mu \Delta t_M. \quad (3.97)$$

Therefore, depending on the scaling parameter, the time step sizes of the two time scales vary. The variation of  $\mu$  is done based on the simulation of  $N = 100$  cycles, all of the simulations were performed using a computer with an Intel Core i7 processor (3.3 GHz) and 16 GB of random access memory. Table 3.4 demonstrates the influence of the scaling parameter  $\mu$  on both the computational cost and accuracy of the multiscale simulation, the simulation evaluated in the previous section is printed in bold.

As the value of  $\mu$  increases, the simulation time decreases significantly from 19.75 s at  $\mu = 10^{-5}$  to just 1.09 s at  $\mu = 10^{-3}$ . However, this speedup comes with a trade-off in accuracy. The relative error at the 100<sup>th</sup> cycle shows a modest increase, ranging from 3.20 % to 4.36 %. As expected, smaller values of the scaling parameter result in higher computational times but also improved accuracy. Notably, the result at  $\mu = 10^{-4}$  offers a favorable balance between efficiency and precision, yielding a simulation time of 2.12 s and a relative error of 3.21 %. Thus, selecting an appropriate scaling factor is crucial to achieving both computational efficiency and a reliable approximation of the cycle-by-cycle reference.

Since an increasing macro time step leads to a more stable simulation because the periodicity criterion with respect to the fast scale is more likely to be fulfilled, Table 3.3 is extended for larger number of cycles. For  $N = 10^3$  cycles, the fully resolved time step was chosen to be  $\Delta t = 10^{-1}$  and for the multiscale calculation, the scaling parameter was kept as  $\mu = 10^{-4}$  and the macro time step was still  $\Delta t_M = 10 P$ . Due to significantly high simulation times for the

Table 3.4: Influence of the size of the scaling factor  $\mu$  on the simulation time as well as the accuracy of results using the cycle-by-cycle simulation as reference to calculate the relative error at the 100<sup>th</sup> cycle

Scaling parameter $\mu$	Macro time step $\Delta t_M$	Simulation time [s]	Relative error [%]
$10^{-3}$	$10 P$	1.09	4.36
$10^{-4}$	$10 P$	2.12	3.21
$10^{-5}$	$10 P$	19.75	3.20

cycle-by-cycle simulation, the time for a total number of  $N = 10^6$  was extrapolated taking into account the average value per cycle based on the two simulations done and is therefore marked as an approximate value. For the two-time-scale approach, it should be noted that the chosen set of parameters could be further improved to increase the reduction in computational time.

The resulting simulation times for constant multiscale parameters are depicted in Table 3.5 including the reduction in computational cost compared to the cycle-by-cycle simulations, in agreement with values reported in the literature [69]. The results for  $N = 10^3$  cycles were again compared to the fully resolved simulation, as shown in Fig. 3.21.

Table 3.5: Comparison of the simulation times for the phase-mixture-model of the alloy X20CrMoV12-1 between the cycle-by-cycle and two-time-scale simulation

$N$	Cycle-by-cycle [s]	Multiscale [s]	Reduction [%]
$10^2$	78.54	2.12	97.29
$10^3$	234.26	18.02	92.37
$10^6$	$\approx 509\,830$	9019.21	$\approx 98.23$

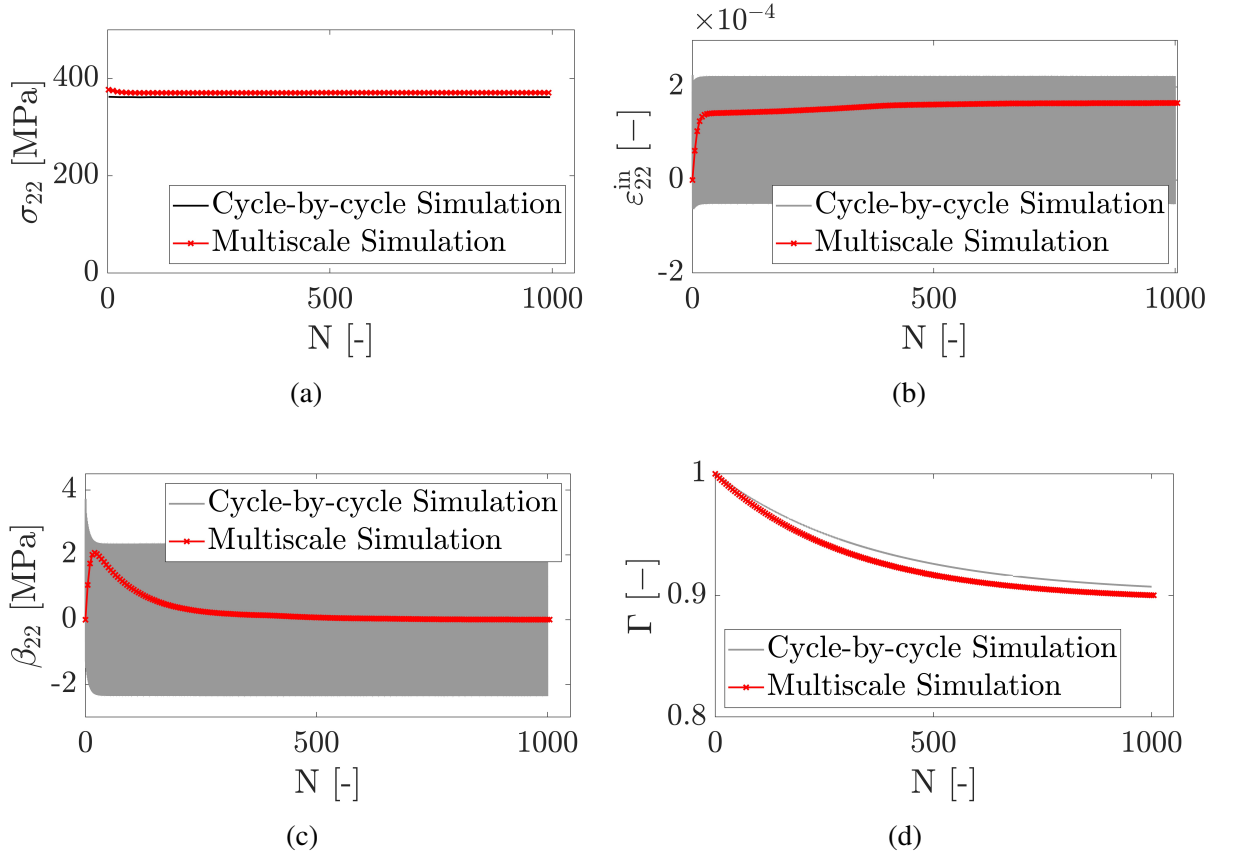


Figure 3.21: Comparison of the stress as well as the averaged internal variables for  $10^3$  cycles: the maximum stress per cycle (a), the inelastic strain  $\epsilon_{22}^{\text{in}}$  (b), the backstress  $\beta_{22}$  (c) and the softening variable  $\Gamma$  (d)

### *3 Numerical Implementation for X20CrMoV12-1*

This section demonstrated the capability of the multiscale algorithm to simulate a large number of loading cycles with high computational efficiency. By systematically varying the scaling parameter  $\mu$  and macro time step  $\Delta t_M$ , a balance between accuracy and performance was achieved. The results show that the multiscale approach maintains good agreement with fully resolved simulations while reducing computational time by more than 90%. These findings highlight the method's suitability for long-term fatigue analysis in high-temperature materials, especially where conventional approaches are prohibitively expensive.

# 4 Application to X12CrMoWVNbN10-1-1

In this Chapter, the same method is supposed to be applied to X12CrMoWVNbN10-1-1 steel. In [87], the same system of equations was solved via the finite element method using the software ABAQUS via UMAT. Additionally, the material model was implemented into the software SIEMENS NX using a neural network to recalibrate the material parameters and functions to describe the material behavior more accurately <sup>1</sup>. These results as well as experimental data generated <sup>2</sup> will serve as comparison for the validation in Subsects. 4.1.2 and 4.3 of this chapter.

## 4.1 Cycle-by-cycle Simulations

### 4.1.1 Constitutive Equations

The development and implementation of the material model for X12CrMoWVNbN10-1-1 was the main object of [87, 142]. In contrast to earlier sections where the inelastic strain was denoted as  $\epsilon^{\text{in}}$ , the focus here shifts to creep strain  $\epsilon^c$  to reflect the dominant deformation mechanism in X12CrMoWVNbN10-1-1 under high-temperature conditions. In order to formulate a suitable evolution equation for it, the time derivative of the total strain, Eq. (3.1) and the same separation ansatz as in Eq. (2.70) are applied

$$\dot{\epsilon}^c = \frac{3}{2} f_{\sigma}(\tilde{\sigma}_{\text{vM}}) f_T(T) \frac{\tilde{\sigma}'}{\tilde{\sigma}_{\text{vM}}}, \quad (4.1)$$

$$\dot{\beta} = \frac{1}{G} \frac{dG}{dT} \dot{T} \beta + A_h \left( \dot{\epsilon}^c - \frac{3}{2} \dot{\epsilon}_{\text{vM}}^c \frac{\beta}{H_{\star} \sigma_{\text{vM}}} \right) \quad (4.2)$$

with the material parameters  $A_h$  and  $H_{\star}$  where

$$\tilde{\sigma}' = \sigma' - \Gamma \beta \quad \text{and} \quad \tilde{\sigma}_{\text{vM}} = \sqrt{\frac{3}{2} \text{tr}(\tilde{\sigma}')^2} \quad (4.3)$$

still hold. The third differential equation is adapted from Subsect. 3.1.1, Eq. (3.19)

$$\dot{\Gamma} = A_S (\Gamma_{\star}(\sigma_{\text{vM}}) - \Gamma) \dot{\epsilon}^c \quad (4.4)$$

<sup>1</sup>Riepin, B. (2024). Ertüchtigung eines konstitutiven Kriechmodells für industrielle Anwendung mit Parameter-Identifizierung mithilfe von künstlichen neuronalen Netzen und Implementierung in UMAT. Masterthesis, Otto-von-Guericke-Universität, Magdeburg.

<sup>2</sup>Kostenko, Y., Almstedt, H., Scholz, A., Linn, S., Naumenko, K., Kutschke, A., Prygorniev, O. (2012). Langzeit-dehnverhalten (LCF-Ermüdung) von großen Dampfturbinenkomponenten im Hochtemperaturbereich. *Verbundprojekt COORETEC-Turbo III*.

containing  $A_S$  as a material parameter and  $\Gamma_*$  as the saturation value. For the condition of constant stress and temperature, the system of equations can be simplified<sup>1</sup>.

$$\dot{\epsilon}^c = f[\sigma(1 - H\Gamma)] f_T(T), \quad (4.5)$$

$$\dot{H} = \frac{3G}{C_h \sigma_0} \left(1 - \frac{H}{H_*}\right) \dot{\epsilon}^c, \quad H = \frac{\beta}{\sigma}, \quad (4.6)$$

$$\dot{\Gamma} = C(\Gamma_* - \Gamma) |\dot{\epsilon}^c| \quad (4.7)$$

allowing for the determination of the parameters shown when applying the stepwise procedure explained below:

- determining the stress and temperature response functions  $f_\sigma$  and  $f_T$  from the dependency of the minimum creep velocity  $\dot{\epsilon}_{\min}^c$  on stress as well as temperature
- using the primary creep regime of experimental data to find the parameter  $C_h$
- finding the values of  $A_S$  and  $\Gamma_*$  from the tertiary creep stage or data concerning long-term strength (time until fracture due to creep happens as function of the stress).

The YOUNG's modulus as well as the POISSON's ratio can be described as functions of the temperature  $T$ <sup>2</sup>

$$E = A_E + B_E T + D_E T^8, \quad (4.8)$$

$$\nu = A_\nu + B_\nu T + D_\nu T^3. \quad (4.9)$$

In literature, many stress response functions are available for describing minimum creep rates, with varying degrees of physical justification. Some overviews can be found for example in [60, 125]. One approach is the hyperbolic sine function which was also used in [47, 88]. Another approach combines diffusion and dislocation mechanisms in a series arrangement for describing the minimum creep rate across a wide range of stress levels

$$\dot{\epsilon}_{\min}^c = \dot{\epsilon}_0 \frac{\sigma}{\sigma_0} + \dot{\epsilon}_0 \left( \frac{\sigma}{\sigma_0} \right)^n \quad (4.10)$$

including  $\dot{\epsilon}_0$ ,  $\sigma_0$  and  $n$  as material parameters. In the low stress regime, the creep rate is approximated as a linear function of the applied stress which is typically associated with diffusion-controlled creep mechanisms. In the moderate stress range, the power law relationship dominates whereas at high stress levels, the power law tends to significantly underestimate the strain rate. This behavior is referred to as the 'power-law breakdown' and will therefore be omitted<sup>1</sup>. A major advantage of Eq. (4.10) is the ability to describe linear creep as well as power law creep in structural applications [112, 115]. The temperature dependency was fitted to be<sup>1</sup>

<sup>1</sup>Kostenko, Y., Almstedt, H., Scholz, A., Linn, S., Naumenko, K., Kutschke, A., Prygorniev, O. (2012). Langzeitdehnverhalten (LCF-Ermüdung) von großen Dampfturbinenkomponenten im Hochtemperaturbereich. *Verbundprojekt COORETEC-Turbo III*.

<sup>2</sup>Riepin, B. (2024). Ertüchtigung eines konstitutiven Kriechmodells für industrielle Anwendung mit Parameter-Identifizierung mithilfe von künstlichen neuronalen Netzen und Implementierung in UMAT. Masterthesis, Otto-von-Guericke-Universität, Magdeburg.

$$f_T = \left( \frac{T}{T_1} \right)^n 10^{-8} \quad (4.11)$$

with the material parameter  $T_1$  and exponent  $n$ . In order to fully describe the evolution of the creep strain, the stress response function  $f_\sigma$  in the form of

$$f_\sigma = \sinh \left( \frac{\tilde{\sigma}_{vM}}{\sigma_1} \right) + b \left[ \sinh \left( \frac{\tilde{\sigma}_{vM}}{\sigma_2} \right) \right]^m \quad (4.12)$$

was introduced applying the three parameters  $\sigma_1$ ,  $\sigma_2$  and  $m$ . For the hardening variable  $H$  the condition  $0 \leq H \leq H_\star$  holds, with  $H_\star$  the saturation value being a constant according to<sup>1</sup>

$$H_\star(\sigma) = \text{const.} \quad (4.13)$$

High temperature steels show a distinct tertiary creep behavior which is also proven by experimental data, e.g. in [129]. In the regime of elevated stress levels, the failure is ductile and creep ends with necking of the specimen as a result of the substantial deformation. For a moderate stress level and a longer test duration, the failure mode is also generally ductile, whereby the slope of the long-term strength curve changes significantly. Here, the creep process is accompanied by numerous microstructural changes which lead to a decrease in creep strength. The two most important mechanisms are the growth of subgrains and the coarsening of carbide precipitates [82, 129]. In the transition region, the formation and progression of cavities and microcrack formation have a significant influence on the creep behavior [97]. The slope of the long-term strength curve is significantly lower compared to the ductile region. A kinematic model to describe ductile fracture was introduced in [72] but examinations of high temperature steels revealed that it overestimated the remaining life time, therefore, structural changes, e.g. coarsening of the sub-grain boundaries must be taken into account. One possibility to do so is by applying the softening variable  $\Gamma$ , see Eq. (4.4). The saturation values for the backstress as well as the softening variable yield

$$\beta_\star = H_\star \sigma_{vM} \quad (4.14)$$

and

$$\Gamma_\star = \frac{\left( 1 - \frac{A_h}{A_S H_\star \sigma_{vM}} \right) + \left| 1 - \frac{A_h D}{A_S H_\star \sigma_{vM}} \right|}{2}. \quad (4.15)$$

<sup>1</sup>Riepin, B. (2024). Ertüchtigung eines konstitutiven Kriechmodells für industrielle Anwendung mit Parameter-Identifizierung mithilfe von künstlichen neuronalen Netzen und Implementierung in UMAT. Masterthesis, Otto-von-Guericke-Universität, Magdeburg.

<sup>2</sup>Kostenko, Y., Almstedt, H., Scholz, A., Linn, S., Naumenko, K., Kutschke, A., Prygorniev, O. (2012). Langzeit-dehnverhalten (LCF-Ermüdung) von großen Dampfturbinenkomponenten im Hochtemperaturbereich. *Verbundprojekt COORETEC-Turbo III*.



### 4.1.2 Implementation

The constitutive equations of the previous section were also implemented as the fully resolved problem in a Python code to serve as a basis for the application of the two-time-scale approach. The corresponding FEM simulations were done via an explicit UMAT using the software SIEMENS NX<sup>1</sup> which now serve as the comparison for the validation of the new implementation. Additionally, the experiments performed in the project<sup>1</sup> are employed to prove the correctness of the new model. In the work at hand, the EULER forward method was used, cf. Subsect. 2.4.1. Validation was conducted following the same strategy as in Subsect. 3.1.2, enabling consistent comparison.

The EULER forward method is generally described through

$$\mathbf{Y}_{n+1} = \mathbf{Y}_n + \Delta t \mathbf{f}(t_n, \mathbf{Y}_n) \quad (4.16)$$

for a tensorial variable  $\mathbf{Y}$ . The update to get the solution at time  $t_{n+1}$  with a prescribed  $\Delta t$  is calculated according to the following scheme

$$\Delta \mathbf{Y} = \Delta t \dot{\mathbf{Y}}(t_n) \quad (4.17)$$

resulting in the following equations

$$\boldsymbol{\varepsilon}_{n+1} = \boldsymbol{\varepsilon}_n + \Delta t \dot{\boldsymbol{\varepsilon}}_n, \quad (4.18)$$

$$\boldsymbol{\varepsilon}_{n+1}^c = \boldsymbol{\varepsilon}_n^c + \Delta t \dot{\boldsymbol{\varepsilon}}_n^c, \quad (4.19)$$

$$\boldsymbol{\beta}_{n+1} = \boldsymbol{\beta}_n + \Delta t \dot{\boldsymbol{\beta}}_n, \quad (4.20)$$

$$\Gamma_{n+1} = \Gamma_n + \Delta t \dot{\Gamma}_n, \quad (4.21)$$

$$T_{n+1} = T_n + \Delta t \dot{T}_n, \quad (4.22)$$

where the derivatives with respect to time  $\dot{\square}_n$  are directly evaluated. The stress is then updated using the three dimensional formulation of HOOKE's law

$$\boldsymbol{\sigma}_{n+1} = \boldsymbol{\mathcal{C}} : \boldsymbol{\varepsilon}_n^{\text{el}} + d\boldsymbol{\mathcal{C}} : \boldsymbol{\varepsilon}_{0n}^{\text{el}} \quad (4.23)$$

with the stiffness tensor of fourth rank  $\boldsymbol{\mathcal{C}}$  and the elastic strain  $\boldsymbol{\varepsilon}^{\text{el}}$ . The second term accounts for temperature changes with respect to time, which will be needed to describe the stress for the TMF test. The stiffness tensor and the elastic strain are calculated according to the following equations

$$\boldsymbol{\mathcal{C}} = \lambda \mathbf{I} \otimes \mathbf{I} + 2\mu \boldsymbol{\mathcal{I}}, \quad \boldsymbol{\mathcal{I}} = \mathbf{e}_i \otimes \mathbf{e}_j \otimes \mathbf{e}_j \otimes \mathbf{e}_i \quad (4.24)$$

---

<sup>1</sup>Kostenko, Y., Almstedt, H., Scholz, A., Linn, S., Naumenko, K., Kutschke, A., Prygorniev, O. (2012). Langzeitdehnverhalten (LCF-Ermüdung) von großen Dampfturbinenkomponenten im Hochtemperaturbereich. *Verbundprojekt COORETEC-Turbo III*.

with  $\mathcal{I}$  the unit tensor of fourth rank and

$$\varepsilon_n^{\text{el}} = \varepsilon_n - \varepsilon_n^{\text{c}} \quad (4.25)$$

as well as

$$\varepsilon_{0n}^{\text{el}} = \varepsilon_n - \varepsilon_{0n}^{\text{c}}. \quad (4.26)$$

$\varepsilon_{0n}^{\text{c}}$  denoting the creep strain at the beginning of the time increment whereas  $\varepsilon_n^{\text{c}}$  describes the already updated creep strain.

### 4.1.3 Validation

#### 4.1.3.1 Low Cycle Fatigue Tests

The same LCF profile as in Subsect. 3.1.3 is used to validate the new model. At high temperatures, both creep and fatigue play a significant role in the material behavior. Although the model does not account for fatigue damage, the creep process can still be observed as well as the model's ability to handle variable loading conditions. The first LCF test is carried out at  $T = 600^\circ\text{C}$  with a constant strain rate of  $\dot{\varepsilon} = 0.046 \frac{\%}{\text{min}}$ . In Fig. 4.1 (a), the result is shown, Fig. 4.1 (b) depicts the model's behavior with respect to the experimental data available for X12CrMoWVNbN10-1-1<sup>1</sup>.

The simulation reveals that the stress peaks are slightly overestimated by the model compared to the experiment. Nevertheless, the trends, the increase in stress amplitude in the tensile region and the decrease in stress amplitude in the compressive region are accurately captured. Additionally, a second LCF profile with the constant strain rate of  $\dot{\varepsilon} = 0.06 \frac{\%}{\text{min}}$  is simulated, again at a temperature of  $T = 600^\circ\text{C}$ . The result of the first cycle and the comparison to the SIEMENS NX UMAT is shown in Fig. 4.2.

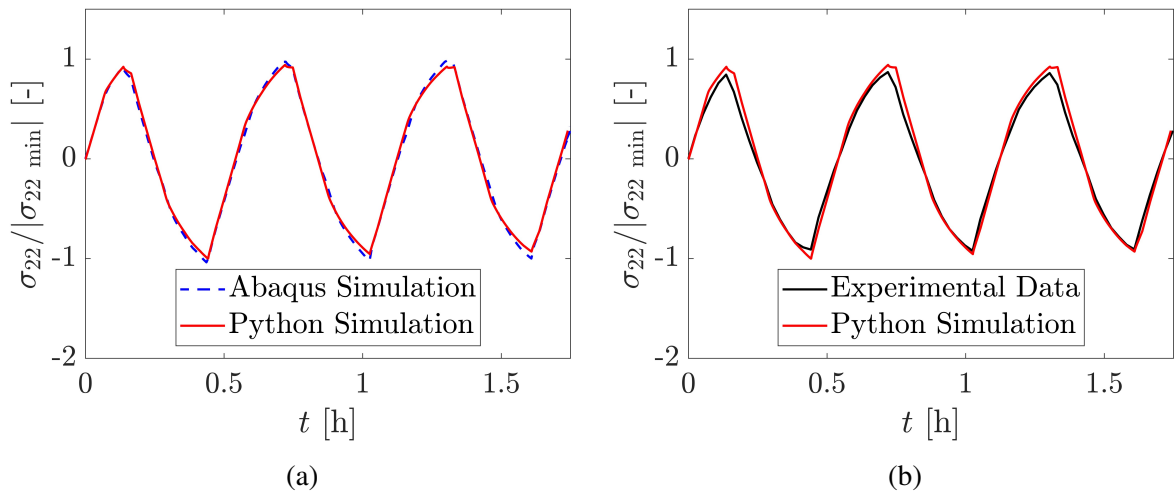


Figure 4.1: Simulation results of three cycles in the LCF test: in comparison with the ABAQUS result (a) and to the experimental results (b)

<sup>1</sup>Kostenko, Y., Almstedt, H., Scholz, A., Linn, S., Naumenko, K., Kutschke, A., Prygorniev, O. (2012). Langzeitdehnverhalten (LCF-Ermüdung) von großen Dampfturbinenkomponenten im Hochtemperaturbereich. Verbundprojekt COORETEC-Turbo III.

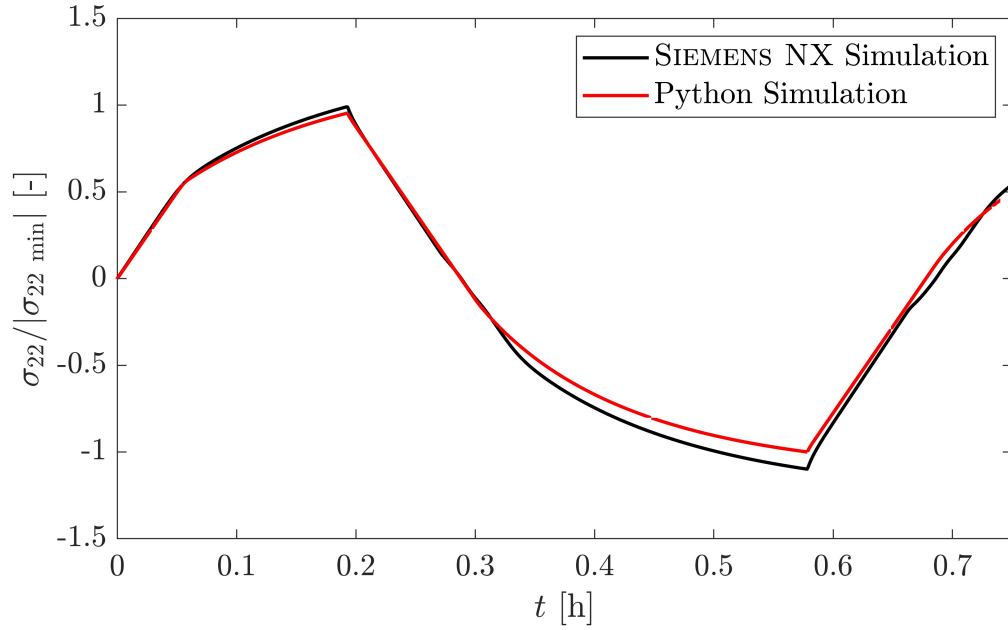


Figure 4.2: Comparison of the simulation results regarding one LCF cycle with a constant strain rate of  $\dot{\varepsilon} = 0.06 \frac{\%}{\text{min}}$

Qualitatively, the behavior completely illustrates the material response described in Sect. 2.1 to a constant strain rate loading profile without dwell times.

In the next step, several cycles of the same loading profile are simulated and again compared with the FEM results as well as the experimental data. The simulation slightly over-estimated the peak stresses but nevertheless, the model captures the stress behavior correctly. Moreover, the trend of decreasing tensile stress amplitudes is accurately represented.

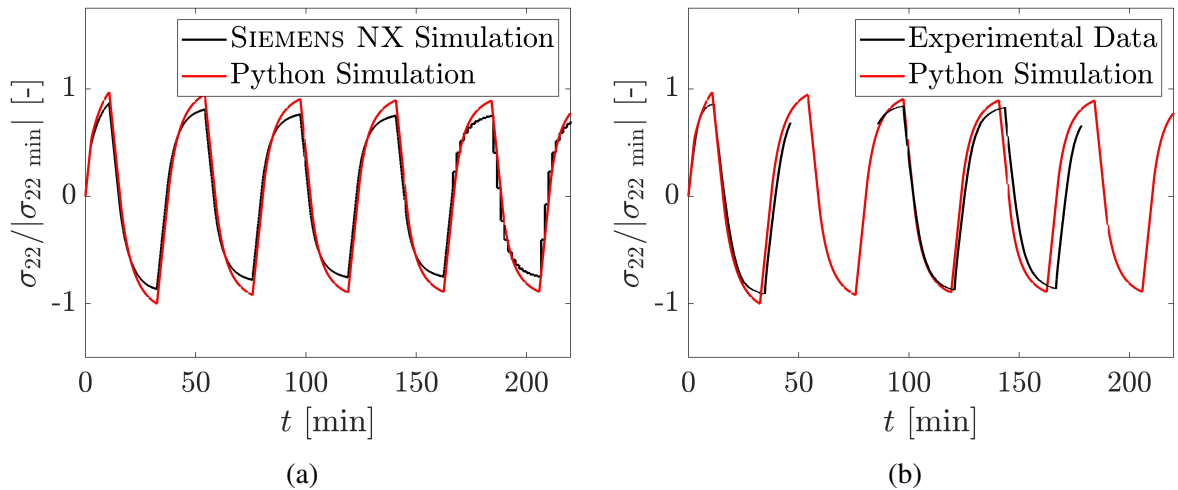


Figure 4.3: Simulation of several cycles in the LCF test: in comparison with the SIEMENS NX result (a) and with the experimental data<sup>1</sup> (b)

<sup>1</sup>Kostenko, Y., Almstedt, H., Scholz, A., Linn, S., Naumenko, K., Kutschke, A., Prygorniev, O. (2012). Langzeitdehnverhalten (LCF-Ermüdung) von großen Dampfturbinenkomponenten im Hochtemperaturbereich. *Verbundprojekt COORETEC-Turbo III*.

The LCF simulations demonstrate that the implemented model is capable of reproducing key features of the material behavior for X12CrMoWVNbN10-1-1, including stress relaxation and amplitude evolution. While minor discrepancies in peak stress levels exist, the trends observed in both FEM and experimental data are well captured, validating the model's suitability for cyclic loading conditions within the calibrated range.

#### 4.1.3.2 Thermo-Mechanical Fatigue Test

The newly developed material model must also account for temperature changes with respect to time. To validate the model, the loading profile<sup>1</sup> depicted in Fig. 4.4 consisting of a cold start, four hot starts and a warm start was applied. The result compared to the SIEMENS NX simulation and the experimental data is shown in Fig. 4.5.

The solution depicted at the bottom illustrates the results of the recalculation of the experiment. The TMF test strain loading profile also includes dwell times, e.g. therefore a relaxation curve (cf. Chapt. 2, Sect. 2.1) is expected. It is evident that the model shows the expected response which aligns well with the experimental data<sup>1</sup>. The simulation slightly underestimates the highest compressive stresses (the first and sixth stress peak). This is due to excessively high strain amplitudes, which are significantly outside the identification range<sup>1</sup>. Overall, the Python simulation agrees well with the FEM results and is therefore validated. For the sake of completeness, the evolution of the internal variables is also shown in Fig. 4.6.

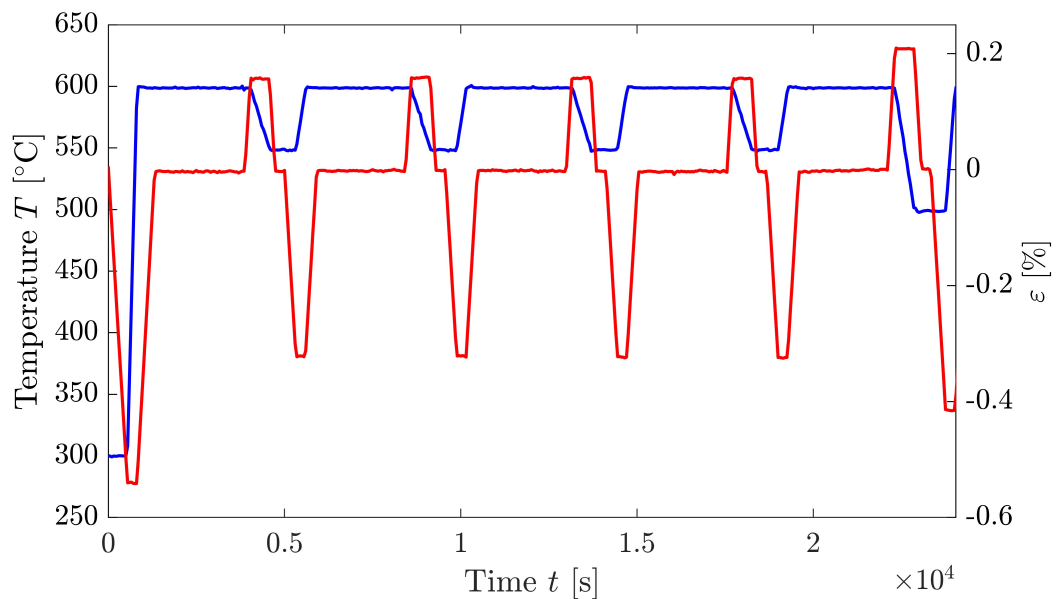


Figure 4.4: Simulated service-type loading profile of a power plant component, including cold, warm as well as hot starts [87]

<sup>1</sup>Kostenko, Y., Almstedt, H., Scholz, A., Linn, S., Naumenko, K., Kutschke, A., Prygorniev, O. (2012). Langzeitdehnverhalten (LCF-Ermüdung) von großen Dampfturbinenkomponenten im Hochtemperaturbereich. *Verbundprojekt COORETEC-Turbo III*.

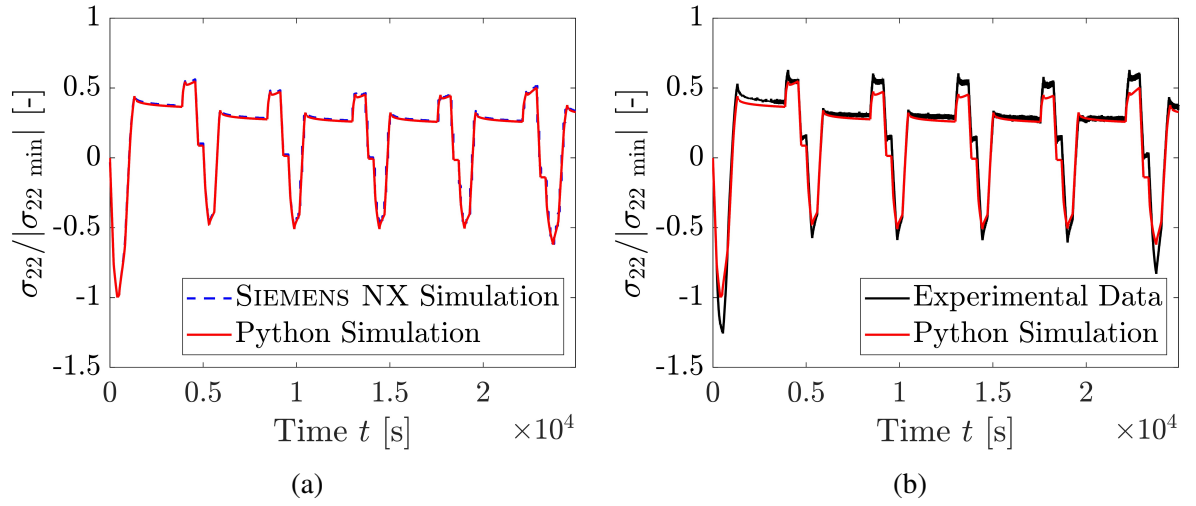


Figure 4.5: TMF test: comparison between the stress response and the FEM solution (a) and the resulting material response from experimental data (b)

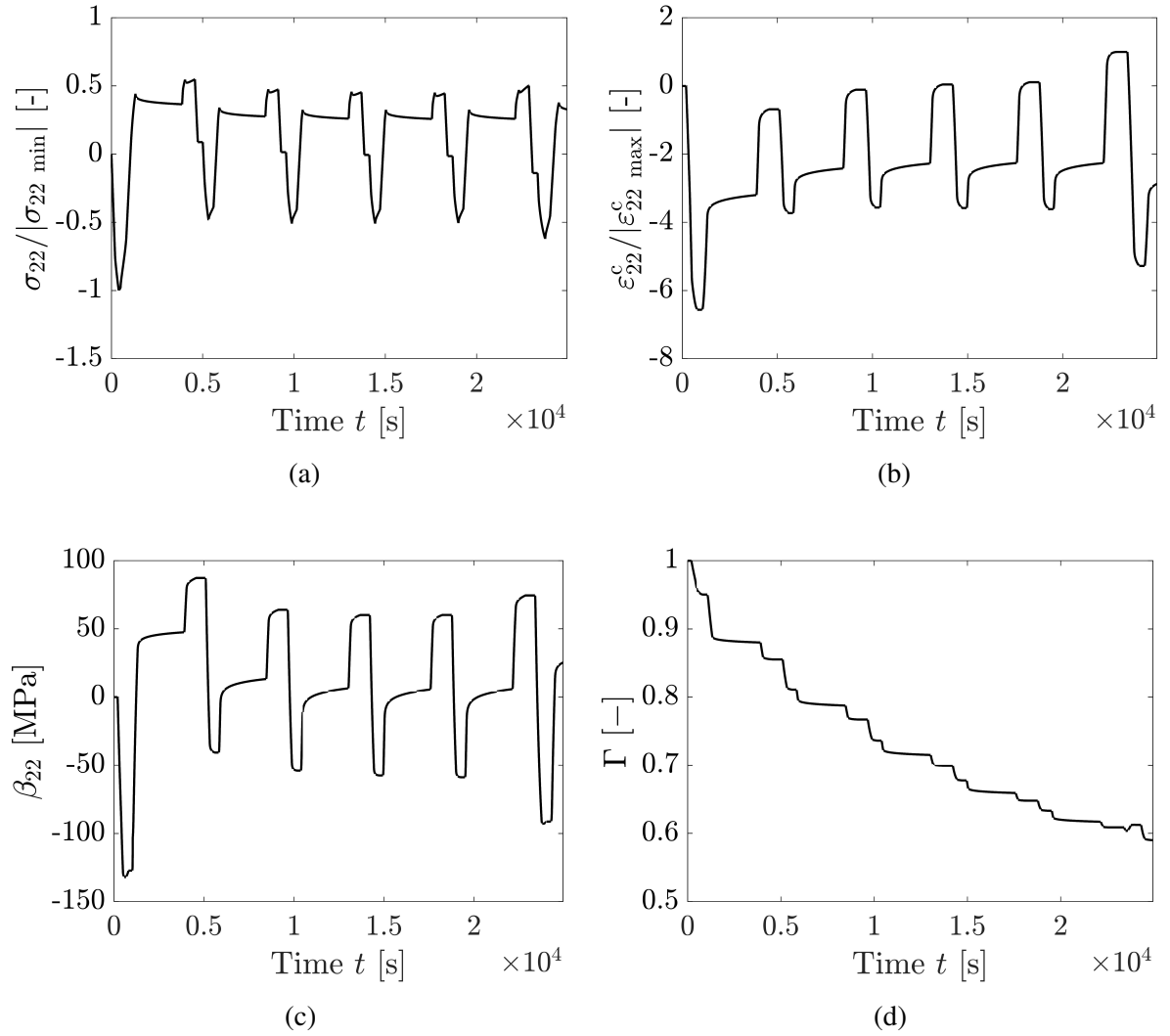


Figure 4.6: Results of the TMF profile: the stress (a) and the internal variables namely the inelastic strain  $\varepsilon_{22}^c$  (b), the backstress  $\beta_{22}$  (c) and the softening variable  $\Gamma$  (d)

The TMF validation confirms that the model successfully accounts for both mechanical and thermal loading variations, including complex service-type conditions with dwell times. The predicted stress-strain response closely aligns with FEM simulations and experimental observations. Minor underestimations at high strain amplitudes are attributed to loading scenarios outside the model's identification range. The internal variables evolve in a physically plausible manner, further supporting the validity of the constitutive model for coupled thermomechanical applications. Additionally, the validation results for both X20CrMoV12-1 and X12CrMoWVNbN10-1-1 (Subsects. 3.1.3 and 4.1.3) indicate a consistent softening behavior under cyclic loading, which is only partially captured by the current constitutive model. This limitation suggests that the evolution equations require refinement for applications involving long-term cyclic loading. The development of an improved material model addressing this limitation is presented in Chapt. 5.

## 4.2 Application of the Two-Time-Scale Approach

This section only summarizes the constitutive equations with respect to the high temperature steel X12CrMoWVNbN10-1-1 since the detailed derivation has been explained in Subsect. 3.2.1.

The  $\mu^{(0)}$ -order problem which is then implemented yields

$$\frac{3}{2} f_{\sigma}(\tilde{\sigma}_{vM}) f_T(T) \frac{\tilde{\sigma}'}{\tilde{\sigma}_{vM}} = \left( \frac{\partial \epsilon^{c(0)}}{\partial t_M} + \frac{\partial \epsilon^{c(1)}}{\partial \tau} \right), \quad (4.27)$$

$$\frac{1}{G} \frac{dG}{dT} \dot{T} \beta + A_h \left( \dot{\epsilon}^c - \frac{3}{2} \dot{\epsilon}_{vM}^c \frac{\beta}{H_{\star} \sigma_{vM}} \right) = \left( \frac{\partial \beta^{(0)}}{\partial t_M} + \frac{\partial \beta^{(1)}}{\partial \tau} \right), \quad (4.28)$$

$$A_S (\Gamma_{\star}(\sigma_{vM}) - \Gamma) \dot{\epsilon}_{vM}^c = \left( \frac{\partial \Gamma^{(0)}}{\partial t_M} + \frac{\partial \Gamma^{(1)}}{\partial \tau} \right). \quad (4.29)$$

An important methodological adaptation is made concerning the treatment of the creep strain rate  $\dot{\epsilon}^c$  and the backstress  $\beta$ . Although they are formally associated with the slow time scale in classical asymptotic analysis, their observed oscillatory behavior under cyclic loading necessitates their inclusion on the microchronological time scale. Rather than introducing a separate scaling parameter as discussed in Subsect. 3.2.3, these variables are now explicitly considered on both, the fast and the slow time scales. This dual-scale representation acknowledges that certain internal variables exhibit both rapid fluctuations within each loading cycle and gradual evolution over many cycles [124]. Therefore, they do not exhibit a clear separation from the fast-scale dynamics so that

$$\epsilon^c = \langle \epsilon^c \rangle + \epsilon^c(\tau), \quad (4.30)$$

$$\beta = \langle \beta \rangle + \beta(\tau). \quad (4.31)$$

Unlike the softening parameter  $\Gamma$ , which evolves predominantly on the slow scale,  $\dot{\epsilon}^c$  and  $\beta$  fluctuate significantly due to their direct coupling with the cyclic stress response. The modeling choice improves robustness, particularly in the early transients or when simulating a limited number of cycles. For the softening, resulting from the  $\mu^{(-1)}$ -order problem,  $\Gamma^{(0)}$  is again only

depending on the macro time, so the micro part  $\frac{\partial \square^{(1)}}{\partial \tau}$  of the evolution vanishes leading to

$$\Gamma^{(0)}(t_M, \tau) = \Gamma^{(0)}(t_M). \quad (4.32)$$

### 4.2.1 Macrochronological Problem

This section only summarizes the slow scale constitutive equations for the steel X12CrMoWVNbN10-1-1 since the detailed derivation was already done in 3.2.1.1 and is carried out analogously here. The three internal variables  $\boldsymbol{\varepsilon}^c$ ,  $\boldsymbol{\beta}$  and  $\Gamma$  are averaged with respect to the fast scale using the averaging operator  $\mathcal{M}$ .

$$\left\langle \frac{d\boldsymbol{\varepsilon}^c(t_M)}{dt_M} \right\rangle = \mathcal{M} \left( \frac{3}{2} f_\sigma(\tilde{\sigma}_{vM}(\tau)) f_T(T(t_M)) \frac{\tilde{\boldsymbol{\sigma}}'(\tau)}{\sigma_{vM}(\tau)} \right), \quad (4.33)$$

$$\begin{aligned} \left\langle \frac{d\boldsymbol{\beta}(t_M)}{dt_M} \right\rangle &= \mathcal{M} \left( \frac{1}{G(T)} \frac{dG(T)}{dT} \frac{dT(t_M)}{dt_M} \langle \boldsymbol{\beta}(t_M) \rangle \right) \\ &+ \mathcal{M} \left( A_h \left[ \frac{d\langle \boldsymbol{\varepsilon}^c(t_M) \rangle}{dt_M} - \frac{3}{2} \frac{\dot{\boldsymbol{\varepsilon}}_{vM}^c(t_M)}{H_\star \sigma_{vM}} \langle \boldsymbol{\beta}(t_M) \rangle \right] \right), \end{aligned} \quad (4.34)$$

$$\left\langle \frac{d\Gamma(t_M)}{dt_M} \right\rangle = \mathcal{M} (A_S (\Gamma^*(\sigma_{vM}(\tau)) - \langle \Gamma(t_M) \rangle) \dot{\boldsymbol{\varepsilon}}_{vM}^c(t_M)). \quad (4.35)$$

### 4.2.2 Microchronological Problem

The fast scale  $\mathbf{v}(\tau)$  in dependency of the slow scale is expressed as

$$\frac{d\mathbf{v}_{\langle \mathbf{U}(t_M) \rangle}(\tau)}{d\tau} = g(\langle \mathbf{U}(t_M) \rangle, \mathbf{v}_{\langle \mathbf{U}(t_M) \rangle}(\tau)), \quad \mathbf{v}_{\langle \mathbf{U}(t_M) \rangle}(t_n + P) = \mathbf{v}_{\langle \mathbf{U}(t_M) \rangle}(t_n), \quad (4.36)$$

$$\frac{d\boldsymbol{\varepsilon}_{\langle \mathbf{U}(\tau) \rangle}^c(\tau)}{d\tau} = \frac{3}{2} f_\sigma(\tilde{\sigma}_{vM}(\tau)) f_T(T(\tau)) \frac{\tilde{\boldsymbol{\sigma}}'(\tau)}{\sigma_{vM}(\tau)}, \quad (4.37)$$

$$\frac{d\boldsymbol{\beta}_{\langle \mathbf{U}(t_M) \rangle}(\tau)}{d\tau} = \frac{1}{G(T)} \frac{dG(T)}{dT} \frac{dT(\tau)}{d\tau} \boldsymbol{\beta}(\tau) + A_h \left[ \frac{d\boldsymbol{\varepsilon}^c(\tau)}{d\tau} - \frac{3}{2} \frac{\dot{\boldsymbol{\varepsilon}}_{vM}^c(\tau)}{H_\star \sigma_{vM}} \boldsymbol{\beta}(\tau) \right], \quad (4.38)$$

which for  $T = \text{const.}$  leads to a simplified time derivative of the three dimensional elastic law

$$\frac{d\boldsymbol{\sigma}_{\langle \mathbf{U}(t_M) \rangle}(\tau)}{d\tau} = \boldsymbol{\mathcal{C}} : \left( \frac{d(\boldsymbol{\varepsilon}(\tau) - \boldsymbol{\varepsilon}^c(\tau))}{d\tau} - \frac{d\langle \boldsymbol{\varepsilon}^c(t_M) \rangle}{dt_M} \right). \quad (4.39)$$

The implementation of the material model with respect to X12CrMoWVNbN10-1-1 steel followed the exact same logic as explained in Subsect. 3.2.2.

### 4.3 Validation

To validate the implementation of the multiscale material model, 100 cycles of the LCF test with the strain rate of  $\dot{\varepsilon} = 0.06 \frac{\%}{\text{min}}$  were simulated at a temperature of  $T = 600^\circ\text{C}$ . For the two-time-scale approach, the experimental input is fitted with the periodic function in Eq. (4.40)

$$y_1(x) = s_1 (\sin(s_2 x)). \quad (4.40)$$

The coefficients and the RSME as a measure of accuracy were taken from Table 4.1, Fig. 4.7 shows the periodic function compared to the experimental input data <sup>1</sup>.

For this LCF loading profile, the cycle-by-cycle simulation is compared to the multiscale solution. The resulting stress response is shown in Fig. 4.8 with respect to the following parameter (adopted from Subsect. 3.2.3) in analogy to the input time unit

$$\Delta t = 10^{-2} \text{ min} \quad (4.41)$$

Table 4.1: Coefficients and root mean square error of the function Eq. (4.40)

Function	RMSE	Coefficients	
$y_1$	$1.08 \times 10^{-6}$	$s_1 = 0.0065$	$s_2 = 0.1450$

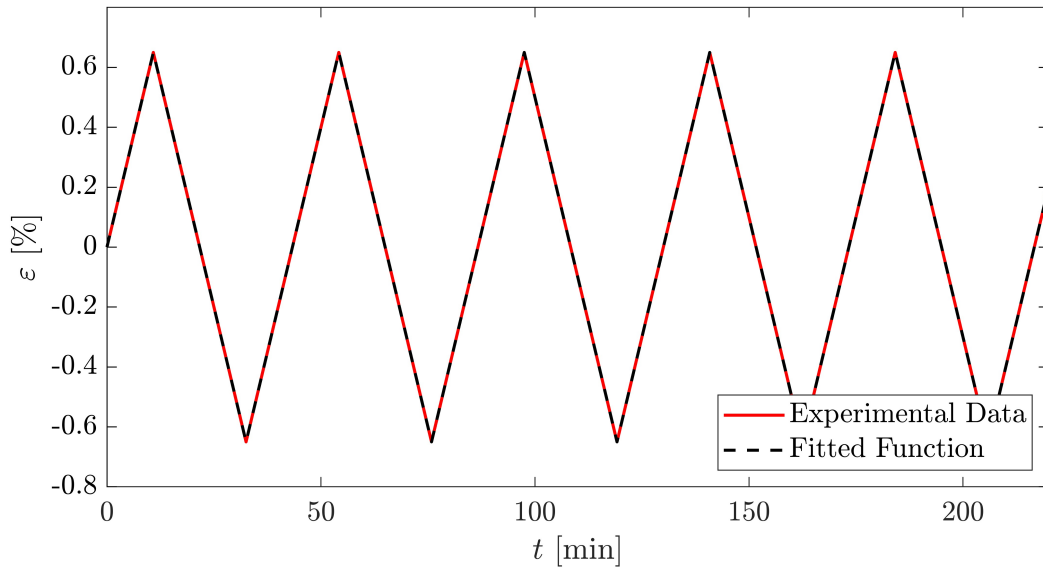


Figure 4.7: Fitting result of the experimental strain input

<sup>1</sup>Kostenko, Y., Almstedt, H., Scholz, A., Linn, S., Naumenko, K., Kutschke, A., Prygorniev, O. (2012). Langzeitdehnverhalten (LCF-Ermüdung) von großen Dampfturbinenkomponenten im Hochtemperaturbereich. *Verbundprojekt COORETEC-Turbo III*.



for the fully resolved problem and for the temporal homogenization method, the same time steps were chosen according to Subsect. 3.2.2

$$\Delta t_M = 10 P, \quad \Delta \tau = P \times 10^{-3} \quad (4.42)$$

with

$$\mu = 10^{-4} \quad (4.43)$$

respectively.

For the internal variables  $\varepsilon_{22}^c$  and  $\beta_{22}$ , both the fast-scale solutions and their macrochronological averages are shown in Fig. 4.9. The figure also includes the evolution of the averaged softening parameter  $\Gamma$ , which evolves on the slow time scale. The results demonstrate a strong agreement between the peak values of  $\varepsilon_{22}^c$  and  $\beta_{22}$  from the fast scale, indicating that the local response is captured consistently within the micro cycles. Since such a LCF profile typically results in a hysteresis, cf. Sect. 2.1, the behavior is illustrated for the first and 100<sup>th</sup> cycle in Fig. 4.10. These hysteresis loops reflect the characteristic stress-strain response under cyclic loading, where inelastic effects such as plastic deformation and material softening accumulate over time. Comparing the early and late cycle responses highlights the evolution of the material behavior, including any cyclic hardening or softening phenomena that emerge throughout the simulation. In Table 4.2, the computational times taken for the profile containing 100 loading cycles are summarized. This consistency across scales highlights the effectiveness of the two-scale formulation in capturing the behavior on the different scales, while significantly reducing computational effort compared to fully resolved simulations.

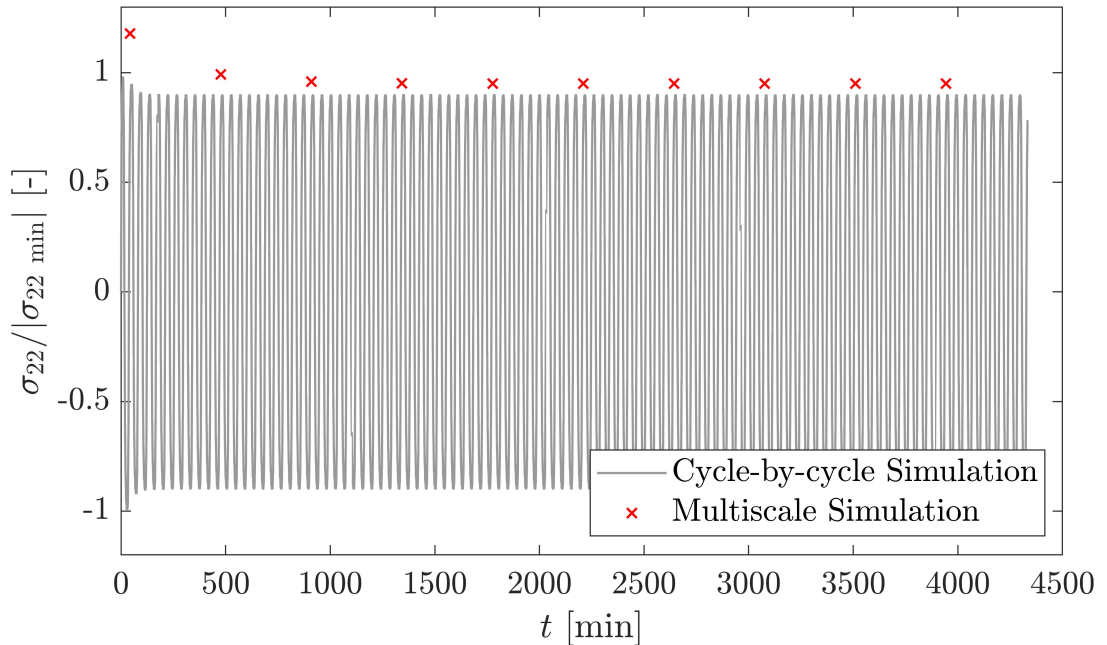


Figure 4.8: Comparison of the cycle-by-cycle simulation with the two-time-scale approach for  $N = 100$  cycles of the LCF profile with a constant strain rate of  $\dot{\varepsilon} = 0.06 \frac{\%}{\text{min}}$

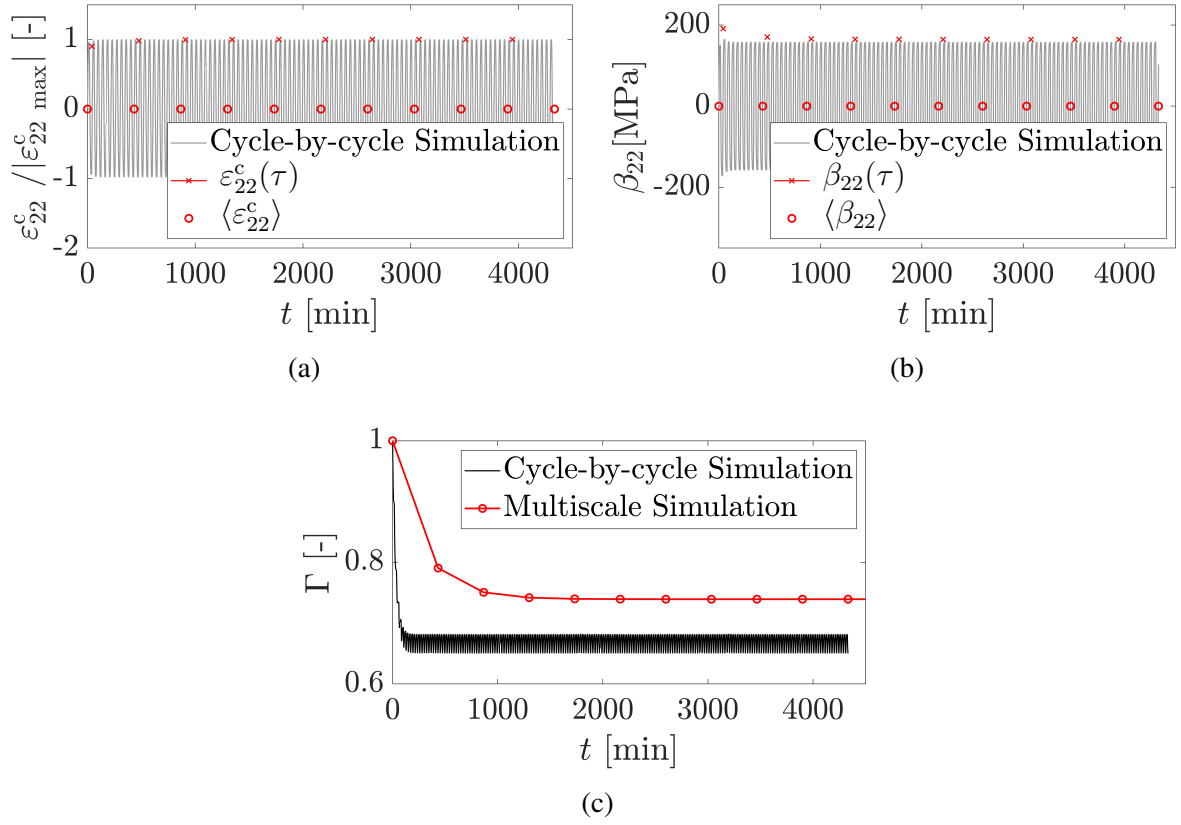


Figure 4.9: Comparison of the internal variables with respect to the multiscale solution: for the inelastic strain  $\varepsilon^c$  (a), the backstress  $\beta$  (b) and the softening variable  $\Gamma$  (c)

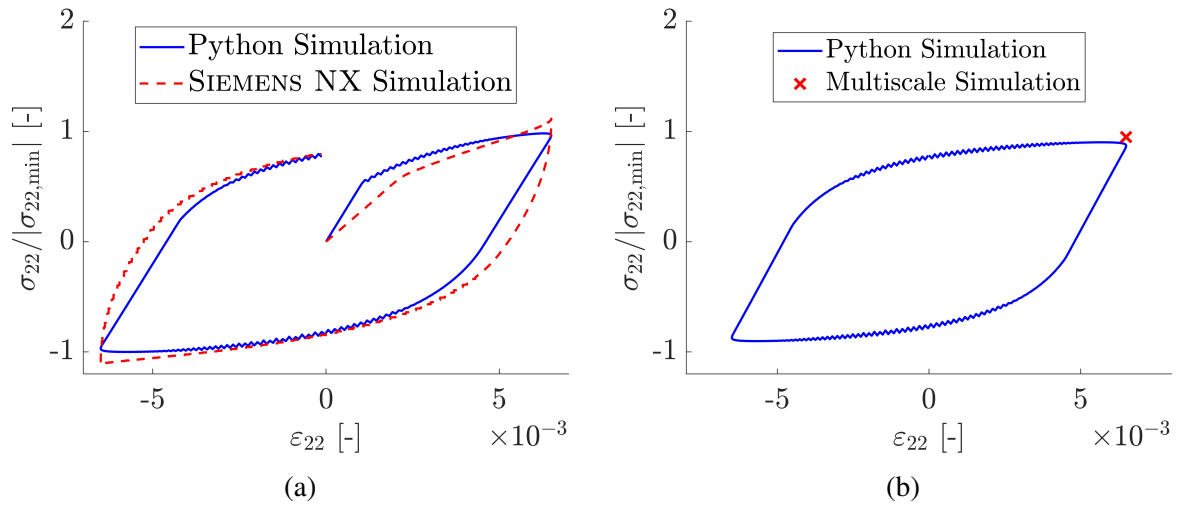


Figure 4.10: Hysteresis loop of the first cycle compared to the SIEMENS NX Solution (a) and the with respect to the 100<sup>th</sup> cycle compared to the multiscale solution (b)

Table 4.2: Comparison of the simulation times for the cycle-by-cycle simulation and two-time-scale solution for X12CrMoWVNbN10-1-1

$N$	<b>Cycle-by-cycle</b> [s]	<b>Multiscale</b> [s]	<b>Reduction</b> [%]
$10^2$	560.57	99.28	82.29

As expected from the fully resolved reference solution, both quantities oscillate symmetrically around zero, resulting in an average value for  $\langle \varepsilon_{22}^c \rangle$  and  $\langle \beta_{22} \rangle$  of zero. Furthermore, it is observed that the internal variable  $\Gamma$  increases rapidly during the initial loading cycles. This steep evolution requires the micro solver to take smaller time steps in order to ensure numerical stability, which leads to longer computational times at the beginning of the simulation. Increasing the number of micro time steps per cycle additionally confirms that the end state of one fast cycle serves as the initial condition for the next, validating the periodicity assumption underlying the two-time-scale approach. This indicates that the multiscale approach captures the cyclic behavior with sufficient accuracy. The consistent transition of internal variables from one micro cycle to the next also illustrates the robustness of the multiscale algorithm in handling history-dependent inelastic effects, which are essential for reliable long-term fatigue predictions.

The simulation times are significantly higher compared to Subsect. 3.2.3 which is due to a longer total observation time, as the period is now approximately 100 times larger than for the other LCF profile. Therefore, the time steps were adapted accordingly. With adapted time step sizes of  $\Delta t = 10^{-1} \text{min}$  and a scaling parameter of  $\mu = 10^{-3}$ , the simulation time for  $N = 100$  cycles using the cycle-by-cycle approach was 54.79 s, while the corresponding multiscale simulation required only 27.21 s. This results in a computational time reduction of 50.33%. The comparison reveals that, although a significant speed-up is achieved through the application of the multiscale method, the percentage reduction is notably smaller than in the case of X20CrMoV12-1. This difference can be attributed to the nature of the scale separation, where for the second alloy X12CrMoWVNbN10-1-1, the characteristic time scales of the micro- and macrochronological processes are closer, slightly reducing the effectiveness of the two-time-scale decoupling.

Nevertheless, the parameters governing the temporal resolution such as  $\Delta t$  and  $\mu$ , can be further adjusted to better exploit the scale separation without compromising accuracy. With careful variation, these can be tuned to achieve greater computational savings without compromising the accuracy of the solution. A few combinations and their reduction potential are shown in Table 4.3.

Now plotting only the maximum stress values for each cycle shows the yield curve with respect to the number of cycles  $N$ . In Fig. 4.11 at the top, the comparison between the cycle-by-cycle simulation and the multiscale result is depicted for  $N = 100$  cycles. It can be observed that the numerical implementations match very well in terms of the decreasing maximum stress values, validating the accuracy of the multiscale approach when compared to the fully resolved solution. The relative error is plotted in Fig. 4.11 (bottom). In particular, the relative error remains within an acceptable range throughout the loading history, with a clear decreasing trend over successive cycles, which further confirms the convergence and reliability of the multiscale formulation when simulating a large number of cycles.

Table 4.3: Comparison of different simulation parameters for  $N = 100$  cycles with respect to the reduction in computational time

Scaling parameter	Macro time step $\Delta t_M$	Reduction [%]
Reference: $10^{-3}$	$10 P$	50.33
$2 \times 10^{-3}$	$2 P$	—
$2 \times 10^{-2}$	$20 P$	72.42
$2.5 \times 10^{-2}$	$25 P$	77.96
$3 \times 10^{-2}$	$30 P$	82.45

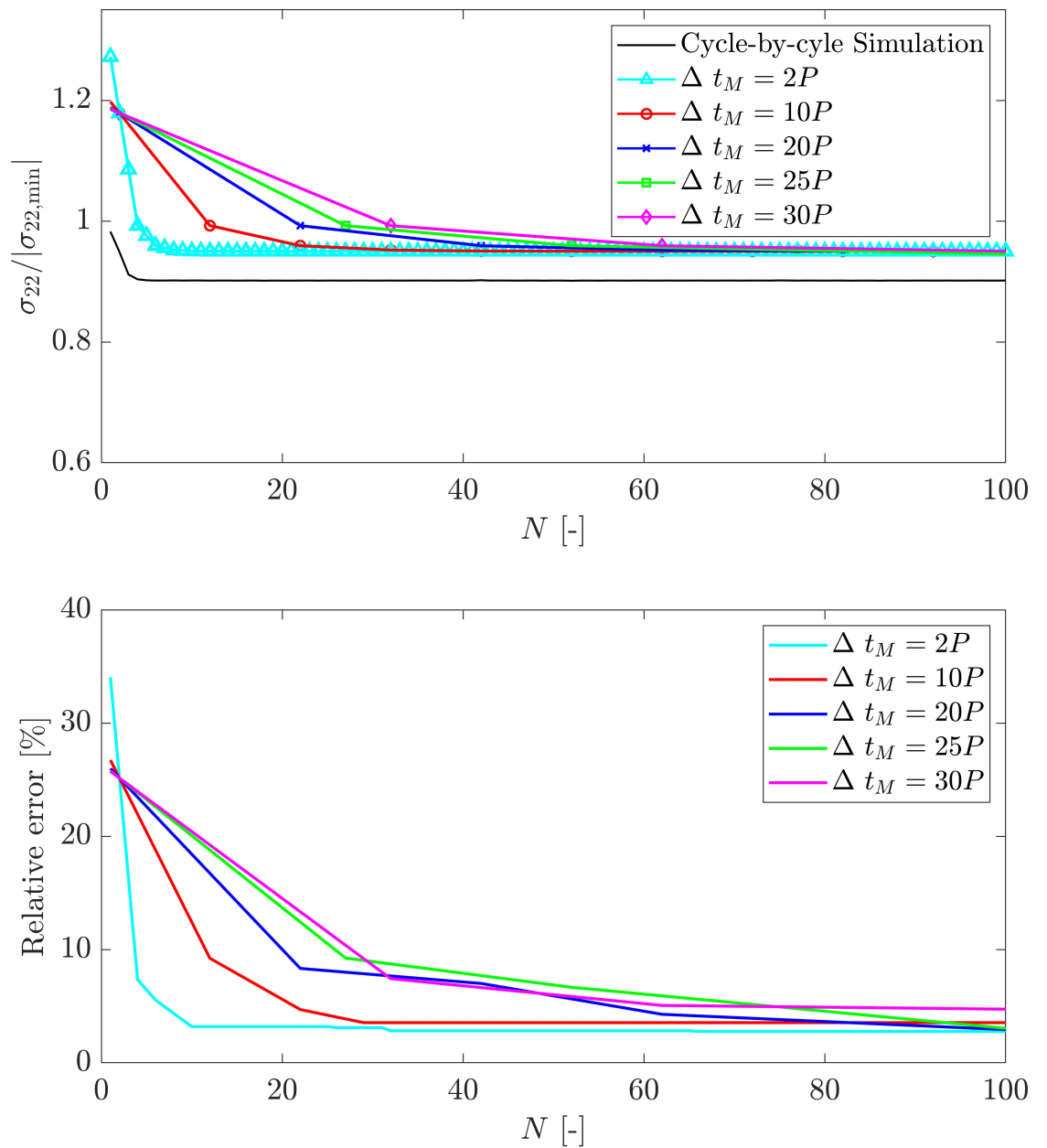


Figure 4.11: Maximum normalized stress with respect to the different macro time steps referred to in Table 4.3 (top) and the error development (bottom)

This confirms, that the smaller the macrochronological time step is chosen, the closer the solution gets to the fully resolved one. It was also already observed in Subsect. 3.2.3, that the error is reduced not only with decreasing slow time step but also with the increasing number of cycles. In the first micro-scale solution, the influence of the macro scale has not yet propagated into the system. As a result, the material response is governed solely by the initial conditions and the assumed periodic loading, which leads to an overestimation of the internal variables. This causes the highest deviation from the fully resolved reference solution and explains the peak error observed in the initial cycles. It is important to note that the observed error levels are within an acceptable range for multiscale simulations and do not compromise the overall accuracy or reliability of the results. As the simulation progresses, the multiscale solution gets closer to the fully resolved simulation, and the periodic solution gradually stabilizes, which further supports the reliability of the two-scale coupling in capturing long-term material behavior with reduced computational cost.

Finally, the obtained numerical results are compared to experimental yield curve, see Fig. 4.12. Here, a key limitation becomes evident: while the experimental curve shows a continuous decrease in stress amplitude  $\sigma_a$  with increasing number of cycles, indicating ongoing cyclic softening, the numerical results fail to capture this behavior beyond the first few cycles. This discrepancy highlights the need for an extended softening model that incorporates additional effects especially occurring during cyclic loading.

In the fully resolved simulation, the stress amplitude exhibits a noticeable reduction only within the first few cycles, after which it stabilizes at an almost constant value. This plateau suggests that the softening process, which should evolve gradually under cyclic loading, saturates too quickly in the current material model.

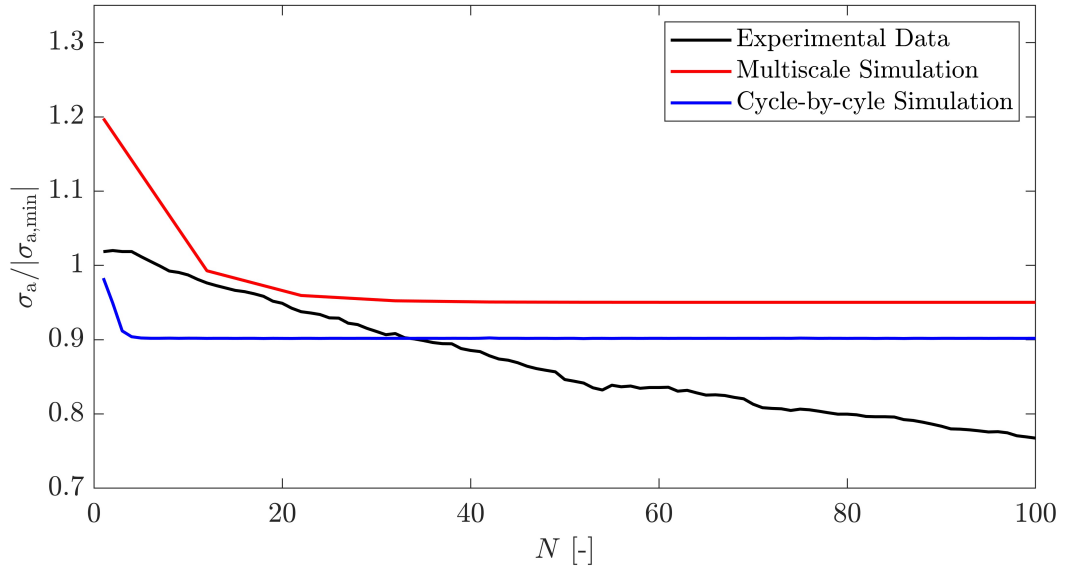


Figure 4.12: Comparison of normalized maximum stress values  $\sigma_a / |\sigma_{a,min}|$  per cycle  $N$  for the cycle-by-cycle simulation (reference), the multiscale solution ( $\Delta t_M = 10P$ ), and experimental measurements (the stress values are normalized using the absolute minimum of the reference simulation)

The root cause of this discrepancy lies in the formulation of the evolution equation describing the softening variable  $\Gamma$ , whose value increases too rapidly, leading to an overly stiff representation of the material's cyclic degradation. Consequently, the model underestimates the long-term evolution of inelastic mechanisms<sup>1</sup>. To overcome this limitation, a revised evolution law is introduced in Chapt. 5, which explicitly incorporates the influence of strain amplitude over repeated cycles. This modification aims to improve the model's capability to replicate the progressive softening observed in high-temperature fatigue tests, thereby enhancing its predictive performance under extended cyclic loading conditions.

---

<sup>1</sup>Riepin, B. (2024). Ertüchtigung eines konstitutiven Kriechmodells für industrielle Anwendung mit Parameter-Identifizierung mithilfe von künstlichen neuronalen Netzen und Implementierung in UMAT. Masterthesis, Otto-von-Guericke-Universität, Magdeburg.

# 5 Formulation and Identification of a New Softening Model

In Sect. 4.3 it became obvious, that the material model is not showing the right behavior with respect to the decreasing stress amplitude for a large number of cycles. Compared to the experimental results, the amplitude rather stays constant after the first few cycles. The goal of this section is to derive an approach to improve the model's response. The reduction of the maximum stress value per cycle is based on the formulation of the softening process. Adapting Eq. (4.4) and using the experimental data as input, the two-time-scale approach can be used to efficiently identify an unknown material parameter.

## 5.1 Adaption of the Material Model

The aim is to adapt the evolution equation for the softening variable  $\Gamma$ . In order to achieve that, we consider a cyclic strain loading profile. The current model uses

$$\dot{\Gamma} = A_S (\Gamma_\star - \Gamma) \dot{\varepsilon}_{\text{vM}}^c \quad (5.1)$$

with

$$\dot{\varepsilon}_{\text{vM}}^c = \left( \frac{2}{3} \dot{\varepsilon}^{\text{pl}} \cdot \dot{\varepsilon}^{\text{pl}} \right)^{\frac{1}{2}}. \quad (5.2)$$

For the uni-axial stress state, (5.1) takes the form

$$\dot{\Gamma} = A_S (\Gamma_\star - \Gamma) |\dot{\varepsilon}^{\text{pl}}|. \quad (5.3)$$

Integrating Eq. (5.3) once with respect to time and inserting the initial condition of at  $t = 0$  yields

$$-\ln \left( \frac{\Gamma - \Gamma_\star}{1 - \Gamma_\star} \right) = -A_S \varepsilon^{\text{pl}} \quad (5.4)$$

or rewritten as

$$\frac{\Gamma - \Gamma_\star}{1 - \Gamma_\star} = \exp \left( -A_S \varepsilon^{\text{pl}} \right). \quad (5.5)$$

In terms of a cyclic strain profile, the right-hand side  $r$  has to be divided into the following four intervals for  $t = [0, P]$

$$r = \int_0^{t_1} \dot{\varepsilon}^{\text{pl}} dt + \int_{t_1}^{t_2} \dot{\varepsilon}^{\text{pl}} dt - \int_{t_3}^{t_4} \dot{\varepsilon}^{\text{pl}} dt - \int_{t_4}^P \dot{\varepsilon}^{\text{pl}} dt \quad (5.6)$$

with

$$\int_{t_2}^{t_3} \dot{\varepsilon}^{\text{pl}} dt = 0 \quad (5.7)$$

as shown in Fig. 5.1 where one period with the corresponding plastic strain and the strain rate is pictured.

Therefore, it is now suggested, to change the right-hand side from  $r = A_S \dot{\varepsilon}_{\text{vM}}^{\text{pl}}$  to

$$R = A_S \frac{d}{dt} f(p) = A_S g(p) \dot{\varepsilon}_{\text{vM}}^{\text{pl}} \quad \text{with} \quad g(p) = \frac{df}{dp} \quad (5.8)$$

where

$$p = \int_0^t \dot{\varepsilon}_{\text{vM}}^{\text{pl}} d\tau. \quad (5.9)$$

In the context of creep behavior,

$$f(p) = p^m \quad \text{with} \quad p = \varepsilon^{\text{pl}} \quad (5.10)$$

so that integrating Eq. (5.8) leads to

$$\int_0^t A_S \frac{df}{dt} dt = A_S [f(\varepsilon^{\text{pl}}) - f(0)]. \quad (5.11)$$

Taking again a periodic profile such as the LCF test into account results in the decomposition of the integral into four subintegrals

$$\int_0^P \frac{df}{dt} dt = f(p) \Big|_0^{t_1} + f(p) \Big|_{t_1}^{t_2} + f(p) \Big|_{t_3}^{t_4} + f(p) \Big|_{t_4}^P \quad (5.12)$$

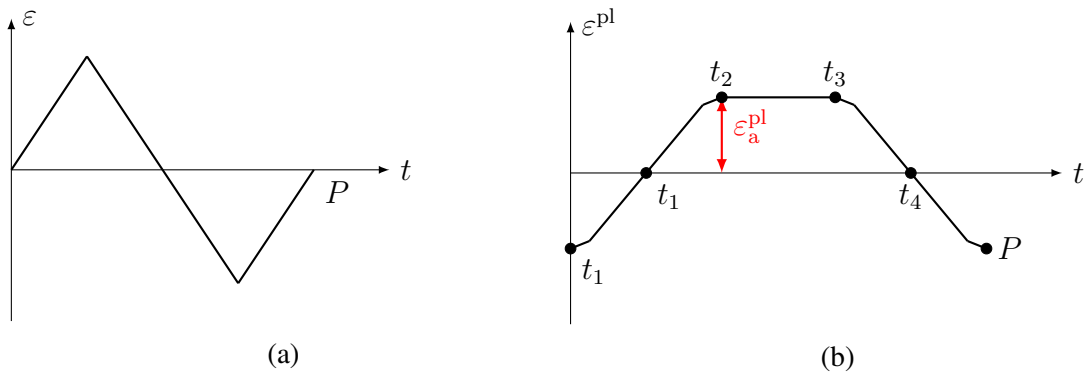


Figure 5.1: Qualitative sketch to show the dependency of the cyclic strain (a) and plastic strain amplitudes (b) on time



with the results of the function  $p$  at the different integral limits

$$\begin{aligned} p(0) &= 0, & p(t_1) &= \varepsilon^{\text{pl}} \Big|_0^{t_1} = \varepsilon_a, \\ p(t_2) &= \varepsilon^{\text{pl}} \Big|_0^{t_1} = 2 \varepsilon_a, & p(t_3) &= 2 \varepsilon_a, \\ p(t_4) &= \varepsilon_a, & p(P) &= 2 \varepsilon_a. \end{aligned} \quad (5.13)$$

These calculations lead to the following change in the right-hand side  $r$  of creep to  $R$  for periodic strain profiles

$$r = f(\varepsilon^{\text{pl}}), \quad (5.14)$$

$$R = f(2\varepsilon_a^{\text{pl}}) \quad (5.15)$$

with

$$2\varepsilon_a^{\text{pl}} = \Delta\varepsilon^{\text{pl}}. \quad (5.16)$$

Here,  $\Delta\varepsilon^{\text{pl}}$  denotes the plastic strain range, which represents the total variation in plastic strain experienced by the material during a complete loading cycle. This relationship is fundamental in fatigue analysis and underpins the classical COFFIN-MANSON relation, which correlates the plastic strain amplitude  $\varepsilon_a^{\text{pl}}$  to the number of cycles to failure [34]. Beyond fatigue life prediction, the strain range has also been used as a key parameter for describing softening behavior in cyclic loading. For instance, in [163], the strain range is utilized to examine cyclic softening in steels subjected to high-temperature low-cycle fatigue and in [155], it is employed to characterize strain-induced softening in natural rubber composites. Motivated by these studies, the softening model in the present work is extended such that the evolution of the softening variable  $\Gamma$  depends not only on the equivalent creep strain rate but also explicitly on the plastic strain amplitude. This enhancement improves the model's ability to represent cyclic softening behavior more accurately.

## 5.2 Calculation of Adapted Softening Evolution

In this section, the newly developed equation is implemented in the two-time-scale approach which is used to identify the missing material parameter, the exponent  $m$  in Eq. (5.10). The general stress response is approximated using a power-law fit

$$y = a x^b + c \quad (5.17)$$

with three parameters (see Table 5.1) depicted in red in Fig. 5.2.

---

<sup>0</sup>Kostenko, Y., Almstedt, H., Scholz, A., Linn, S., Naumenko, K., Kutschke, A., Prygorniev, O. (2012). Langzeitdehnverhalten (LCF-Ermüdung) von großen Dampfturbinenkomponenten im Hochtemperaturbereich. *Verbundprojekt COORETEC-Turbo III*.

Table 5.1: Coefficients and root mean square error of the power law function fitting the experimental values<sup>1</sup>

Function	RMSE	Coefficients		
$y$	4.8879	$a = -27.3309$	$b = 0.2062$	$c = 415.2802$

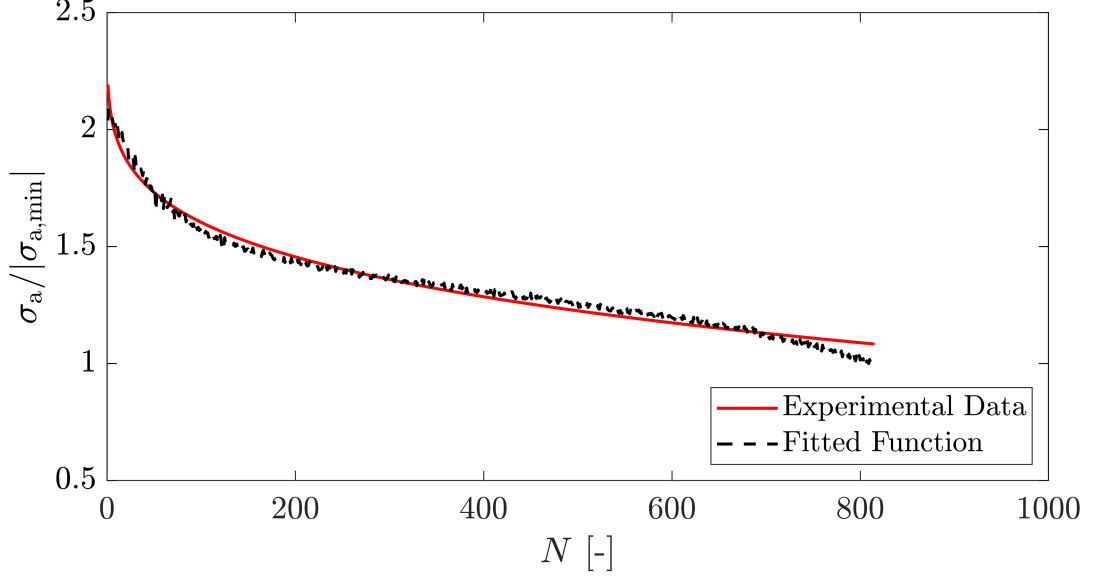


Figure 5.2: Fitting result of the experimental strain input

The fitted function is now inserted as the reference stress result of the fast scale and serves for evaluating the accuracy of the numerical solution. Since the microchronological solution also evolves with respect to time, the derivative of the given data was used. The evolution of the plastic strain and backstress equations on the micro scale and the calculation of  $\Gamma$  on the macro scale are not changed.

Since now the softening is not depending explicitly on the VON MISES strain rate but on the inelastic amplitude, this is calculated as

$$\varepsilon_a^{\text{pl}}(\tau) = \frac{1}{2} \left( \max_{\tau} \|\varepsilon^{\text{pl}}(\tau)\| - \min_{\tau} \|\varepsilon^{\text{pl}}(\tau)\| \right). \quad (5.18)$$

The chosen macro time step of  $\Delta t_M = 10 P$  offers the possibility to calculate the error between the computed  $\sigma_a(\tau)$  and the fitted function every 10 periods. In, Algorithm 3, the general procedure is explained.

---

**Algorithm 3** New algorithm to describe the fitting of the material parameter with the help of the multiscale procedure

---

1. **Input:** Prescribed stress profile  $\sigma(t)$ , parameter set  $m = \{0.5, 1.0, 1.5, 2.0\}$
  2. Initialize the slow and fast variables at  $t_M = t_{M_0}$
  3. For each value of  $m$ :
    - a) **Multiscale algorithm:**
      - i. Iterate from  $t_{M_0}$  to  $t_{M_n}$ :
        - A. Solve microchronological problem for one period
        - B. Solve the macrochronological problem with input values from previous step and in dependency of  $m$
        - C. Average over fast time using trapezoidal rule
        - D. Update the slow variables
    - b) **Evaluate the error:**
      - Compare predicted response with reference
      - Compute error  $E(m)$
  4. **Return:** the parameter  $m$  and the error  $E(m)$
- 

The selected interval for the exponent  $m$  is justified by the observed numerical behavior during the simulation when using values outside the chosen range. Values of  $m$  higher than 2.0 lead to large stress values in the hyperbolic sine based stress response function, which cause overflow errors and result in unstable or non-physical solutions. By restricting  $m$  to a moderate range, the model remains numerically stable and physically meaningful, ensuring reliable results throughout the simulation. This constraint is therefore not only physically motivated but also essential from a numerical standpoint.

Since the experimental data is available for  $N = 800$  cycles, the same number is once simulated with the fully resolved model, resulting in a computational time of 472.56s. The implementation of the newly derived softening evolution equation has also improved the stability of the two-time-scale approach. This enhanced representation reduces numerical instabilities that previously arose from abrupt or non-physical changes in the softening variable, particularly during the early cycles. This not only leads to more accurate macroscopic predictions but also enhances the robustness of the homogenization scheme under complex cyclic loading conditions. The simulation time for 800 cycles yields 101.01s with a reduction of 78.62% in the computational cost. The resulting errors for the different exponents  $m$  are depicted in Table 5.2.

The resulting yield curves for  $m = 2.0$  are shown in Fig. 5.3. The introduction of the new softening evolution equation significantly improves the model's ability to capture the material response during the first few hundreds of cycles. In both the fully resolved and the multiscale simulations, the initial decrease in stress amplitude compared to the experiment is well reproduced, closely matching the expected physical behavior.

Table 5.2: Error calculation with respect to the cycle number for the different simulations varying the exponent  $m$  in the softening evolution compared to the experimental data

Cycle number	Error [%]				
	$m = 0.5$	$m = 1.0$	$m = 1.5$	$m = 2.0$	before
10	27.98	26.91	20.44	12.91	7.89
20	25.32	24.19	23.33	9.29	4.51
50	18.38	17.17	17.07	1.81	4.37
100	7.12	5.74	5.64	2.06	18.77
150	3.65	2.20	2.11	0.79	23.2
200	0.05	1.45	1.56	2.67	27.82
300	5.9	7.48	7.61	7.78	35.42
500	13.98	15.68	15.81	15.82	46.56
800	41.36	43.49	43.63	43.64	80.77
$\emptyset$	15.97	16.03	15.24	10.75	27.70

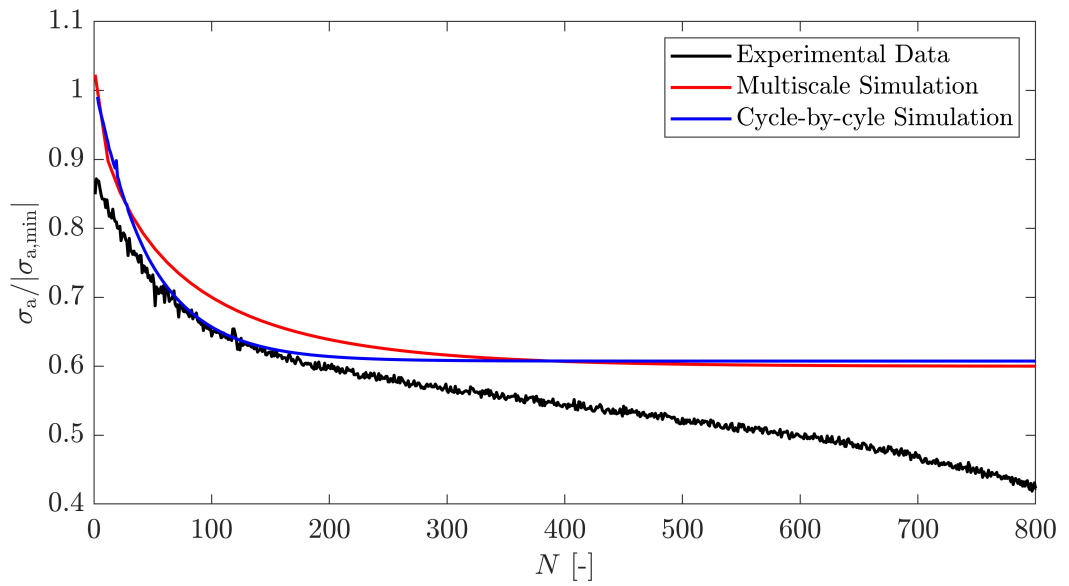


Figure 5.3: Comparison of the experimental data, the two-time-scale approach and the fully resolved simulation for  $N = 800$  cycles of the LCF profile with the exponent  $m = 2.0$

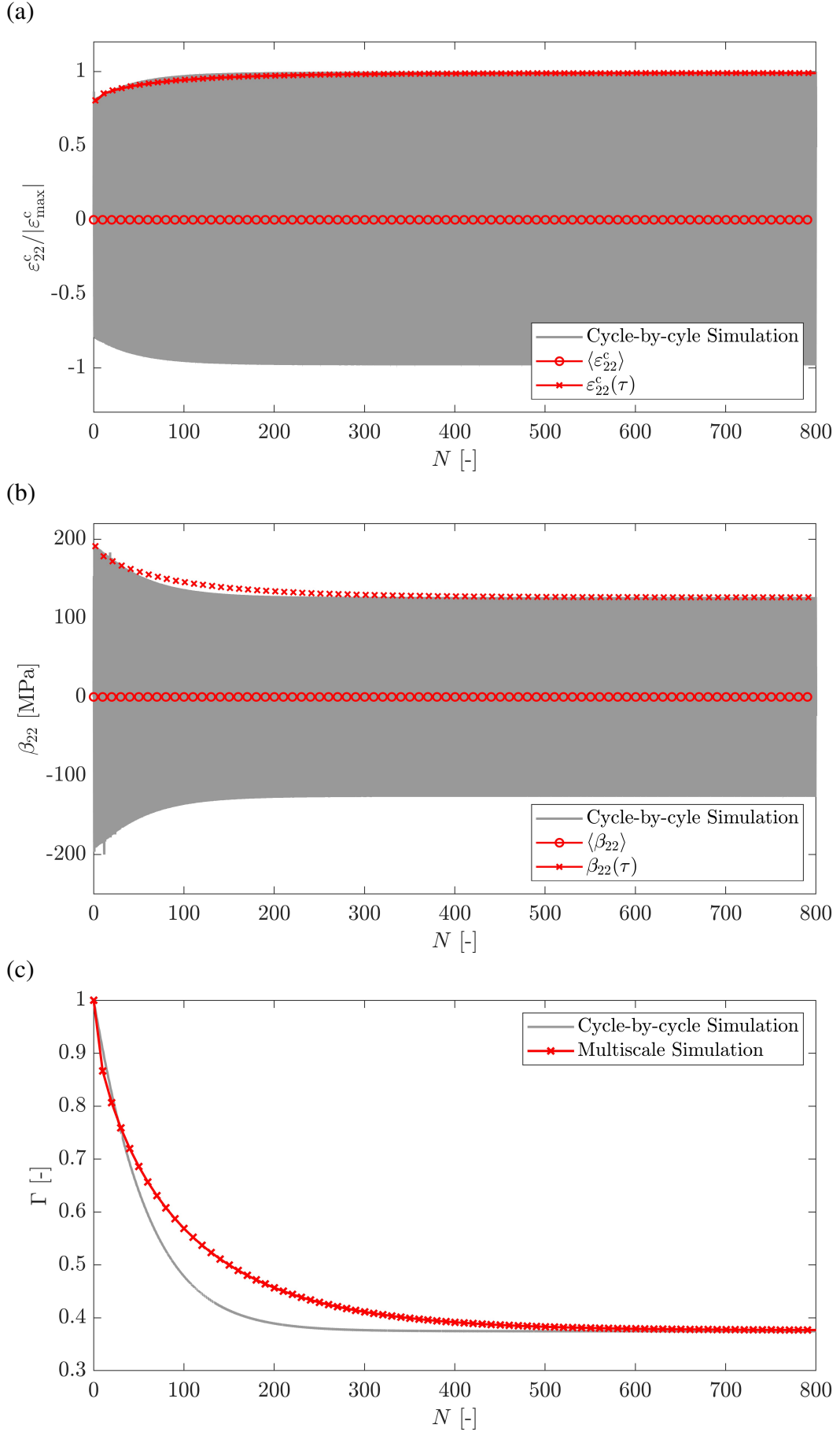


Figure 5.4: Comparison of the internal variables between the cycle-by-cycle integration and the multiscale solution for  $m = 2.0$  for the inelastic strain  $\varepsilon_{22}^c$  (a), the backstress  $\beta_{22}$  (b) and the softening variable  $\Gamma$  (c)

Furthermore, both simulations converge toward the same stabilized stress amplitude after a larger number of cycles compared to the previous softening formulation. This indicates that the new approach not only enhances the accuracy of early-cycle predictions but also provides a more realistic representation of the long-term cyclic softening behavior. However, the multiscale simulation slightly overestimates the stress amplitudes. This is likely due to a delayed evolution of the softening variable calculated at the slow scale, while the remaining internal variables, the inelastic strain and backstress show accurate magnitudes, see Fig. 5.4. This suggests that the more gradual softening evolution is the dominant factor which leads to the minor deviation observed.

### 5.3 Validation of the New Parameter

To validate the new defined softening behavior, the results of the multiscale code including the updated evolution equation for  $\Gamma$  with the exponent  $m = 2.0$  yielding the least averaged relative error are compared to the experimental results<sup>1</sup> for the LCF test with constant strain rate of  $\dot{\epsilon} = 0.046 \frac{\%}{\text{min}}$ . The normalized yield curves are illustrated in Fig. 5.5, the difference in the softening evolution itself is pictured in Fig. 5.6 comparing the results of the two evolution equations simulated with the multiscale procedure.

Especially in the initial cycles, the introduced cyclic softening evolution shows a significantly improved agreement with the experimental data, capturing the early stress amplitude reduction more accurately. However, as observed in Sect. 5.2, the stress response tends to stabilize too early at a nearly constant value, which slightly underrepresents the gradual nature of cyclic softening seen in the experiments. Nevertheless, the new approach provides a clearly improved description of the softening behavior over the full loading history and better reflects the material's cyclic degradation compared to the previous formulation.

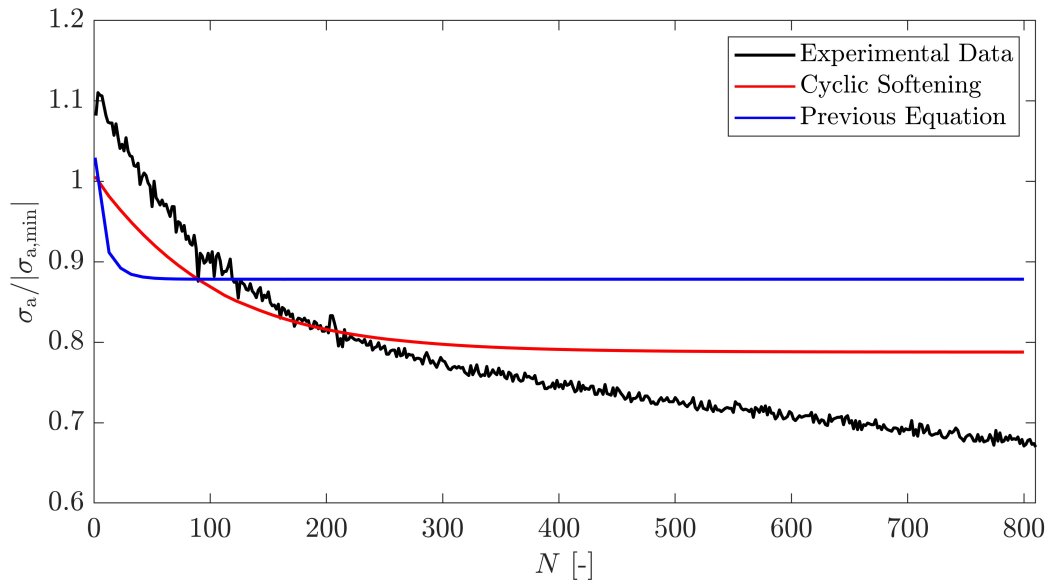


Figure 5.5: Comparison of the experimental data, the two-time-scale approach including the new cyclic softening evolution and the applying the previous definition

<sup>1</sup>Kostenko, Y., Almstedt, H., Scholz, A., Linn, S., Naumenko, K., Kutschke, A., Prygorniev, O. (2012). Langzeitdehnverhalten (LCF-Ermüdung) von großen Dampfturbinenkomponenten im Hochtemperaturbereich. Verbundprojekt COORETEC-Turbo III.

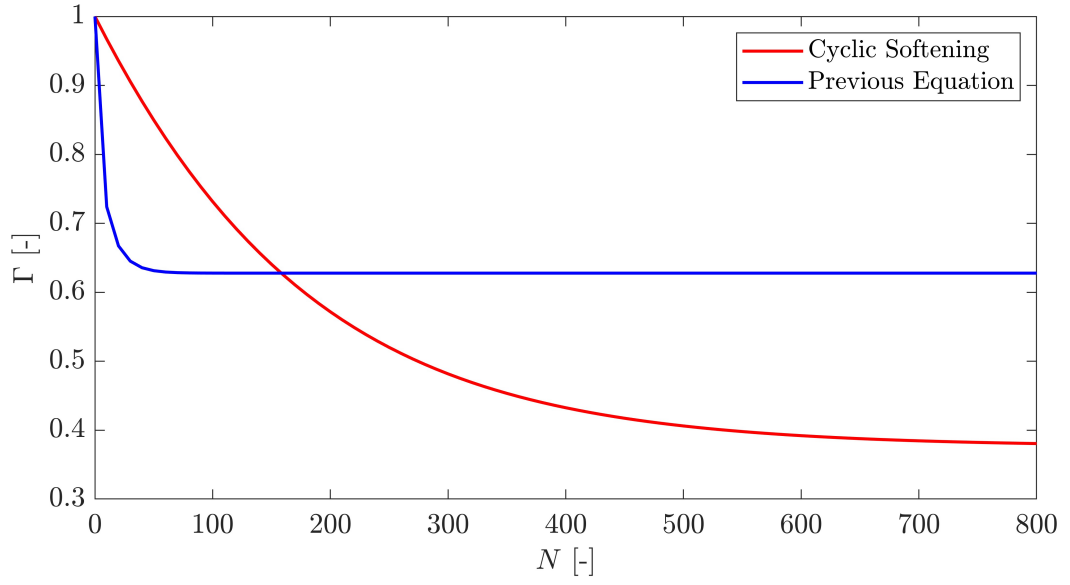


Figure 5.6: Comparison of the cyclic softening evolution with the previous definition with respect to a large number of cycles

## 6 Summary and Outlook

This thesis presents the development and implementation of a multiscale computational framework for simulating the inelastic behavior of high-temperature steels under cyclic and thermo-mechanical loading. Motivated by the need to reduce computational effort while maintaining accuracy, the work builds on the two-time-scale approach, which separates the mechanical response into fast and slow time components. This method is particularly suited for simulating long-duration loading histories, such as those experienced by structural components in power plants, where thousands of cycles occur over a component's service life, requiring accurate resolution of both short-term cyclic behavior and long-term material degradation.

The theoretical foundation is rooted in continuum mechanics and thermodynamically consistent constitutive modeling. Rate-dependent plasticity, internal variables, and time integration schemes form the basis of the numerical approach. The formulation includes evolution equations for internal variables such as inelastic strain, backstress, and a softening parameter, which together describe the material's response to cyclic loading with a focus on time- and temperature-dependent effects. Within this framework, the governing equations are formulated and solved using both traditional time-integration techniques and the multiscale method, which enables efficient computation by solving the fast-scale problem only at selected points and using the results to inform the evolution of slow-scale variables.

The Python-based implementation of the model is first applied to X20CrMoV12-1 steel, with results validated against fully resolved as well as finite element simulations using ABAQUS. The model accurately captures key material behaviors under low cycle fatigue and thermo-mechanical fatigue conditions. In particular, the model demonstrates its capability of handling non-isothermal loading paths by incorporating temperature-dependent material properties, which is crucial for replicating the thermal-mechanical interaction present in TMF. This is demonstrated through a TMF test scenario with synchronized thermal and mechanical cycles, where the model accurately predicts the stress response including relaxation effects and enhanced inelastic strain accumulation due to thermal activation.

The multiscale simulation shows a substantial reduction of more than 80% in computational time compared to cycle-by-cycle analysis. The implemented temporal homogenization allows large macro time steps that span multiple cycles while retaining fidelity to the cyclic stress-strain behavior, thereby enabling simulation of long-term fatigue effects within practical time frames. The same methodology is then extended to X12CrMoWVNbN10-1-1 steel, demonstrating the flexibility and robustness of the modeling approach as the results are validated against finite element simulations and experimental data. Material-specific parameters are identified for this steel to reflect its distinct cyclic response, and in both cases, the multiscale model reliably reproduces the stress response and internal variable evolution under complex loading. For the application to X12CrMoWVNbN10-1-1, the results further suggest that a hybrid simulation strategy can significantly enhance both accuracy and efficiency. In particular, performing a fully resolved cycle-by-cycle simulation for the initial loading cycles followed by a switch to the multiscale framework for the remaining service life, would allow for ac-



curate capture of early material evolution while benefiting from the computational advantages of the two-time-scale approach. This strategy reflects the fact that the softening behavior in high-temperature steels is most active during the first few cycles, after which the material response tends to stabilize. Adopting such a staged simulation process is therefore recommended for industrial applications, enabling faithful reproduction of key mechanical phenomena while achieving substantial reductions in computational cost.

To further enhance the model's predictive capabilities, a new formulation for the evolution of the softening variable is introduced. By incorporating the plastic strain amplitude into the evolution law, the model more accurately reflects the material's cyclic softening behavior. This approach is inspired by fatigue literature, where strain amplitude plays a key role in damage and softening evolution. Parameter identification is performed using numerical fitting techniques for a low cycle fatigue test with a strain rate of  $\dot{\epsilon} = 0.06 \frac{\%}{\text{min}}$ , and the updated model showed improved agreement when applied to the LCF test with  $\dot{\epsilon} = 0.046 \frac{\%}{\text{min}}$  and compared to reference experimental data. The use of amplitude-based evolution enhances the model's ability to capture cycle-dependent degradation, especially under varying strain amplitudes. While the newly developed model performs better than the previous one in capturing early-cycle softening and stress amplitude reduction, it still requires further refinement to accurately represent the material behavior in later cycles, where long-term stabilization occurs. To improve the efficiency and objectivity of the parameter identification, the manual variation of the softening exponent can be replaced with an automated optimization process. Python-based optimization algorithms (e.g. `scipy.optimize` or gradient-based solvers) can be employed to automatically calibrate the model parameters. This approach enables a more systematic identification of optimal material parameters, reduces user bias, and significantly accelerates the fitting process, particularly for complex, nonlinear constitutive models.

Overall, this work establishes the foundation for a computationally efficient, physically realistic simulation of inelastic cyclic material behavior. It sets the stage for future developments to apply the model to more complex structural simulations, such as components with spatial inhomogeneities or multiaxial stress states, and to explore its integration within commercial FEM environments for industrial-scale applications.

## 6.1 Conclusions

This thesis demonstrates a computational framework for simulating the inelastic behavior of high-temperature steels subjected to cyclic and thermal loading. By incorporating a two-time-scale approach, the model achieves a balance between computational efficiency and physical accuracy. The work highlights several key outcomes

- In contrast to existing multiscale implementations primarily applied to generic viscoelastic–viscoplastic materials, this work focuses specifically on high-temperature steels, addressing their complex cyclic plasticity.
- The Python-based implementation accurately reproduces cyclic material behavior, validated against FEM and experimental data.
- The multiscale algorithm successfully decouples fast and slow dynamics, enabling efficient long-term simulations over thousands of cycles.

- The methodology is generalizable and successfully applied to different high-temperature steels.
- The multiscale formulation was adapted to represent key internal variables, such as inelastic strain and backstress, on both fast and slow time scales, enabling accurate capture of cyclic transients as well as long-term material evolution.
- The adaptation of the softening model, by including the plastic strain amplitude, improves accuracy under cyclic loading and enhances predictive capabilities for cyclic softening.

## 6.2 Further Research

Despite its significant advantages, the two-time-scale approach is subject to certain limitations that must be considered in future applications and extensions. First, the method assumes periodic or quasi-periodic loading conditions. Under non-periodic or highly transient scenarios, the required scale separation may no longer hold, potentially compromising accuracy [132]. Furthermore, in materials exhibiting strong path-dependence or microstructural memory effects, the homogenized fast-scale response may not adequately reflect the local history, particularly in early cycles [52]. The method is also sensitive to abrupt non-linearities or transitions in material behavior, such as crack initiation or phase transformation, where the assumption of slowly varying macro-scale evolution becomes invalid. Additionally, while the computational efficiency benefits are substantial, they depend heavily on appropriate choices for the scaling parameter  $\mu$  and the macro time increment  $\Delta t_M$ . Poor calibration can lead to either numerical instability or loss of fidelity. Finally, in cases involving very few cycles or short time-to-failure scenarios, the multiscale advantage diminishes, and fully resolved simulations may still be necessary to capture the full evolution of material damage.

Acknowledging these limitations highlights the importance of further methodological development to enhance the model's applicability in practical engineering contexts. In the present work, the three-dimensional constitutive equations for the phase-mixture model were implemented within a multiscale Python framework, enabling the separation of mechanical behavior across different time scales. To extend this approach for practical engineering applications and to capture more complex physical phenomena, future work should address two major developments: the inclusion of damage evolution, and the integration of the model within a finite element method framework. This would allow for full-field simulations of engineering structures while maintaining the computational efficiency offered by the temporal two-scale approach. This implementation can be viewed as a foundational step toward coupling the developed algorithm with commercial FEM software, with the ultimate goal of significantly reducing computational time in large-scale simulations.

As outlined in [70], an efficient multiscale simulation strategy involves solving the initial boundary value problem through detailed cycle-by-cycle analysis for the first few cycles. This high-fidelity solution provides insight into the local mechanical response and allows for the identification of critical integration points, such as regions of stress concentration or high inelastic strain accumulation. Once these points are identified, the two-time-scale algorithm can be applied selectively, concentrating computational resources where needed while coarsening the temporal resolution elsewhere.

The macro- and microchronological time scales are introduced by additively decomposing the total simulation time: the macro time scale captures slow structural evolution, while the

micro time scale resolves the rapid cyclic oscillations of local stress and strain. The macro time increment can be dynamically adapted depending on the degree of nonlinearity or rate of change in the macro response [70]. Typically, an error estimator or convergence tolerance is used to control this adaptive stepping, ensuring both accuracy and efficiency. The overall computational workflow involves the following main steps

- **Initialization:** At the beginning of each macro time step  $\Delta t_M$ , the state variables on the fast time scale and the applied strain increment are required. These serve as initial conditions for solving the fast-scale problem over a representative loading period at each critical point.
- **Fast-scale integration:** The boundary value problem is solved in the fast time domain  $\tau$  to capture the material's response over a loading cycle. The solution is used to compute cycle-averaged quantities, which are passed to the macro solver.
- **Data storage and exchange:** To maintain consistency in data exchange between time scales and across simulation domains, the fast-scale results are saved in external files. This step is crucial for managing memory and enabling post-processing or re-use of data in subsequent cycles [70, 123].
- **Macro-scale update:** Using the averaged or homogenized data from the microchronological analysis, the macro-scale problem is advanced in time. The updated macro state then serves as input for the next fast-scale calculation.

An alternative approach involves direct coupling of the Python-based multiscale code with commercial FEM software via their application programming interfaces. For example, ABAQUS offers a powerful scripting interface in Python, allowing programmatic control over model definition, simulation settings, and user subroutines. Through this interface, custom routines can be embedded into the FEM workflow, enabling direct integration of the multiscale solver with the element-level computations. This method provides a flexible and scalable path for deploying multiscale models in real-world structural simulations, particularly in practical engineering simulations like fatigue-critical applications such as welded joints, notched specimens, or complex geometries [1, 123].

Ultimately, combining the two-time-scale method with FEM allows for the simulation of large structures under realistic loading while retaining detailed resolution of the local cyclic response. This is especially beneficial in cases where fatigue or long-term degradation is driven by micromechanical evolution over many cycles.

# Bibliography

- [1] Abaqus. *ABAQUS Analysis User's Manual*. <https://classes.engineering.wustl.edu/2009/spring/mase5513/abaqus/docs/v6.6/>. Online; accessed 08. September 2021.
- [2] Abdulle, A., Weinan, E., Engquist, B., and Vanden-Eijnden, E. “The heterogeneous multiscale method”. In: *Acta Numerica* 21, 2012, pp. 1–87. ISSN: 1474-0508, 0962-4929. DOI: 10.1017/S0962492912000025.
- [3] Agamennone, R., Blum, W., Gupta, C., and Chakravartty, J. “Evolution of microstructure and deformation resistance in creep of tempered martensitic 9–12%Cr–2%W–5%Co steels”. In: *Acta Materialia* 54(11), 2006, pp. 3003–3014. DOI: 10.1016/j.actamat.2006.02.038.
- [4] Altenbach, H., Breslavsky, D., Naumenko, K., and Tatarinova, O. “Two-time-scales and time-averaging approaches for analysis of cyclic creep based on Armstrong–Frederick type constitutive model”. In: *Proceedings of the Institution of Mechanical Engineers, Part C: Journal of Mechanical Engineering Science* 233(5), 2019, pp. 1690–1700. DOI: 10.1177/0954406218772609.
- [5] Altenbach, H. and Knape, K. “On the main directions in creep mechanics of metallic materials”. In: *Mechanics - Proceedings of National Academy of Sciences of Armenia* 73 (3), 2020, pp. 24–43. DOI: 10.33018/73.3.2.
- [6] Altenbach, H. *Kontinuumsmechanik – Einführung in die materialunabhängigen und materialabhängigen Gleichungen*. 4th ed. Berlin, Heidelberg: Springer Vieweg, 2018. ISBN: 978-3-662-57503-1. DOI: 10.1007/978-3-662-57504-8.
- [7] Ascher, U. M. and Petzold, L. R. *Computer Methods for Ordinary Differential Equations and Differential-Algebraic Equations*. Philadelphia, PA: SIAM, 1998. ISBN: 978-0-898713-52-6.
- [8] Atkin, R. J. and Craine, R. E. “Continuum theories of mixtures: Basic theory and historical development”. In: *The Quarterly Journal of Mechanics and Applied Mathematics* 29(2), 1976, pp. 209–244. DOI: 10.1093/qjmam/29.2.209. eprint: <https://academic.oup.com/qjmam/article-pdf/29/2/209/5232968/29-2-209.pdf>.
- [9] Aubry, D. and Puel, G. “Two-timescale homogenization method for the modeling of material fatigue”. In: *IOP Conference Series: Materials Science and Engineering* 10, 2010, p. 012113. DOI: 10.1088/1757-899X/10/1/012113.
- [10] Bachmann, P. *Analytische Zahlentheorie*. Vol. 2. Leipzig: Teubner, 1894.
- [11] Barrett, R., O'Donoghue, P., and Leen, S. “An improved unified viscoplastic constitutive model for strain-rate sensitivity in high temperature fatigue”. In: *International Journal of Fatigue* 48, 2013, pp. 192–204. ISSN: 0142-1123. DOI: 10.1016/j.ijfatigue.2012.11.001.

- [12] Bathe, K.-J. *Finite Element Procedures*. Prentice Hall, 2006.
- [13] Becker, M. and Hackenberg, H.-P. “A constitutive model for rate dependent and rate independent inelasticity. Application to IN718”. In: *International Journal of Plasticity* 27, 2011, pp. 596–619. DOI: 10.1016/j.ijplas.2010.08.005.
- [14] Bejaoui, S. and Bary, B. “Modeling of the link between microstructure and effective diffusivity of cement pastes using a simplified composite model”. In: *Cement and Concrete Research* 37(3), 2007. Cementitious Materials as model porous media: Nanostructure and Transport processes, pp. 469–480. DOI: 10.1016/j.cemconres.2006.06.004.
- [15] Belytschko, T., Yen, H.-J., and Mullen, R. “Mixed methods for time integration”. In: *Computer Methods in Applied Mechanics and Engineering* 17-18, 1979, pp. 259–275. ISSN: 0045-7825. DOI: 10.1016/0045-7825(79)90022-7.
- [16] Belytschko, T., Smolinski, P., and Wing Kam Liu. “Stability of multi-time step partitioned integrators for first-order finite element systems”. In: *Computer Methods in Applied Mechanics and Engineering* 49(3), 1985, pp. 281–297. ISSN: 0045-7825. DOI: 10.1016/0045-7825(85)90126-4.
- [17] Benson, D. and Hallquist, J. “COMPUTATION FOR TRANSIENT AND IMPACT DYNAMICS”. In: *Encyclopedia of Vibration*. Ed. by Braun, S. Oxford: Elsevier, 2001, pp. 278–286. ISBN: 978-0-12-227085-7. DOI: 10.1006/rwvb.2001.0006.
- [18] Bensoussan, A., Papanicolau, G., and Lions, J. *Asymptotic Analysis for Periodic Structures*. Elsevier Science, 1978. ISBN: 9780080875262.
- [19] Bertram, A. *Elasticity and Plasticity of Large Deformations*. May 2014. ISBN: 978-3-642-24614-2. DOI: 10.1007/978-3-642-24615-9.
- [20] Besseling, J. and van der Giessen, E. *Mathematical Modeling of Inelastic Deformation*. Applied Mathematics. Taylor & Francis, 1994. ISBN: 9780412452802. URL: <https://books.google.de/books?id=IRRwxDHEDvIC>.
- [21] Bhattacharyya, M., Dureisseix, D., and Faverjon, B. “A unified approach based on temporal homogenisation and cycle jump for thermo-mechanical combined cycle fatigue”. In: *International Journal of Fatigue* 131, 2020, p. 105320. ISSN: 0142-1123. DOI: 10.1016/j.ijfatigue.2019.105320.
- [22] Bottasso, C. L. “Multiscale temporal integration”. In: *Computer Methods in Applied Mechanics and Engineering* 191(25), 2002, pp. 2815–2830. ISSN: 0045-7825. DOI: 10.1016/S0045-7825(02)00219-0.
- [23] Brandis, H., Huchtemann, B., and Steinen, A. von den. “Technologie der Wärmebehandlung warm- und hochwarmfester Stähle”. In: *TZ für Metallbearbeitung* 79(4), 1985, pp. 9–17.
- [24] Brigham, E. O. *The fast Fourier transform and its applications*. Prentice-Hall, Inc., 1988.

- [25] Bruckner, T., Bashmakov, I. A., Mulugetta, Y., Chum, H., Vega Navarro, A. De la, Edmonds, J., Faaij, A., Fungtammasan, B., Garg, A., Hertwich, E., Honnery, D., Infield, D., Kainuma, M., Khennas, S., Kim, S. H., Nimir, H. B., Riahi, K., Strachan, N., Wiser, R., and Zhang, X. “Energy Systems”. In: *Climate Change 2014: Mitigation of Climate Change. Contribution of Working Group III to the Fifth Assessment Report of the Intergovernmental Panel on Climate Change*. Ed. by Edenhofer, O., Pichs-Madruga, R., Sokona, Y., Farahani, E., Kadner, S., Seyboth, K., Adler, A., Baum, I., Brunner, S., Eickemeier, P., Kriemann, B., Savolainen, J., Schlömer, S., Stechow, C. von, Zwickel, T., and Minx, J. C. Cambridge, United Kingdom and New York, NY, USA: Cambridge University Press, 2014, pp. 511–597. URL: [https://www.ipcc.ch/site/assets/uploads/2018/02/ipcc\\_wg3\\_ar5\\_chapter7.pdf](https://www.ipcc.ch/site/assets/uploads/2018/02/ipcc_wg3_ar5_chapter7.pdf).
- [26] Burden, R. L., Faires, J. D., and Burden, A. M. *Numerical Analysis*. Cengage Learning, 2015.
- [27] Butcher, J. C. *Numerical Methods for Ordinary Differential Equations*. Wiley, 2008.
- [28] Butcher, J. C. “Implicit Methods for Stiff Problems”. In: *Numerical Methods for Ordinary Differential Equations*. Springer, 2003, pp. 163–176.
- [29] Butcher, J. C. *Numerical Methods for Ordinary Differential Equations*. 3rd. Chichester, UK: John Wiley & Sons, 2016. ISBN: 978-1-118-56033-6.
- [30] Chaboche, J. L. and Rousselier, G. “On the Plastic and Viscoplastic Constitutive Equations—Part II: Application of Internal Variable Concepts to the 316 Stainless Steel”. In: *Journal of Pressure Vessel Technology* 105(2), 1983, pp. 159–164. DOI: 10.1115/1.3264258.
- [31] Chaboche, J. “Constitutive equations for cyclic plasticity and cyclic viscoplasticity”. In: *International Journal of Plasticity* 5, 1989, pp. 247–302. DOI: 10.1016/0749-6419(89)90015-6.
- [32] Chaboche, J. “A review of some plasticity and viscoplasticity constitutive theories”. In: *International Journal of Plasticity* 24(10), 2008. Special Issue in Honor of Jean-Louis Chaboche, pp. 1642–1693. DOI: 10.1016/j.ijplas.2008.03.009.
- [33] Chyasnawichious, Q. K. and Siau, T. *Python Programming and Numerical Methods: A Guide for Engineers and Scientists*. Elsevier, 2021. URL: <https://pythonnumericalmethods.berkeley.edu>.
- [34] Coffin, L. F. “A study of the effects of cyclic thermal stresses on a ductile metal”. In: *Transactions of the ASME* 76(6), 1954, pp. 931–950.
- [35] Cognard, J.-Y. and Ladevèze, P. “A large time increment approach for cyclic viscoplasticity”. In: *International Journal of Plasticity* 9(2), 1993, pp. 141–157. ISSN: 0749-6419. DOI: 10.1016/0749-6419(93)90026-M.
- [36] Cojocaru, D. and Karlsson, A. “A simple numerical method of cycle jumps for cyclically loaded structures”. In: *International Journal of Fatigue* 28(12), 2006, pp. 1677–1689. ISSN: 0142-1123. DOI: 10.1016/j.ijfatigue.2006.01.010.
- [37] Coleman, B. D. and Noll, W. “Constitutive Equations for Materials with Memory”. In: *The Foundations of Mechanics and Thermodynamics*. Ed. by Truesdell, C. Berlin, Heidelberg: Springer-Verlag, 1963, pp. 49–101. DOI: 10.1007/978-3-540-37805-4\_2.

- [38] Combescure, A. and Gravouil, A. “A numerical scheme to couple subdomains with different time-steps for predominantly linear transient analysis”. In: *Computer Methods in Applied Mechanics and Engineering* 191, Jan. 2002, pp. 1129–1157. DOI: 10.1016/S0045-7825(01)00190-6.
- [39] Courant, R., Friedrichs, K., and Lewy, H. “Über die partiellen Differenzengleichungen der mathematischen Physik”. In: *Mathematische Annalen* 100(1), 1928, pp. 32–74. DOI: 10.1007/BF01448839.
- [40] Czichos, H., Skrotzki, B., and Simon, F. *Das Ingenieurwissen: Werkstoffe*. Springer Berlin Heidelberg, 2013. ISBN: 9783642411250. URL: <https://books.google.de/books?id=sSETngEACAAJ>.
- [41] Czycholl, G. “Periodic Structures”. In: *Solid State Theory, Volume 1: Basics: Phonons and Electrons in Crystals*. Berlin, Heidelberg: Springer Berlin Heidelberg, 2023, pp. 5–23. ISBN: 978-3-662-66135-2. DOI: 10.1007/978-3-662-66135-2\_2.
- [42] Davis, P. J. and Rabinowitz, P. *Methods of Numerical Integration*. Courier Corporation, 2007.
- [43] Dechema Forschungsinstitut. *Arbeitsgruppe Hochtemperaturwerkstoffe*. <https://dechema-dfi.de/hochtemperaturwerkstoffe.html>. Online; accessed 24. June 2021.
- [44] Devulder, A., Aubry, D., and Puel, G. “Two-time scale fatigue modelling: application to damage”. In: *Computational Mechanics* 45, 2010, pp. 637–646. DOI: 10.1007/s00466-010-0476-2.
- [45] DIN EN 10095:2018-12. *Hitzebeständige Stähle und Nickellegierungen; Deutsche Fassung EN 10095:1999*. December 2018.
- [46] Durand, L. “Models of tensile behaviour of two-phase alloys from their components”. In: *Materials Science and Technology* 3(2), 1987, pp. 105–109. DOI: 10.1179/mst.1987.3.2.105.
- [47] Dyson, B. E. and McLean, M. “Microstructural evolution and its effects on the creep performance of high temperature alloys”. In: *Microstructural Stability of Creep Resistant Alloys for High Temperature Plant Applications*. Ed. by Strang, A., Cawley, J., and Greenwood, G. W. Institute of Materials, 1997, pp. 371–393.
- [48] Eisenträger, J. “A Framework for Modeling the Mechanical Behavior of Tempered Martensitic Steels at High Temperatures”. PhD thesis. Otto-von-Guericke-Universität Magdeburg, 2018. URN: urn:nbn:de:gbv:ma9:1-11971.
- [49] Eisenträger, J., Naumenko, K., and Altenbach, H. “Calibration of a phase mixture model of hardening and softening regimes in tempered martensitic steel over wide stress and temperature ranges”. In: *The Journal of Strain Analysis for Engineering Design* 53, 2018, pp. 156–177. DOI: 10.1177/0309324718755956.
- [50] Ennis, P. and Quadakkers, W. “High chromium martensitic steels- Microstructure, properties and potential for further development”. In: *VGB PowerTech* 81, Jan. 2001, pp. 87–90.
- [51] Farhat, H. and Salvini, C. “Novel gas turbine challenges to support the clean energy transition”. In: *Energies* 15, 2022. DOI: 10.3390/en15155474.

- [52] Fish, J., Li, A., and Li, R. “Generalized Mathematical Homogenization: From theory to practice”. In: *Computer Methods in Applied Mechanics and Engineering* 197(41), 2008, pp. 3225–3248. DOI: 10.1016/j.cma.2007.12.002.
- [53] Fish, J. *Multiscale Methods: Bridging the Scales in Science and Engineering*. Oxford University Press, 2009.
- [54] Fournier, B., Sauzay, M., and Pineau, A. “Micromechanical model of the high temperature cyclic behavior of 9–12%Cr martensitic steels”. In: *International Journal of Plasticity* 27(11), 2011, pp. 1803–1816. ISSN: 0749-6419. DOI: 10.1016/j.ijplas.2011.05.007.
- [55] Fournier, B., Sauzay, M., Renault, A., Barcelo, F., and Pineau, A. “Microstructural evolutions and cyclic softening of 9%Cr martensitic steels”. In: *Journal of Nuclear Materials* 386-388, 2009, pp. 71–74. DOI: 10.1016/j.jnucmat.2008.12.061.
- [56] Frederick, C. and Armstrong, P. “A Mathematical Representation of the Multi Axial Bauschinger Effect”. In: *CEGB Report RD/B/N 731, Central Electricity Generating Board. The Report Is Reproduced as a Paper: 2007 Materials at High Temperatures* 24, 1966, pp. 1–26. DOI: 10.1179/096034007X20758.
- [57] Frei, S. and Richter, T. “Creep damage parameter extraction from ex-service 12% Cr steel using digital image correlation computed strain data”. In: *Computational Mechanics* 64(5), 2020, pp. 1129–1145. DOI: 10.1007/s00466-019-01796-5.
- [58] Frei, S. and Richter, T. “Efficient approximation of flow problems With multiple scales in time”. In: *Multiscale Modeling & Simulation* 18(2), 2020, pp. 942–969. ISSN: 1540-3459, 1540-3467. DOI: 10.1137/19M1258396.
- [59] Frei, S. and Richter, T. “Numerical implementation of a phase mixture model for rate-dependent inelasticity of tempered martensitic steels”. In: *Acta Mechanica* 226(7), 2020, pp. 2267–2281. DOI: 10.1007/s00707-019-02601-y.
- [60] Frost, H. J. and Ashby, M. F. *Deformation-Mechanism Maps: The Plasticity and Creep of Metals and Ceramics*. Oxford, UK: Pergamon Press, 1982. ISBN: 978-0080293387.
- [61] Ghafaar, M. A., Mazen, A., and El-Mahallawy, N. “Application of the rule of mixtures and Halpin-Tsai equations to woven fabric reinforced epoxy composites”. In: *Journal of Engineering Sciences* 34(1), 2006, pp. 227–236.
- [62] Giroux, P., Dalle, F., and Sauzay, M. “Mechanical and microstructural stability of P92 steel under uniaxial tension at high temperature”. In: *Materials Science and Engineering A* 527, 2010, pp. 3984–3993. DOI: 10.1016/j.msea.2010.03.001.
- [63] Götz, G. “Langzeitentwicklung der Mikrostruktur neuer 9 - 12 % Chromstähle für den Einsatz in Kraftwerken”. PhD Thesis. Friedrich-Alexander-Universität Erlangen-Nürnberg (FAU), 2004.
- [64] Griebel, M., Zumbusch, G., and Knapek, S. “Time Integration Methods”. In: *Numerical Simulation in Molecular Dynamics: Numerics, Algorithms, Parallelization, Applications*. Berlin, Heidelberg: Springer Berlin Heidelberg, 2007, pp. 11–237. DOI: 10.1007/978-3-540-68095-6\_6.
- [65] Griffiths, D. F. and Higham, D. J. *Numerical Methods for Ordinary Differential Equations: Initial Value Problems*. London, UK: Springer Science & Business Media, 2010. ISBN: 978-1-84996-294-3.



- [66] Guennouni, T. “Sur une méthode de calcul de structures soumises à des chargements cycliques: l’homogénéisation en temps”. In: 22, 1988, pp. 417–455. DOI: 10 . 1051 / m2an/1988220304171.
- [67] Hairer, E. and Wanner, G. *Solving Ordinary Differential Equations I: Nonstiff Problems*. Springer, 1991.
- [68] Hairer, E. and Wanner, G. *Solving Ordinary Differential Equations II: Stiff and Differential-Algebraic Problems*. Springer, 1996.
- [69] Haouala, S. and Doghri, I. “Modeling and algorithms for two-scale time homogenization of viscoelastic-viscoplastic solids under large number of cycles”. In: *International Journal of Plasticity* 70, 2015, pp. 98–120. DOI: 10 . 1016/j . ijplas . 2015 . 03 . 005.
- [70] Haouala, S. “Time and Space (4D) Homogenization for Viscoelastic-Viscoplastic Solids Under Large Numbers of Cycles”. PhD thesis. Louvain-la-Neuve, Belgium: Université catholique de Louvain, 2016. URL: <http://hdl.handle.net/2078.1/171109>.
- [71] Haupt, P. and Kurth, J. *Continuum Mechanics and Theory of Materials*. Advanced Texts in Physics. Springer Berlin Heidelberg, 2002. ISBN: 9783540431114. URL: <https://books.google.de/books?id=BKFotA-0sewC>.
- [72] Hoff, N. J. “The necking and the rupture of rods subjected to constant tensile loads”. In: *Journal of Applied Mechanics* 20(1), 1953, pp. 105–108. DOI: 10 . 1115/1 . 401060.
- [73] Hogge, M. and Assaker, D. “Unified Versus Non Unified Constitutive Models for Thermo-Viscoplasticity by the Finite Element Method”. In: *31st Structures, Structural Dynamics and Materials Conference*. 1990. DOI: 10 . 2514/6 . 1990-973.
- [74] Holdsworth, S., Mazza, E., Binda, L., and Ripamonti, L. “Development of thermal fatigue damage in 1CrMoV rotor steel”. In: *Nuclear Engineering and Design* 237(24), 2007, pp. 2292–2301. DOI: 10 . 1016/j . nucengdes . 2007 . 05 . 002.
- [75] Hughes, T. J. and Stewart, J. R. “A space-time formulation for multiscale phenomena”. In: *Journal of Computational and Applied Mathematics* 74(1), 1996, pp. 217–229. ISSN: 0377-0427. DOI: 10 . 1016/0377-0427(96)00025-8.
- [76] IEA (2021). *Key World Energy Statistics 2021*. <https://www.iea.org/reports/key-world-energy-statistics-2021>. Online; accessed 26. May 2023.
- [77] Illschner, B. “Kriechverhalten, Lebensdauer und Zeitstandfestigkeit der Metalle”. In: *Festigkeits- und Bruchverhalten bei höheren Temperaturen*. Ed. by Dahl, W. and Pitsch, W. VDEh, Düsseldorf, 1980, pp. 1–30.
- [78] Illschner, B. *Hochtemperatur-Plastizität: Warmfestigkeit und Warmverformbarkeit metallischer und nichtmetallischer Werkstoffe*. Reine und angewandte Metallkunde in Einzeldarstellungen. Springer Berlin Heidelberg New York, 1973.
- [79] Iserles, A. *A First Course in the Numerical Analysis of Differential Equations*. 2nd. Cambridge, UK: Cambridge University Press, 2009. ISBN: 978-0-521-73490-5.
- [80] Jameson, A. “Overview of Time Integration Methods”. In: *Computational Aerodynamics*. Cambridge Aerospace Series. Cambridge University Press, 2022, 308–329.
- [81] Kachanov, L. M. *Introduction to Continuum Damage Mechanics*. Dordrecht: Springer, 1986.

- [82] Kimura, K. “9Cr-1Mo-V-Nb steel”. In: *Creep Properties of Heat Resistant Steels and Superalloys* (Martienssen, W., ed.) Ed. by Yagi, K., Merckling, G., Kern T.-U. and Irie, H., and Warlimont, H. Springer-Verlag Berlin Heidelberg.
- [83] Knape, K. and Altenbach, H. “Application of the Two-Time-Scale Approach to the Constitutive Equations of High-Temperature Steel”. In: *Lectures Notes on Advanced Structured Materials 3*. Ed. by Altenbach, H., Hitzler, L., Johlitz, M., Merkel, M., and Öchsner, A. Cham: Springer Nature Switzerland, 2025, pp. 427–438. ISBN: 978-3-031-77403-4. DOI: 10.1007/978-3-031-77403-4\_25.
- [84] Knape, K. and Altenbach, H. “Modeling the Inelastic Behavior of High-Temperature Steels Using a Two-Time-Scale Approach”. In: *Lectures Notes on Advanced Structured Material*. Ed. by Altenbach, H., Johlitz, M., Merkel, M., and Öchsner, A. Cham: Springer International Publishing, 2022. DOI: 10.1007/978-3-031-11589-9\_23.
- [85] Knape, K. and Altenbach, H. “On the Ways to Numerically Implement the Two-Time-Scale Approach”. In: *Lectures Notes on Advanced Structured Materials 2*. Ed. by Altenbach, H., Hitzler, L., Johlitz, M., Merkel, M., and Öchsner, A. Cham: Springer Nature Switzerland, 2024, pp. 401–412. DOI: 10.1007/978-3-031-49043-9\_23.
- [86] Koo, G.-H. and Kwon, J.-H. “Identification of inelastic material parameters for modified 9Cr–1Mo steel applicable to the plastic and viscoplastic constitutive equations”. In: *International Journal of Pressure Vessels and Piping* 88(1), 2011, pp. 26–33. ISSN: 0308-0161. DOI: 10.1016/j.ijpvp.2010.11.004.
- [87] Kostenko, Y., Almstedt, H., Naumenko, K., Linn, S., and Scholz, A. “Robust methods for creep fatigue analysis of power plant components under cyclic transient thermal loading”. In: *Proceedings of the ASME Turbo Expo 2024: Turbomachinery Technical Conference and Exposition 5*, 2013. DOI: 10.1115/GT2013-95680.
- [88] Kowalewski, Z., Hayhurst, D., and Dyson, B. “Mechanisms-based creep constitutive equations for an aluminium alloy”. In: *The Journal of Strain Analysis for Engineering Design* 29(4), 1994, pp. 309–316.
- [89] Krempl, E. “Creep-Plasticity Interaction”. In: *Creep and Damage in Materials and Structures*. Ed. by Altenbach, H. and Skrzypek, J. J. Wien: Springer Wien, 1999, pp. 285–348. DOI: 10.1007/978-3-7091-2506-9\_6.
- [90] Krempl, E. and Ho, K. “Inelastic deformation: phenomenology, modeling and simulation”. In: *Applied Mechanics Reviews* 39(10), 1986, pp. 1475–1484.
- [91] Labergere, C., Saanouni, K., Sun, Z. D., Dhifallah, M. A., Li, Y., and Duval, J. L. “Prediction of Low Cycle Fatigue Life Using Cycles Jumping Integration Scheme”. In: *Damage Mechanics: Theory, Computation and Practice*. Vol. 784. Applied Mechanics and Materials. Trans Tech Publications Ltd, Sept. 2015, pp. 308–316. DOI: 10.4028/www.scientific.net/AMM.784.308.
- [92] Ladeveze, J. “Methodes constructives pour la simulation numerique d’ecoulement de fluides non newtoniens”. PhD thesis. Universite Paris 6, 1985.
- [93] Ladeveze, P. and Zienkiewicz, O. C. *New Advances in Computational Structural Mechanics: Proceedings of the European Conference on New Advances in Computational Structural Mechanics, Giens, France, 2-5 April 1991*. USA: Elsevier Science Inc., 1992. ISBN: 0444890572.

- [94] Lambert, J. D. *Numerical Methods for Ordinary Differential Systems: The Initial Value Problem*. Chichester, UK: John Wiley & Sons, 1991. ISBN: 978-0-471-92990-3.
- [95] Landau, E. *Handbuch der Lehre von der Verteilung der Primzahlen*. Leipzig: Teubner, 1909.
- [96] Lanids, Fred. *gas-turbine engine*. <https://www.britannica.com/technology/gas-turbine-engine>. Online; accessed 25. May 2023.
- [97] Lee, J., Ghassemi-Armaki, H., Maruyama, K., Muraki, T., and Asahi, H. “Causes of breakdown of creep strength in 9Cr–1.8W–0.5Mo–VNb steel”. In: *Materials Science and Engineering A-structural Materials Properties Microstructure and Processing* 428, 2006, pp. 270–275. DOI: 10.1016/j.msea.2006.05.010.
- [98] Lemaitre, J. and Chaboche, J.-L. *Mechanics of Solid Materials*. Cambridge: Cambridge University Press, 1990.
- [99] Lesne, P.-M. and Savalle, S. *An efficient cycles jump technique for viscoplastic structure calculations involving large number of cycles*. Technical Report TP no. 1989-138. ONERA – The French Aerospace Lab, 1989, p. 13.
- [100] LeVeque, R. J. *Finite Difference Methods for Ordinary and Partial Differential Equations: Steady-State and Time-Dependent Problems*. Philadelphia, PA: SIAM, 2007. ISBN: 978-0-898716-29-0.
- [101] Loew, P., Poh, L. H., Peters, B., and Beex, L. “Accelerating fatigue simulations of a phase-field damage model for rubber”. In: *Computer Methods in Applied Mechanics and Engineering* 370, Oct. 2020, p. 113247. DOI: 10.1016/j.cma.2020.113247.
- [102] Luccioni, L. X., Pestana, J. M., and Taylor, R. L. “Finite element implementation of non-linear elastoplastic constitutive laws using local and global explicit algorithms with automatic error control”. In: *International Journal for Numerical Methods in Engineering* 50(5), 2001, pp. 1191–1212. DOI: 10.1002/1097-0207(20010220)50:5<1191::AID-NME73>3.0.CO;2-T.
- [103] Lung, D. “Machinability of Carbon Steel”. In: *CIRP Encyclopedia of Production Engineering*. Ed. by Chatti, S., Laperrière, L., Reinhart, G., and Tolio, T. Berlin, Heidelberg: Springer Berlin Heidelberg, 2019, pp. 1076–1082. DOI: 10.1007/978-3-662-53120-4\_6698.
- [104] Maier, H. J., Niendorf, T., and Bürgel, R. *Handbuch Hochtemperatur-Werkstofftechnik*. Springer Vieweg Wiesbaden, 2019. DOI: 10.1007/978-3-658-25314-1.
- [105] Manchiraju, S., Asai, M., and Gosh, S. “A dual-time-scale finite element model for simulating cyclic deformation of polychrystalline alloys”. In: *The Journal of Strain Analysis for Engineering Design* 42, 2007, pp. 183–200. DOI: 10.1243/03093247JSA233.
- [106] Massoudi, M. “A note on the meaning of mixture viscosity using the classical continuum theories of mixtures”. In: *International Journal of Engineering Science* 46(7), 2008, pp. 677–689. ISSN: 0020-7225. DOI: 10.1016/j.ijengsci.2008.01.008.
- [107] Miller, A. “An inelastic constitutive model for monotonic, cyclic, and creep deformation: Part I—Equations development and analytical procedures”. In: *Journal of Engineering Materials and Technology* 98(2), 1976, pp. 97–105. DOI: 10.1115/1.3443367. eprint: [https://asmedigitalcollection.asme.org/materialstechnology/article-pdf/98/2/97/5483497/97\\_1.pdf](https://asmedigitalcollection.asme.org/materialstechnology/article-pdf/98/2/97/5483497/97_1.pdf).

- [108] Morrow, J. “Cyclic Plastic Energy and Fatigue of Metals”. In: *Fatigue of Metals*. Vol. 378. ASTM STP. Philadelphia: ASTM International, 1964, pp. 45–87.
- [109] *Motion and Control Technology Blog: Natural Gas Combined Cycle Power Plants: History, Trends and Outlook*. <https://blog.parker.com/site/usa/details-home-page/natural-gas-combined-cycle-power-plants-history-trends-and-outlook-us>. Online; accessed 15. April 2022.
- [110] Naumenko, K. and Altenbach, H. *Modeling of Creep for Structural Analysis*. Springer Berlin, Heidelberg, 2007. DOI: 10.1007/978-3-540-70839-1.
- [111] Naumenko, K. and Altenbach, H. *Modeling High Temperature Materials Behavior for Structural Analysis Part I: Continuum Mechanics Foundations and Constitutive Models*. Vol. 28. Advanced Structured Materials: Springer International Publishing, 2016. DOI: 10.1007/978-3-319-31629-1.
- [112] Naumenko, K., Altenbach, H., and Gorash, Y. “Creep analysis with a stress range dependent constitutive model”. In: *Archive of Applied Mechanics* 79, 2009, pp. 619–630. DOI: 10.1007/s00419-008-0287-5.
- [113] Naumenko, K., Altenbach, H., and Kutschke, A. “A combined model for hardening, softening, and damage processes in advanced heat resistant steels at elevated temperature”. In: *International Journal of Damage Mechanics* 20, 2011, pp. 578–597. DOI: 10.1177/1056789510386851.
- [114] Naumenko, K. and Gariboldi, E. “A phase mixture model for anisotropic creep of forged Al-Cu-Mg-Si alloy”. In: *Materials Science and Engineering: A* 618, 2014, pp. 368–376. DOI: 10.1016/j.msea.2014.08.028.
- [115] Naumenko, K. and Kostenko, Y. “Structural analysis of a power plant component using a stress-range-dependent creep-damage constitutive model”. In: *Materials Science and Engineering: A* 510-511, 2009, pp. 169–174. DOI: 10.1016/j.msea.2008.04.096.
- [116] Naumenko, K., Kutschke, A., Kostenko, Y., and Rudolf, T. “Multi-axial thermo-mechanical analysis of power plant components from 9-12 Cr steels at high temperature”. In: *Engineering Fracture Mechanics* 78, 2011, pp. 1657–1668. DOI: 10.1016/j.engfracmech.2010.12.002.
- [117] Naumenko, K. and Altenbach, H. *Modeling of Creep for Structural Analysis*. Springer, Jan. 2007. ISBN: 9783540708391. DOI: 10.1007/978-3-540-70839-1\_1.
- [118] Naumenko, K., Altenbach, H., and Kutschke, A. “A constitutive model for creep and long-term strength in advanced heat resistant steels and structures”. In: *Proceedings of the 7th EUROMECH Solid Mechanics Conference* 2(3), 2009, pp. 1–14.
- [119] Nayfeh, A. *Introduction to Perturbation Methods*. New York: John Wiley & Sons, 1993.
- [120] Odqvist, F. *Mathematical Theory of Creep and Creep Rupture*. Oxford mathematical monographs. Clarendon Press, 1974. ISBN: 9780198535225. URL: <https://books.google.de/books?id=clh8AAAAIAAJ>.
- [121] Oechsner, M., Berger, C., and Kloos, K.-H. “Werkstoff- und Bauteileigenschaften”. In: *Dubbel Taschenbuch für den Maschinenbau I: Grundlagen und Tabellen*. Ed. by Bender, B. and Göhlich, D. Berlin, Heidelberg: Springer Berlin Heidelberg, 2020, pp. 475–519. DOI: 10.1007/978-3-662-59711-8\_29.

- [122] Ohno, N. “Recent topics in constitutive modeling of cyclic plasticity and viscoplasticity”. In: *Applied Mechanics Reviews* 43(11), Nov. 1990, pp. 283–295. DOI: 10.1115/1.3119155.
- [123] Oskay, C. and Fish, J. “Fatigue life prediction using 2-scale temporal asymptotic homogenization”. In: *International Journal for Numerical Methods in Engineering* 61, 2004, pp. 329–359. DOI: 10.1002/nme.1069.
- [124] Pasquale, A., Chinesta, F., Abisset-Chavanne, E., and Ammar, A. “A time multiscale decomposition in cyclic elasto-plasticity”. In: *Communications in Nonlinear Science and Numerical Simulation* 125, 2023, p. 107465. DOI: 10.1016/j.cnsns.2023.107465.
- [125] Penny, R. and Marriott, D. *Design for Creep*. London: Chapman & Hill, 1995.
- [126] Petersmeier, T. *Isothermes Hochtemperaturermüdungsverhalten des Stahles X22CrMoV12-1*. Vol. 472. VDI Forschungsberichte Reihe 5. Düsseldorf: VDI Verlag, 1997.
- [127] Piwecki, M. “Tensile behaviour of a metastable austenitic stainless steel and its individual phase components”. In: *Materials Science and Engineering: A* 156(1), 1992, pp. 77–83. ISSN: 0921-5093. DOI: 10.1016/0921-5093(92)90417-Y.
- [128] Polcik, P. “Modellierung des Verformungsverhaltens der warmfesten 9-12%-Chromstähle im Temperaturbereich von 550 - 650°C”. PhD thesis. Erlangen-Nürnberg: Friedrich-Alexander- Universität, 1998.
- [129] Polcik, P., Sailer, T., Blum, W., Straub, S., Bursik, J., and Orlova, A. “On the microstructural development of the tempered martensitic Cr-steel P 91 during long-term creep—a comparison of data”. In: *Materials Science & Engineering A: Structural Materials: Properties, Microstructure and Processing* 260(1-2), 1999, pp. 252–259. DOI: 10.1016/S0921-5093(98)00887-9.
- [130] Prager, W. “A new method of analyzing stresses and strains in work hardening plastic solids”. In: *Journal of Applied Mechanics* 23(3), 1956, pp. 493–496.
- [131] Priester, L. *Grain boundaries: from theory to engineering*. Vol. 172. Springer Science & Business Media, 2012.
- [132] Puel, G. and Aubry, D. “CCF modelling with use of a two-timescale homogenization model”. In: *Procedia Engineering* 2, 2010, pp. 787–796. DOI: 10.1016/j.proeng.2010.03.085.
- [133] Pugh, C. and Robinson, D. “Some trends in constitutive equation model development for high-temperature behavior of fast-reactor structural alloys”. In: *Nuclear Engineering and Design* 48(1), 1978. Special Issue Structural Mechanics in Reactor Technology - Smirt-4, pp. 269–276. DOI: 10.1016/0029-5493(78)90221-2.
- [134] Rajagopal, K. R. and Tao, L. *Mechanics of Mixtures*. WORLD SCIENTIFIC, 1995. DOI: 10.1142/2197. eprint: <https://www.worldscientific.com/doi/pdf/10.1142/2197>.
- [135] Reback, J., McKinney, W., van den Bossche, J., and Augspurger, T. *pandas-dev/pandas: Pandas*. <https://pandas.pydata.org/>. 2020. URL: <https://pandas.pydata.org/>.

- [136] Reddy, J. *Applied Functional Analysis and Variational Methods in Engineering*. McGraw-Hill, 1993.
- [137] Reuß, A. “Berechnung der Fließgrenze von Mischkristallen auf Grund der Plastizitätsbedingung für Einkristalle.” In: *ZAMM - Zeitschrift für Angewandte Mathematik und Mechanik* 9, 1929, pp. 49–58. URL: <https://api.semanticscholar.org/CorpusID:122637382>.
- [138] Röttger, D. *Untersuchungen zum Wechselverformungs- und Zeitstandverhalten der Stähle X20CrMoV12-1 und X10CrMoVNb9-1*. German. Vol. 392. Fortschritt-Berichte VDI Reihe 5, Grund- und Werkstofftechnik. Zugl.: Bochum, Univ., Diss., 1997. Düsseldorf: VDI Verlag, 1997.
- [139] Saad, A. A. “Cyclic Plasticity and Creep of Power Plant Materials”. PhD thesis. The University of Nottingham, 2012. url: [http://eprints.nottingham.ac.uk/12538/1/PhD\\_thesis\\_-\\_Abdullah\\_Aziz\\_Saad.pdf](http://eprints.nottingham.ac.uk/12538/1/PhD_thesis_-_Abdullah_Aziz_Saad.pdf).
- [140] Sanders, J. A. and Verhulst, F. *Averaging Methods in Nonlinear Dynamical Systems*. New York: Springer, 1985.
- [141] Scholz, A. and Berger, C. “Deformation and life assessment of high temperature materials under creep fatigue loading”. In: *International Journal of Fatigue* 28, 2006, pp. 643–651.
- [142] Schwienheer, M., Haase, H., Scholz, A., and Berger, C. “Long Term Creep and Creep Fatigue Properties of the Martensitic Steels of Type (G)X12CrMoWVNbN10-1-1”. In: *Materials for Advanced Power Engineering 2002*. Ed. by Lecomte-Beckers, J., Carton, M., Schubert, F., and Schmiedt, U. D. E. Vol. 3. Schriften des Forschungszentrums Jülich. Reihe Energietechnik 21. Jülich: Forschungszentrum Jülich GmbH, 2002, pp. 1409–1418. ISBN: 3-89336-312-2.
- [143] Shumway, R. H. and Stoffer, D. S. *Time Series Analysis and Its Applications: With R Examples*. Springer, 2017.
- [144] Siemens Energy. *Reliable gas turbines*. <https://www.siemens-energy.com/global/en/offerings/power-generation/gas-turbines.html>. Online; accessed 10. April 2022.
- [145] Simo, J. C. and Hughes, T. J. R. *Computational Inelasticity*. New York: Springer-Verlag, 1998.
- [146] Simon, A., Samir, A., Scholz, A., and Berger, C. “Konstitutive Beschreibung eines 10%Cr-Stahls zur Berechnung betriebsnaher Kriechermüdungsbeanspruchung”. In: *Materialwissenschaft und Werkstofftechnik* 38(8), 2007, pp. 635–641. DOI: 10.1002/mawe.200600125.
- [147] Stein, E. and Barthold, F.-J. *Der Ingenieurbau: Grundwissen in 9 Bänden. Werkstoffe, Elastizitätstheorie*. Ed. by Mehlhorn, G. Bd. 4. Ernst & Sohn, 1997. ISBN: 9783433015704. URL: <https://books.google.de/books?id=X14hzQEACAAJ>.
- [148] Stoller, R. E. and Odette, G. R. “A composite model of microstructural evolution in austenitic stainless steel under fast neutron irradiation”. In: *Radiation-induced changes in microstructure, 13th international symposium, ASTM STP*. Vol. 955. 1987, pp. 371–392.

- [149] Straub, S. *Verformungsverhalten und Mikrostruktur warmfester martensitischer 12 %-Chromstähle*. Fortschritt-Berichte VDI.: Grund- und Werkstoffe. VDI-Verlag, 1995. URL: <https://books.google.co.cr/books?id=2RxhtwAACAAJ>.
- [150] Truesdell, C. and Noll, W. *The Non-Linear Field Theories of Mechanics*. 2nd. Vol. III/3. Handbuch der Physik. Berlin, Heidelberg: Springer, 1992. DOI: 10.1007/978-3-662-10388-3.
- [151] Velay, V., Bernhart, G., and Penazzi, L. “Cyclic behavior modeling of a tempered martensitic hot work tool steel”. In: *International Journal of Plasticity* 22(3), 2006, pp. 459–496. DOI: 10.1016/j.ijplas.2005.03.007.
- [152] Voigt, W. “Ueber die Beziehung zwischen den beiden Elasticitätsconstanten isotroper Körper”. In: *Annalen der Physik* 274(12), 1889, pp. 573–587. DOI: 10.1002/andp.18892741206. eprint: <https://onlinelibrary.wiley.com/doi/pdf/10.1002/andp.18892741206>.
- [153] Wang, J., Steinmann, P., Rudolph, J., and Willuweit, A. “Simulation of creep and cyclic viscoplastic strains in high-Cr steel components based on modified Becker-Hackenberg model”. In: *International Journal of Pressure Vessels and Piping* 128, 2015, pp. 36–47. DOI: 10.1016/j.ijpvp.2015.02.003.
- [154] Wang, P., Cui, L., Lyschik, M., Scholz, A., Berger, C., and Oechsner, M. “A local extrapolation based calculation reduction method for the application of constitutive material models for creep fatigue assessment”. In: *International Journal of Fatigue* 44, 2012, pp. 253–259. DOI: 10.1016/j.ijfatigue.2012.04.018.
- [155] Wang, Y., Zhao, H., Li, Y., and Zhang, L. “Strain softening of natural rubber composites filled with carbon black and silica”. In: *Journal of Rheology* 67(1), 2023, pp. 157–168. DOI: 10.1122/8.0000491.
- [156] Wegst, M. and Wegst, C. *Stahlschlüssel - Key to Steel CD-ROM 2019: Deutsch/ Englisch/ Französisch /Eine Selbst Frei Definierbare Sprache*. Stahlschlüssel, 2020. ISBN: 9783922599364. URL: <https://books.google.de/books?id=y6tmzQEACAAJ>.
- [157] Weinan, E. *Principles of Multiscale Modeling*. Cambridge University Press, 2011.
- [158] Weinan, E and Engquist, B. “The heterogeneous multiscale methods”. In: *Communications in Mathematical Sciences* 1(1), 2003, pp. 87–132.
- [159] Weinan, E. and Engquist, B. “Heterogeneous multiscale methods: A review”. In: *Communications in Computational Physics* 2(3), 2007, pp. 367–450.
- [160] Wriggers, P. “Nonlinear Finite Element Methods”. In: vol. 4. Springer, 2008. DOI: 10.1007/978-3-642-56865-7.
- [161] Yu, Q. and Fish, J. “Temporal homogenization of viscoelastic and viscoplastic solids subjected to locally periodic loading”. In: *Computational Mechanics* 29, 2002, pp. 199–211. DOI: 10.1007/s00466-002-0334-y.
- [162] Zhang, S.-L. and Xuan, F.-Z. “Interaction of cyclic softening and stress relaxation of 9–12% Cr steel under strain-controlled fatigue-creep condition: Experimental and modeling”. In: *International Journal of Plasticity* 98, 2017, pp. 45–64. ISSN: 0749-6419. DOI: 10.1016/j.ijplas.2017.06.007.

## *Bibliography*

- [163] Zhao, C., Zhang, J., Fu, J., Lian, Y., Zhang, Z., Zhang, C., and Huang, J. “Low-Cycle Fatigue Behavior of the Novel Steel and 30SiMn2MoV Steel at 700 °C”. In: *Materials* 13(24), 2020, p. 5753. DOI: 10.3390/ma13245753.
- [164] Zienkiewicz, O. C., Taylor, R. L., and Zhu, J. *The Finite Element Method for Solid and Structural Mechanics*. Elsevier, 2005.